1991

Application of mathematical morphology to the analysis of X-ray NDE images

Mathew Scaria Chackalackal
Iowa State University

Application of Mathematical Morphology to the analysis of X-ray NDE Images

by

Mathew Scaria Chackalackal

A Thesis Submitted to the

Graduate Faculty in Partial Fulfillment of the

Requirements for the Degree of

MASTER OF SCIENCE

Department: Electrical Engineering and Computer Engineering
Major: Electrical Engineering

Approved:

_____
In Charge of Major Work

_____
For the Major Department

_____
For the Graduate College

Iowa State University
Ames, Iowa
1991

TABLE OF CONTENTS

ACKNOWLEDGEMENTS x

CHAPTER 1. INTRODUCTION 1

CHAPTER 2. BINARY MORPHOLOGY 5

Minkowski Algebra 5

Translation 5

Minkowski Addition 6

Minkowski Subtraction 8

Illustration of Minkowski Subtraction 8

Binary Morphology 9

Dilation 10

Properties of Dilation 12

Erosion 14

Properties of Erosion 17

Openings and Closings 21

Properties of Opening and Closing 25

CHAPTER 3. GRAY-SCALE MORPHOLOGY 26

Three Dimensional Binary Image 27

Top Surface and Umbra 27

Gray Scale Dilation 29
Gray Scale Erosion 33
Structuring Elements 38
Decomposition of Structuring Elements 41
CHAPTER 4. MORPHOLOGICAL FILTERS 45
Opening and Closing 46
Hybrid Filtering 50
CHAPTER 5. APPLICATION OF MORPHOLOGICAL FILTERING TO NDE 55
Background Elimination 56
Selection of Structuring Element 60
Elimination of Artifacts 62
Detection of Cracks 64
Report to Westinghouse Electric Corporation on the Evaluation of Sample Radiographs 64
Introduction 66
Processing Techniques and Results 66
Conclusions 68
CHAPTER 6. MORPHOLOGICAL EDGE DETECTION 76
Morphological Gradient 76
Blur Minimum Morphologic Edge Operator 80
CHAPTER 7. CONNECTIVITY 83
Definitions 84

Thinning and Thickening 87

Cluster Fast Segmentation (CFS) 88

CHAPTER 8. APPLICATION OF MATHEMATICAL MORPHOLOGY TO THE STUDY OF MICROSTRUCTURAL CHARACTERISTICS OF METAL MATRIX COMPOSITES 92

Morphological Skeleton 93

Generalized Connectivity Algorithm 94

CHAPTER 9. CONCLUSION 100

CHAPTER 10. BIBLIOGRAPHY 103

LIST OF FIGURES

Figure 2.1: Translation of **A** by **x** 6

Figure 2.2: Minkowski addition of **A** by **B** 7

Figure 2.3: Minkowski subtraction of **A** by **B** 9

Figure 2.4: Illustration of binary dilation 11

Figure 2.5: Illustration of binary dilation 12

Figure 2.6: Illustration of Property D-5 14

Figure 2.7: Illustration of erosion 16

Figure 2.8: Reflection operation 17

Figure 2.9: Illustration of erosion 18

Figure 2.10: Illustration of Property E-1 19

Figure 2.11: Illustration of erosion followed by dilation 22

Figure 2.12: Illustration of opening 23

Figure 2.13: Illustration of closing 24

Figure 3.1: One cube stack in 3-D binary image 28

Figure 3.2: Umbra of a function 29

Figure 3.3: Illustration of dilation using an umbra 30

Figure 3.4: Illustration of gray scale dilation using the top surface elements 31

Figure 3.5: Illustration of gray-scale dilation 34

Figure 3.6: The picture on the left is the digitized image of a Westinghouse radiograph (Courtesy of Westinghouse). The one on the right is the dilated image 35
Figure 3.7: Illustration of gray scale erosion 39
Figure 3.8: The picture on the left is a digitized image of a pipe (Courtesy of Atlantic Richfield Corporation). The one on the right is the eroded image 40
Figure 3.9: 9×9 mask representing a hemisphere. The height of the hemisphere is nine and the origin is at the center of the mask 42
Figure 3.10: Three-dimensional plot of the mask 43
Figure 3.11: Decomposition of a 5×5 cylinder 44

Figure 4.1: Pictorial Illustration of opening 48
Figure 4.2: Digitized radiograph of a composite (Courtesy of Westinghouse) 49
Figure 4.3: The image of composite opened by a 9×9 cylinder 49
Figure 4.4: Illustration of closing 51
Figure 4.5: Digitized image of a frog (Courtesy of the American Association of Railroads) 52
Figure 4.6: Image of frog closed by a 25×25 cylinder 52
Figure 4.7: Schematic of a hybrid filter 53
Figure 4.8: Digitized radiograph of a space shuttle fuel tank (Courtesy of Martin Marietta) and a slice through the image 53
Figure 4.9: Hybrid filtered image and its slice 54

Figure 5.1: Digitized radiograph of a composite (Courtesy of Westinghouse) 58

Figure 5.2: Background estimate obtained by opening 58
Figure 5.3: Extracted Flaws 59
Figure 5.4: Extraction of a flaw hidden in the transition region of a control valve by closing 60
Figure 5.5: Comparing hemisphere with a cylinder in an opening operation 61
Figure 5.6: A horizontal structuring element, **H**, is on the left and a vertical structuring element, **V**, is on the right 63
Figure 5.7: The picture on the left is the image of a composite with artifacts (Courtesy of Westinghouse). The image on the right is the result of artifact reduction 63
Figure 5.8: The picture on the left shows the digitized radiograph of a pipe (Courtesy of Westinghouse). The picture on the right gives the result of crack detection 65
Figure 5.9: Picture of a single wall shot 69
Figure 5.10: Processed result. 70
Figure 5.11: Picture of a single wall shot 70
Figure 5.12: Result of trend removal 70
Figure 5.13: Result of histogram equalization 71
Figure 5.14: Picture of contact print 71
Figure 5.15: Result of trend removal 71
Figure 5.16: Histogram equalized image 72
Figure 5.17: Picture of enlargement of contact print 72
Figure 5.18: Result of trend removal 72
Figure 5.19: Result of histogram equalization 73

Figure 5.20: Picture of a small section of single wall x-ray of sample#2 . . 73
Figure 5.21: Picture of subsection of Figure 5.20 74
Figure 5.22: Result of morphological processing 74
Figure 5.23: Picture of a section of double wall shot 75
Figure 5.24: Result of morphological processing 75
Figure 5.25: Binary image of Figure 5.24 75

Figure 6.1: Illustration of Gradient1 77
Figure 6.2: Illustration of Gradient2 78
Figure 6.3: The picture on the left is the digitized radiograph of a honeycomb (Courtesy of Joe Gray). The one on the right is the edge detected image 79
Figure 6.4: Real time x-ray image of a honeycomb (Courtesy of Joe Gray) 81
Figure 6.5: Edge detected using Sobel operator 82
Figure 6.6: Edge detected using Gradient4 82

Figure 7.1: Structuring element used in hit-or-miss transform 85
Figure 7.2: Illustration of ultimate erosion 86
Figure 7.3: Illustration of Step 1 of CFS 89
Figure 7.4: Illustration of Step 2 89
Figure 7.5: Illustration of Step 3 90
Figure 7.6: Simulated x-ray image of two flaws at different depths in the material 91
Figure 7.7: The picture on the left gives the two seeds and the one on the right gives the separated flaws 91

Figure 8.1: Digitized secondary electron image of metal matrix composite 93

Figure 8.2: Illustration of morphological skeletonizing 95

Figure 8.3: Simulated image of the metal matrix composite showing the silicon carbide particles 96

Figure 8.4: Seeds generated by CFS 97

Figure 8.5: Skeleton of Figure 8.3 98

Figure 8.6: Cluster with the connectivity broken 99

ACKNOWLEDGEMENTS

I would like to express my deepest gratitude and sincere thanks to my major professor, Dr. John P. Basart, for his guidance, encouragement and support throughout this research. I would also like to thank Dr. Steve F. Russell, Dr. William Q. Meeker, and Dr. Hsein-Sen Hung for serving on the committee. I thank my parents and family for all the moral support and guidance they have provided me during the course of my education.

CHAPTER 1. INTRODUCTION

Ever since the beginning, man has been in the relentless pursuit of perfection. From stone age to space age, from caves to condominiums, from carts to planes, trains and automobiles, his drive for consummation has grown considerably. The high quality products that are available in the market at the turn of the twenty first century are living legacies of his unyielding endeavor for excellence. But one fact that most people do not realize is the amount of time and money devoted to quality control and non- destructive evaluation (NDE) that is responsible for the high quality of products. In the past, people used to tap earthenware and other materials as a means of non destructive testing for defects in the material. They could sense the defects by the nature of the sound propagated through the material. The ultrasonic method of NDE is an extension of this principle.

NDE has grown in stature over the last fifty years. Almost every part in an airplane has to undergo some means of NDE testing before it can be airborne. Especially with lot of aging airplanes and increasing air tragedies NDE has become indispensable for the aircraft companies. The automobile industry, space craft industry, manufacturers of nuclear vessels and the railroad industry are some of the other industries, to name a few, where NDE has become essential for their survival. With the drive for high quality products at the lowest prices, a lot of economics also has

come into play. Thus one of the objectives of the NDE community is to make NDE techniques as efficient as possible. There are five major methods of non-destructive testing - radiographic (x-rays), ultrasonic, magnetic, electrical and penetrant.

Ever since its discovery, x-rays have become one of the major methods for medical and material testing. It is the imaging capability of x-rays that has partly contributed to its success in medical and industrial fields. Often it becomes necessary to enhance or process the information on the radiographs. NDE images are invariably noisy and of low contrast. Further, in industrial inspection, technicians have to go through miles of radiographs making their life monotonous. Added to the monotony, human fatigue could cause them to err. Lot of industries prefer to have NDE as an integrated part of the assembly line. This implies automation of non-destructive testing. A conceptual image processing system for NDE applications will have an x-ray source, an imaging system and a processor with the necessary intelligence that can automatically detect the flaws. The nature of x-ray images does not make them favorable candidates for automation. Extracting the flaws from low contrast images with the background trends is not easy. One of the main objectives of my research was to investigate what morphology had to offer for automated detection of flaws.

Mathematical morphology is based on the mathematics of Minkowski Algebra. Minkowski (1903) was a set theoretician who introduced the concepts of dilation to characterize integral measures of certain open sets. Golay (1969), Kirsh et al. (1957), Moore (1968), Preston (1961), and Unger (1958) were some of the early investigators who used dilation as a smoothing operator in image processing. Dilation as an image operator for shape extraction and estimation of image parameters was explored by Matheron (1975) and Serra (1972). Most of the credit for introducing mathematical

morphology as a set theoretical method for image analysis goes to Matheron (1975) and Serra (1982). Some contributions were made by Sternberg to the morphology of gray tone functions (1979 & 1983).

The term morphology denotes the study of form and texture. In image processing applications, it refers to the analysis of geometric structure or texture within an image. The basic strategy is to understand the geometric properties of an image by probing the structure of the image with various forms known as structuring elements. Mathematical morphology provides an approach to the processing of digital images which is based on shape. Appropriately used, mathematical morphological operations tend to simplify image data, preserving their essential shape characteristics and eliminating irrelevancies. The most important contributions of mathematical morphology are the morphological filters - opening and closing. It is opening or closing with the assistance of structuring elements that makes it possible to extract features based on shape and size.

Many papers on mathematical morphology have been published in recent years. The two major publications in this field are the books by Matheron (1975) and Serra (1982). Both of these books are very rigorous and highly mathematical. Alternatively, Giardina's and Dougherty's book (1988), is easy to read and gives a good introduction to the concepts of mathematical morphology. Serra's tutorial paper (1986), summarizes much of the background material in his book. A tutorial overview is provided by Haralick et al. (1987). Sternberg's tutorial paper (1986) explains the concepts of gray-scale morphological transformations. Zhuang and Haralick (1986) discuss the splitting of structuring elements into smaller structuring elements that makes the software routines computationally more efficient, and Skolnick (1986) discusses

background elimination and artifact elimination in the analysis of two-dimensional electrophoretic gels of biological materials. Meyer (1986) discusses autofocussing, segmentation and artifact elimination in cytological specimens. Maragos and Schafer (1986) discuss the numerous applications of morphological filters in image processing. Sternberg (1983), Rodenacker et al. (1983), and Meyer (1979) discuss biomedical applications. Sternberg and Sternberg (1983), and Mandenville (1985) discuss automated industrial inspection using morphological filters.

Chapters 2 and 3 discuss the mathematics of binary and gray-scale morphology. Chapter 4 gives a review of morphological filters. The applications of morphological filters to NDE are discussed with results in Chapter 5. Morphological edge detection is covered in Chapter 6. Applications of connectivity to NDE are discussed with results in Chapters 7 and 8.

CHAPTER 2. BINARY MORPHOLOGY

Morphological tools started becoming popular in the late fifties with the advent of digital computers. Though people in the area of image processing became exposed to mathematical morphology over the last three decades, the principles of mathematical morphology have been around for almost a century. It existed under the name of Minkowski algebra. Most papers on morphology tend to overlook the contributions of H. Minkowski to the development of morphology. The mathematics of morphology evolves from Minkowski Algebra. Any treatise on mathematical morphology will be incomplete without paying tributes to the ingenuity of Minkowski. This chapter begins with a brief discussion of Minkowski algebra. Minkowski (1903), Giardina and Dougherty (1988) discuss the algebraic properties of Minkowski addition and subtraction in great depth.

Minkowski Algebra

Translation

Minkowski addition and subtraction are defined using translations. For an element $\mathbf{x}$ of Euclidean space, the translation of a set of points, $\mathbf{A}$, by $\mathbf{x}$ is defined by:

$$(\mathbf{A})_{\mathbf{x}} = \{a + \mathbf{x} : a \in \mathbf{A}\} \tag{2.1}$$

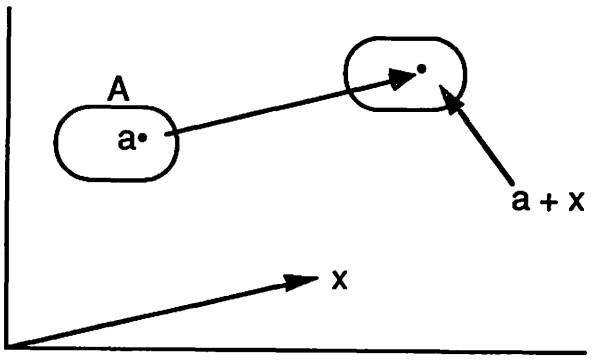

Figure 2.1: Translation of **A** by **x**

where $(\mathbf{A})_{\mathbf{x}}$ denotes **A** translated by **x**. Considering **x** to be a vector in the plane, **A** + **x** is **A** translated along the vector **x**. Thus, when **A** is translated by the vector **x**, every point in **A** is translated by **x**. This is illustrated in Figure 1.1. Translation by a single vector results in a shift of **A** in the spatial domain. The shape and size of **A** remains the same.

Minkowski Addition

Given two sets **A** and **B** in Euclidean space, the Minkowski addition of **A** by **B** is given by:

$$\mathbf{A} \oplus \mathbf{B} = \cup(\mathbf{A} + b); \quad b \in \mathbf{B} \tag{2.2}$$

where $\oplus$ denotes Minkowski addition. Minkowski addition is defined as the union of the translates obtained by translating every element in **A** by every element in **B**. Unlike translation by a single vector, $\mathbf{A} \oplus \mathbf{B}$ does not retain the original size and

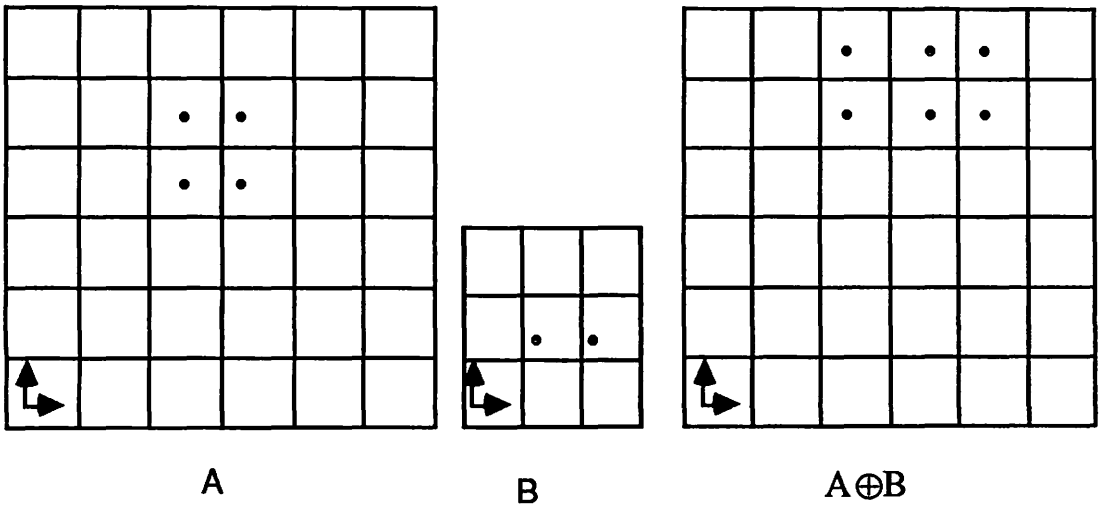

Figure 2.2: Minkowski addition of **A** by **B**

shape of the set **A**.

Illustration of Minkowski Addition:

$$\begin{aligned} \text{Let } \mathbf{A} &= \{(2,3),(2,4),(3,3),(3,4)\} \\ \text{and } \mathbf{B} &= \{(1,1),(2,1)\}. \\ \text{Then } \mathbf{A}+\mathbf{B} &= \{(3,4),(3,5),(4,4),(4,5),(4,4),(4,5),(5,4),(5,5)\} \\ \text{and } \mathbf{A}\oplus\mathbf{B} &= \{(3,4),(3,5),(4,4),(4,5),(5,4),(5,5)\}. \end{aligned}$$

B consists of two elements, which are considered as two different vectors. Each element in **A** is then translated by the two elements in **B**. The translates that occur more than once are deleted to get the final dilated image. Figure 1.2 illustrates this process.

Minkowski Subtraction

Given two sets **A** and **B** in Euclidean space, the Minkowski subtraction of **A** by **B** is defined by:

$$\mathbf{A} \ominus \mathbf{B} = \cap(\mathbf{A} + b);\ b \in \mathbf{B} \tag{2.3}$$

where $\ominus$ denotes Minkowski subtraction. **A** is translated by every element in **B** to obtain different sets of translates, each set corresponding to an element in **B**. All those elements which are common to all the different sets are retained to yield the final result.

Illustration of Minkowski Subtraction

$$\begin{aligned}
\text{Let } \mathbf{A} &= \{(2,3),(2,4),(3,3),(3,4)\} \\
\text{and } \mathbf{B} &= \{(1,1),(2,1)\} = \{b_1, b_2\}. \\
\text{then } \mathbf{A} + b_1 &= \{(3,4),(3,5),(4,4),(4,5)\}, \\
\mathbf{A} + b_2 &= \{(4,4),(4,5),(5,4),(5,5)\} \\
\text{and } \mathbf{A} \ominus \mathbf{B} &= (\mathbf{A} + b_1) \cap (\mathbf{B} + b_2) = \{(4,4),(4,5)\}.
\end{aligned}$$

Two sets of translates are obtained by translating **A** by the elements in **B**. The elements common to the two sets are retained to give the Minkowski subtracted set. Figure 1.3 illustrates this operation.

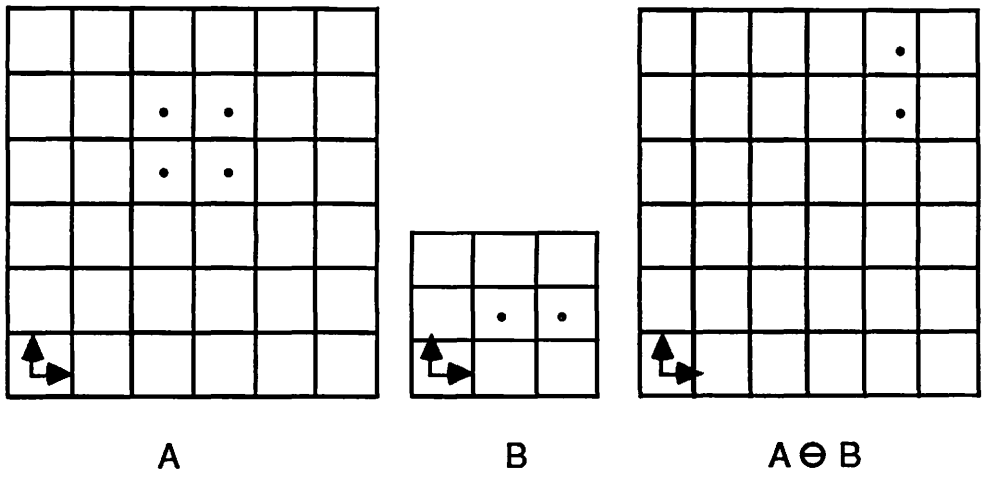

Figure 2.3: Minkowski subtraction of **A** by **B**

Binary Morphology

Binary Morphology evolved from the mathematics of Minkowski algebra. Minkowski addition and subtraction were introduced by Minkowski early in the twentieth century as set theoretic operations. The binary morphological operation, dilation is exactly the same as Minkowski addition. In binary morphology, we deal with images instead of sets. Binary morphology strictly adheres to the properties of Minkowski algebra. In binary morphology, we refer to **A** as the image undergoing the transformation and **B** as the structuring element. Dilation and erosion are the most primitive binary morphological operations. Dilation and erosion are building blocks in the design of other morphological tools. Serra (1972, 1982 and 1986), Haralick et al. (1987) and Matheron (1965 and 1975) are some of the pioneering researchers in binary morphology.

Dilation

Definition D-1: Let **A** and **B** be subsets of Euclidean space. The dilation of **A** by **B** is denoted by $\mathbf{A} \oplus \mathbf{B}$ and is defined by:

$$\mathbf{A} \oplus \mathbf{B} = \{c \mid c = a + b \; for \; some \; a \in \mathbf{A} \; and \; b \in \mathbf{B}\}. \tag{2.4}$$

where **C** is the resulting image in Euclidean space. This is read as **A** dilated by **B** is the set **C**, which is obtained by translating every element in **A** by every element in **B**.

Definiton D-2: The dilation of **A** by **B** is given by :

$$\mathbf{A} \oplus \mathbf{B} = \cup(\mathbf{A})_b \; ; \quad b \in \mathbf{B}. \tag{2.5}$$

This is the definition for Minkowski addition. Binary dilation is the same as Minkowski addition. The two definitions are exactly the same. This definition emphasizes the role of image shifting in implementing dilation. In addition to being shifted in spatial domain, the image grows as a result of dilation.

Illustration of Dilation: Figure 1.4 is a simple case in which the image **A** has a single bright pixel with all the other pixels being zeros. Black dots represent bright pixels. The origin is at the bottom left hand corner. The structuring element has three bright pixels as given in the figure. The bright pixel in **A** is translated individually by every pixel in **B** and the set union of all the translates is taken to obtain the dilated image. The dilation process can be visualized as a slightly different operation. The origin of the structuring element is moved to every bright pixel in **A**. At each alignment of the origin of **B** with **A**, **B** is superimposed on **A**. Proceeding in this manner, we get the final dilated image. Figure 1.5 also illustrates binary

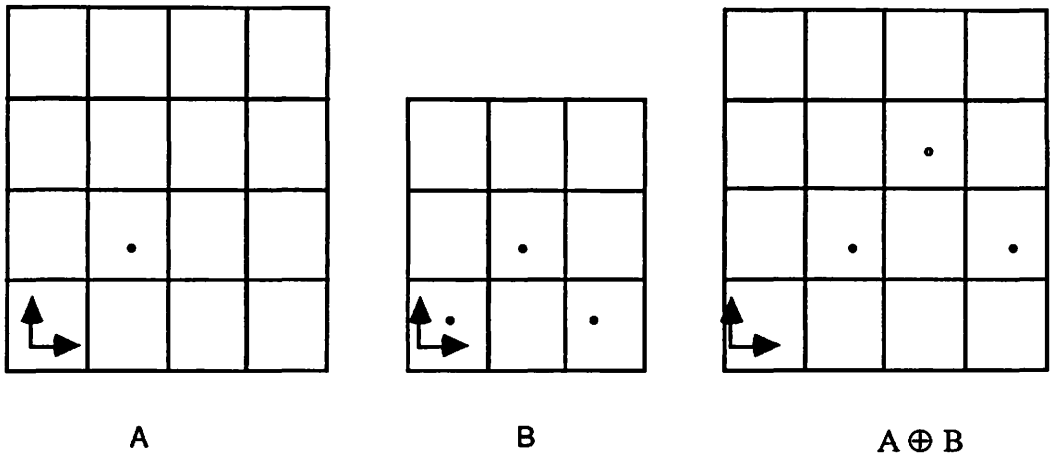

Figure 2.4: Illustration of binary dilation

dilation. In this case, **A** has four bright pixels. Thus four different sets of translates are obtained and the set union of these translates gives the dilated image.

$$
\begin{aligned}
\textit{Let } \mathbf{A} &= \{(0,0),(1,0),(0,1),(1,1)\} \\
\textit{and } \mathbf{B} &= \{(0,0),(1,1),(2,0)\} = \{b_1, b_2, b_3\}. \\
\textit{Then } \mathbf{A} + b_1 &= \{(0,0),(1,0),(0,1),(1,1)\}, \\
\mathbf{A} + b_2 &= \{(1,1),(2,1),(1,2),(2,2)\}, \\
\mathbf{A} + b_2 &= \{(2,0),(3,0),(2,1),(2,3)\} \\
\textit{and } \mathbf{A} \oplus \mathbf{B} &= (\mathbf{A} + b_1) \cup (\mathbf{A} + b_2) \cup (\mathbf{A} + b_3) \\
&= \{(0,0),(1,0),(0,1),(1,1),(2,1),(1,2),(2,2),(2,0),(3,0),(2,3)\}.
\end{aligned}
$$

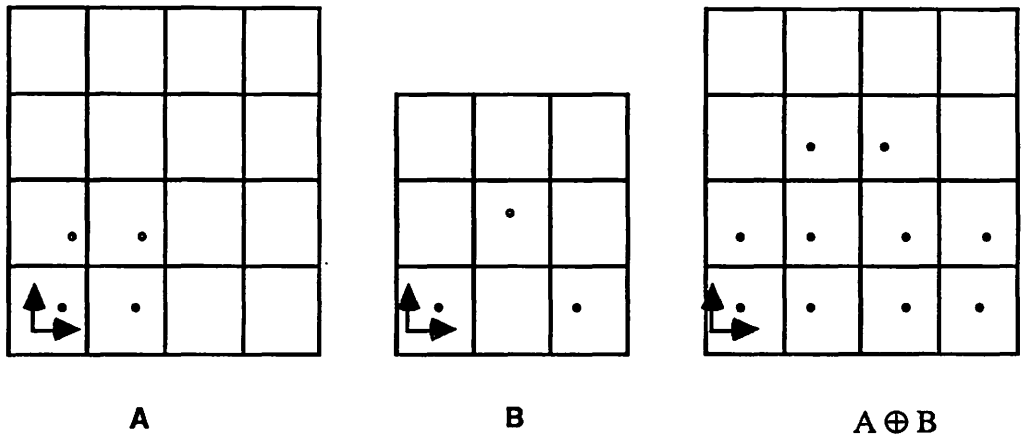

Figure 2.5: Illustration of binary dilation

Properties of Dilation

Property D-1:

$$\mathbf{A} \oplus \mathbf{B} = \mathbf{B} \oplus \mathbf{A}. \tag{2.6}$$

The dilation operation is commutative because addition is commutative.

Property D-2:

$$\mathbf{A} \oplus (\mathbf{B} \oplus \mathbf{C}) = (\mathbf{A} \oplus \mathbf{B}) \oplus \mathbf{C}. \tag{2.7}$$

The dilation operation is associative. This property is useful if the image **A** is to be dilated by a structuring element **D**, which itself can be expressed as the dilation of **B** by **C**. Then $\mathbf{A} \oplus \mathbf{D}$ can be computed as

$$\mathbf{A} \oplus \mathbf{D} = \mathbf{A} \oplus (\mathbf{B} \oplus \mathbf{C}) = (\mathbf{A} \oplus \mathbf{B}) \oplus \mathbf{C}. \tag{2.8}$$

This property is commonly referred to as the chain rule for dilations. The form $(\mathbf{A} \oplus \mathbf{B}) \oplus \mathbf{C}$ represents a considerable savings in number of operations to be

performed when $\mathbf{A}$ is the image and $\mathbf{B} \oplus \mathbf{C}$ is the structuring element. The savings come about because a brute force dilation by $\mathbf{B} \oplus \mathbf{C}$ might take as many as N^2 operations while first dilating $\mathbf{A}$ by $\mathbf{B}$ and then dilating the result by $\mathbf{C}$ could take as few as 2N operations, where N is the number of elements in $\mathbf{B}$ and $\mathbf{C}$.

Property D-3:

$$(\mathbf{A})_x \oplus \mathbf{B} = (\mathbf{A} \oplus \mathbf{B})_x. \tag{2.9}$$

This is the translation invariance property of dilation. Translating $\mathbf{A}$ by $\mathbf{x}$ and then dilating by $\mathbf{B}$ is the same as dilating $\mathbf{A}$ by $\mathbf{B}$ and then translating the result by $\mathbf{x}$.

Property D-4:

$$(\mathbf{A})_x \oplus (\mathbf{B})_{-x} = \mathbf{A} \oplus \mathbf{B}. \tag{2.10}$$

A shift in the image can be compensated by a shift in the structuring element in the opposite direction.

Property D-5: The dilated result contains the original image if the origin belongs to the structuring element. Dilation is an extensive transformation when the origin belongs to the structuring element. Extensivity means that the original is contained in the dilated image. Figure 1.6 gives an example where the origin is not in the structuring element. $\mathbf{A} \oplus \mathbf{B}$ has nothing in common with $\mathbf{A}$.

Property D-6: Dilation is an increasing operation. $\mathbf{A} \subseteq \mathbf{C}$ implies $\mathbf{A} \oplus \mathbf{B} \subseteq \mathbf{C} \oplus \mathbf{B}$. If two images are being dilated by the same structuring element, their growth is proportional to their respective sizes.

Property D-7:

$$\mathbf{A} \oplus (\mathbf{B} \cup \mathbf{C}) = (\mathbf{A} \oplus \mathbf{B}) \cup (\mathbf{A} \oplus \mathbf{C}). \tag{2.11}$$

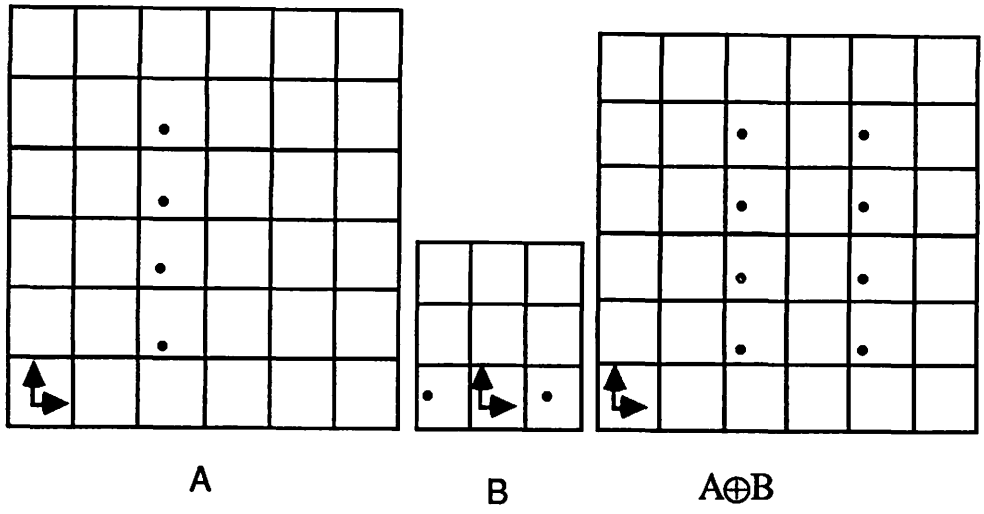

Figure 2.6: Illustration of Property D-5

This property permits a further decomposition of a structuring element into a union of structuring elements. If a structuring element consists of six points, it can be decomposed into the union of six structuring elements, each structuring element consisting of a single point.

Erosion

Erosion is the morphological dual to dilation. Dilation is a growing operation whereas erosion is a shrinking operation. Erosion is the morphological transformation which combines two sets using the vector subtraction of set elements. Erosion is not the same as Minkowski subtraction. However, the notation for erosion is the same as the notation for Minkowski subtraction. From hereon, $\mathbf{A} \ominus \mathbf{B}$ stands for **A** eroded by **B**.

Definition E-1: Given two images **A** and **B** in Euclidean space, the erosion of **A** by **B** is defined by:

$$\mathbf{A} \ominus \mathbf{B} = \{c \mid c + b \in \mathbf{A} \text{ for every } b \in \mathbf{B}\}. \tag{2.12}$$

where **C** is an image in Euclidean space. The above expression denotes that, **A** eroded by **B** is the image **C**, where every element in **C** translated by every element in **B** is within the original image **A**. In an algorithmic sense, every element in **A** is translated by every element in **B**; if the translates of any element of **A** do not lie in the original image, they are deleted. The resulting image is the eroded image. Figure 1.7 illustrates the above definition. **A** is the original image and **B** the structuring element. **D** gives one of the intermediate stages in the process of erosion. $\mathbf{A} = \{(0,1),(1,1),(2,1),(0,2),(1,2),(2,2)\}$ and $\mathbf{B} = \{(0,0),(1,0),(2,0)\}$. **D** gives the result of translating the pixel in the upper left hand corner, (0,2) by **B**. The translates $\{(0,2),(1,2),(2,2)\}$ are contained in **A**. Thus (0,2) is retained in the final eroded image. Similarly the translates of (0,1) are contained in **A**. So (0,1) is also retained in the final image. The translates of all the other pixels are not fully contained in **A** and so they are all deleted. **C** is the final eroded image.

Definition E-2:

$$\mathbf{A} \ominus \mathbf{B} = \{c \mid (\mathbf{B})_c \subseteq \mathbf{A}\}. \tag{2.13}$$

This implies that the translates of every element in **B** by every element in **C** should fall within **A**. Here **C** is the eroded image. Thus the structuring element **B** may be visualized as a probe which slides across the image **A**, testing the spatial nature of **A** at every point. Where **B** translated to c can be contained in **A** (by placing the origin of **B** at c), then c belongs to $\mathbf{A} \ominus \mathbf{B}$.

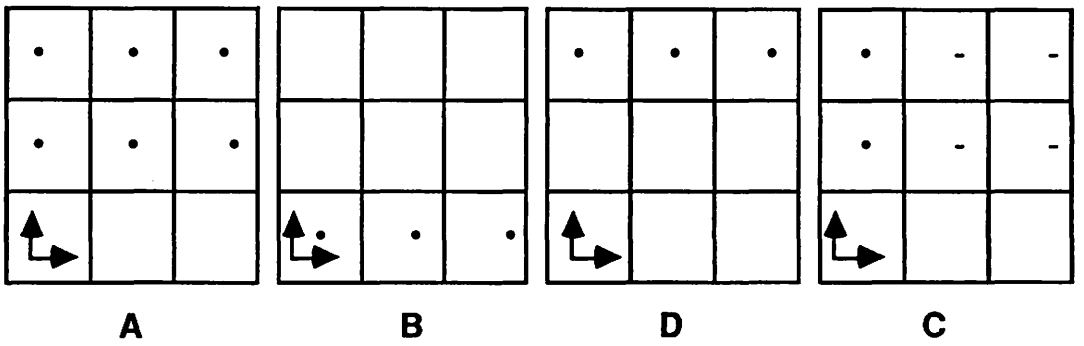

Figure 2.7: Illustration of erosion

Definition E-3: Hadwiger (1957) defines the erosion of **A** by **B** as:

$$\mathbf{A} \ominus \mathbf{B} = \{c \mid \text{for every } b \in \mathbf{B}, \text{ there exists an } a \in \mathbf{A} \text{ such that } x = a - b\} \tag{2.14}$$

Reflection: The reflection of the structuring element **B** is given by:

$$\check{\mathbf{B}} = \{-b : b \in \mathbf{B}\} \tag{2.15}$$

where -b is the scalar multiple of b by -1. Thus, $\check{\mathbf{B}}$ is simply **B**, reflected about the origin as illustrated in Figure 1.8.

Defintion E-4: Sternberg (1986) defines the erosion of **A** by **B** as:

$$\mathbf{A} \ominus \mathbf{B} = \cup(\mathbf{A})_{-b} \; ; \; where - b \in \check{\mathbf{B}}. \tag{2.16}$$

This definition clearly brings out the difference between Minkowski subtraction and erosion. Erosion of **A** by **B** is the intersection of all the translations of **A** by b, where

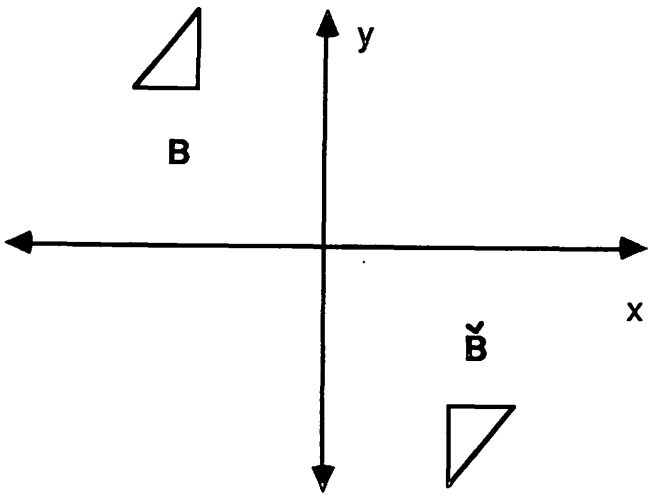

Figure 2.8: Reflection operation

$b \in \mathbf{B}$. It is to be noted that, Minkowski subtraction and erosion are the same if and only if $\mathbf{B} = \check{\mathbf{B}}$, which is possible only if the structuring element is symmetrical about the origin. Also, all the definitions of erosion are equivalent. Figure 1.9 illustrates this definition. **A** is the image and **B** is the structuring element. $\check{\mathbf{B}}$ is the reflection of the structuring element. $\mathbf{A} + b_1, \mathbf{B} + b_2$ and $\mathbf{A} + b_3$ are respectively the translates obtained by translating **A** by each element in $\check{\mathbf{B}}$. **C** gives the final eroded image. **C** is obtained by taking the intersection of $\mathbf{A} + b_1, \mathbf{A} + b_2$ and $\mathbf{A} + b_3$.

Properties of Erosion

Property E-1:

$$\mathbf{A} \ominus \mathbf{B} \subseteq \mathbf{A}. \tag{2.17}$$

Erosion is a shrinking operation. In set terms, the eroded set is contained in the original image. A transformation having this property is called anti-extensive. However,

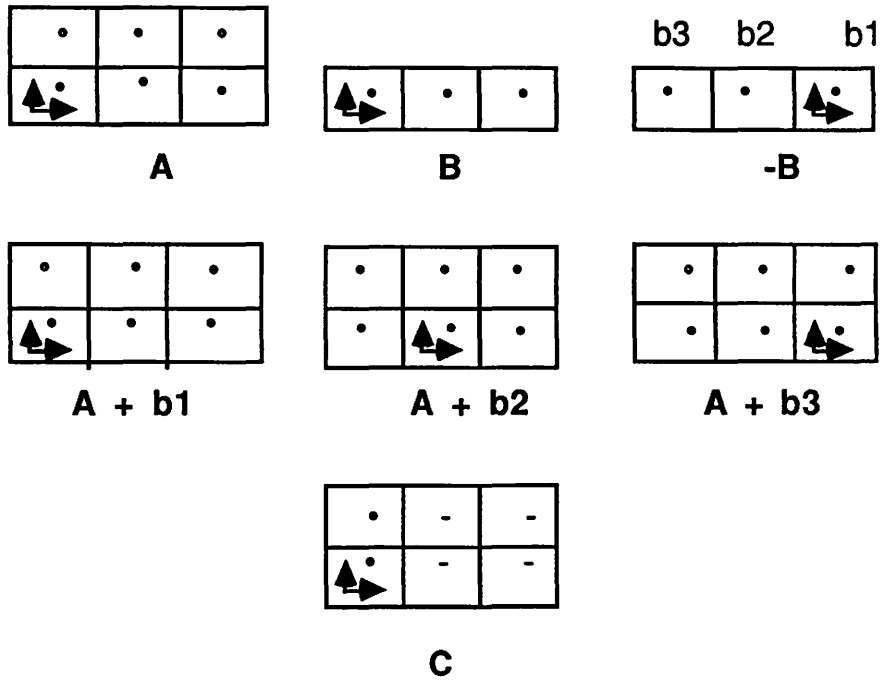

Figure 2.9: Illustration of erosion

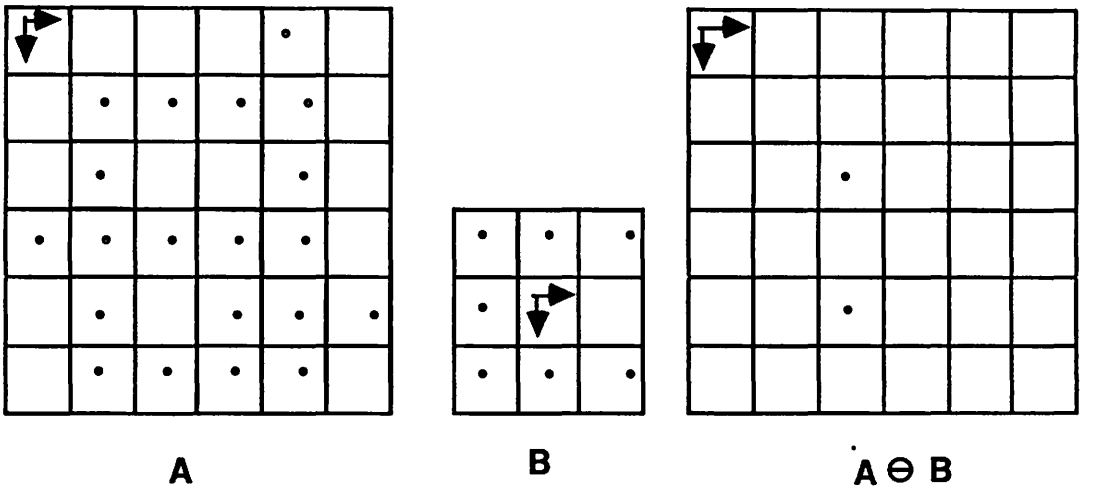

Figure 2.10: Illustration of Property E-1

the erosion transformation is necessarily anti-extensive only if the origin belongs to the structuring element. Figure 2.10 illustrates this property. **A** is the original image and **B** the structuring element. The structuring element does not contain the origin. Notice how $\mathbf{A} \ominus \mathbf{B}$ does not bear any similarity to **A**.

Property E-2: Erosion is translation invariant. Translating **A** by x and then eroding by **B** is the equivalent to eroding **A** by **B** and then translating the result by x. In symbols,

$$\mathbf{A}_x \ominus \mathbf{B} = (\mathbf{A} \ominus \mathbf{B})_x. \tag{2.18}$$

$$\mathbf{A} \ominus \mathbf{B}_x = (\mathbf{A} \ominus \mathbf{B})_{-x}. \tag{2.19}$$

Property E-3: Erosion is an increasing transformation. If **A** is contained in **C**, then **A** eroded by **B** will be contained in **C** eroded by **B**. This is the increasing

property.

$$\mathbf{A} \subseteq \mathbf{C} \; implies \; \mathbf{A} \ominus \mathbf{B} \subseteq \mathbf{C} \ominus \mathbf{B}. \tag{2.20}$$

If image **A** is contained in image **C**, then the erosion of **A** is contained in the erosion of **C**.

Property E-4:

$$\mathbf{A} \supseteq \mathbf{B} \; implies \; \mathbf{D} \ominus \mathbf{A} \subseteq \mathbf{D} \ominus \mathbf{B}. \tag{2.21}$$

If **A** and **B** are structuring elements and **B** is contained in **A**, then the erosion of an image **D** by **A** is more severe than erosion by **B**. This implies that **D** eroded by **A** will be contained in **D** eroded by **B**. This property leads to a natural ordering of the erosions by structuring elements having the same shape but different sizes.

Property E-5: The dilation and erosion transformations bear a marked similarity, in that what one does to to the image foreground the other does to the image background. Dilation results in the growth of the bright pixels at the expense of the background. Erosion results in the growth of the background at the expense of the bright pixels. This property can be formalized as a duality relationship.

$$(\mathbf{A} \ominus \mathbf{B})^c = \mathbf{A}^c \oplus \check{\mathbf{B}}. \tag{2.22}$$

where $\check{\mathbf{B}}$ is the reflection of **B** and $\mathbf{A}^c$ is the complement of **A**.

Property E-6: A chain rule holds for erosion when the structuring element is decomposable through dilation. It is given by:

$$\mathbf{A} \ominus (\mathbf{B} \oplus \mathbf{C}) = (\mathbf{A} \ominus \mathbf{B}) \ominus \mathbf{C}. \tag{2.23}$$

This relation is important as it permits a large erosion to be computed by two successive smaller erosions. This property can be extended to structuring elements decom-

posed as the dilation of K structuring elements. For instance, if $\mathbf{B} = (\mathbf{B}_1 \oplus \cdots \oplus \mathbf{B}_K)$, then

$$\begin{aligned} \mathbf{A} \ominus \mathbf{B} &= \mathbf{A} \ominus (\mathbf{B}_1 \oplus \cdots \oplus \mathbf{B}_K) \\ &= (\cdots(\mathbf{A} \ominus \mathbf{B}_1) \ominus \cdots \ominus \mathbf{B}_K). \end{aligned} \tag{2.24}$$

Openings and Closings

In morphological applications, dilation and erosion are applied in pairs and are seldom used individually. Though dilation and erosion are dual operators, they are not reciprocal operators. Dilating an image followed by erosion or vice versa with the same structuring element does not return the same image. It is found that, when dilation and erosion are applied one after the other in any order, certain features in the image disappear. The size and shape of the features that disappear depend on the size and shape of the structuring element. Figure 2.11 illustrates this phenomenon. **A** is the image and **B** is the structuring element. **C** is obtained by eroding **A** with **B**. **C** is then dilated by **B** to get **D**. As expected **D** is not a replica of **A**. Successive erosion and dilation retained most of the features in **A** except for the two isolated bright pixels. As hinted earlier, erosion followed by dilation with a different structuring element will result in a totally different image. Thus based on the nature of the structuring element, it becomes possible to suppress certain features in the image. This property has been fully exploited in the two morphological filters - opening and closing. The concepts of opening and closing were first studied by Matheron (1965 & 1975). It is opening and closing that shot morphology to prominence in the areas of pattern recognition and industrial vision applications. Morphological filtering an image by an opening or closing operation corresponds to the ideal non-realizable

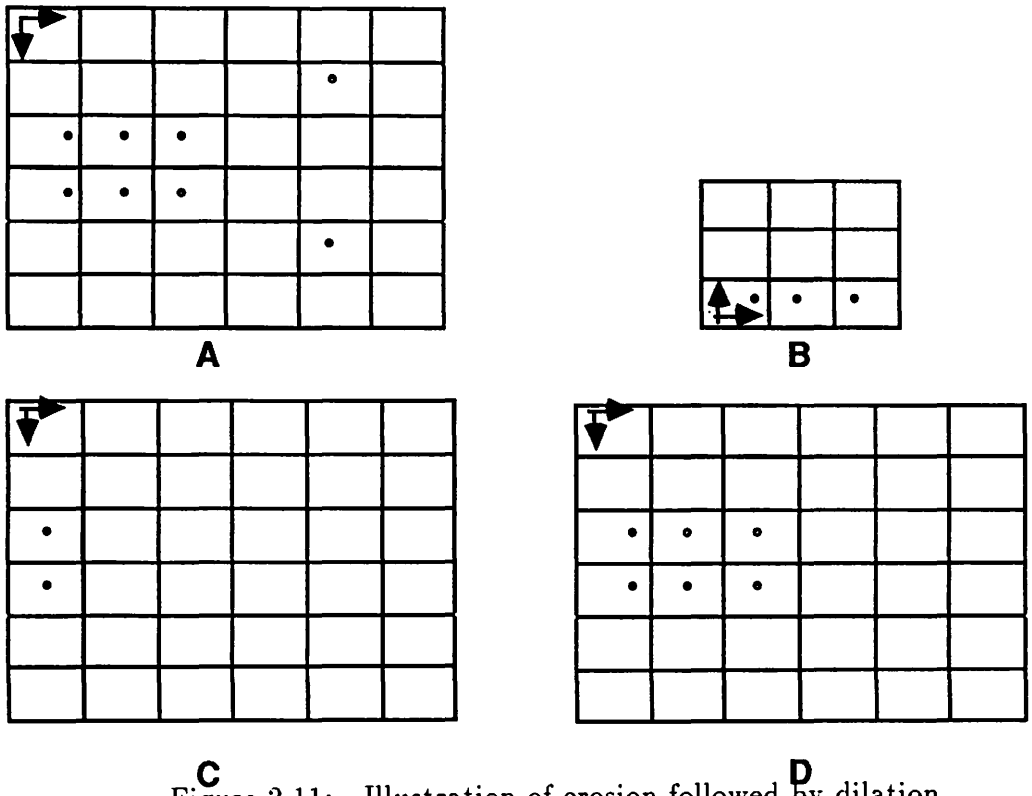

Figure 2.11: Illustration of erosion followed by dilation

filters of conventional linear filtering.

Definition O-1: The opening of image **A** by structuring element **B** is denoted by **A** $\circ$ **B** and is defined as:

$$\mathbf{A} \circ \mathbf{B} = (\mathbf{A} \ominus \mathbf{B}) \oplus \mathbf{B}. \tag{2.25}$$

Figure 2.11 is an illustration of opening where it was possible to eliminate isolated bright pixels from the image. Figure 2.12 is another example of opening where the intent is to eliminate all those regions in the image where a circle of unit radius will not fit. **A** is the image and **B** is a circle of unit radius. **C** gives the eroded image and **D**, the opened image. Notice how the edges of the image got rounded off due to opening.

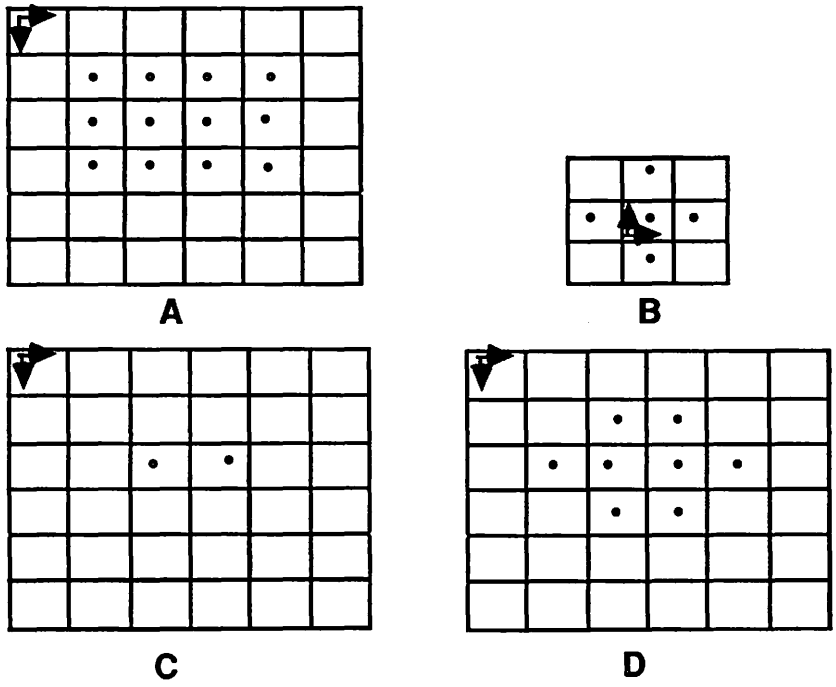

Figure 2.12: Illustration of opening

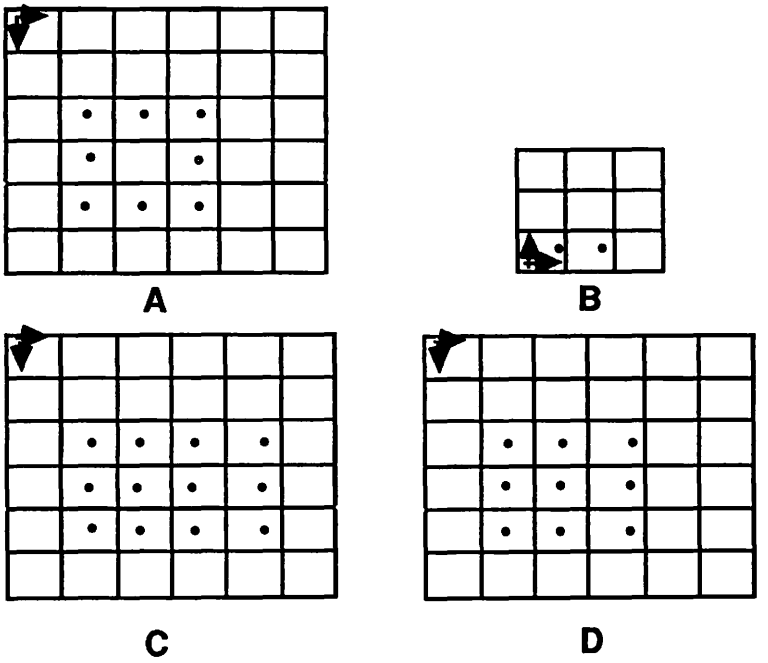

Figure 2.13: Illustration of closing

Definition C-1: The closing of image **A** by structuring element **B** is denoted by **A** • **B** and is defined as:

$$\mathbf{A} \bullet \mathbf{B} = (\mathbf{A} \oplus \mathbf{B}) \ominus \mathbf{B}. \tag{2.26}$$

Figure 2.13 illustrates closing. **A** is the original image in which there is a dark pixel surrounded by bright pixels. **B** is the structuring element. **C** is the result of dilating **A** by **B**. **D** is the closed image. Notice how the dark pixel has been removed from the image. Thus, opening and closing are controllable filtering operations, where we can eliminate bright and dark features respectively from the image.

Properties of Opening and Closing

Property O-1: Opening transformation is antiextensive. This implies that the opening of **A** by **B** is necessarily contained in **A**, regardless of whether or not the origin belongs to **B**.

$$\mathbf{A} \circ \mathbf{B} \subseteq \mathbf{A}. \tag{2.27}$$

Property O-2: It follows from the increasing property of erosion and dilation that opening is an increasing transformation. If $\mathbf{A}_1 \subseteq \mathbf{A}_2$, then $\mathbf{A}_1 \circ \mathbf{B} \subseteq \mathbf{A}_2 \circ \mathbf{B}$.

Property O-3: An image once opened by a structuring element remains unchanged by any further openings with the same structuring element. This is the idempotence property of opening.

$$\mathbf{A} \circ \mathbf{B} = (\mathbf{A} \circ \mathbf{B}) \circ \mathbf{B}. \tag{2.28}$$

Property C-1: The closing transformation is extensive. This means that closing of **A** by structuring element contains **A** regardless of whether or not **B** contains its origin.

$$\mathbf{A} \subseteq \mathbf{A} \bullet \mathbf{B}. \tag{2.29}$$

Property C-2: Closing is an increasing transformation. If $\mathbf{A}_1 \subseteq \mathbf{A}_2$, then $\mathbf{A}_1 \bullet \mathbf{B} \subseteq \mathbf{A}_2 \bullet \mathbf{B}$.

Property C-3: Closing transformation exhibits idempotence.

$$\mathbf{A} \bullet \mathbf{B} = (\mathbf{A} \bullet \mathbf{B}) \bullet \mathbf{B}. \tag{2.30}$$

CHAPTER 3. GRAY-SCALE MORPHOLOGY

Binary morphology has severe limitations. The growth of morphology as a discipline was handicapped by its incapability of handling multi-level images. Images had to be thresholded into two regions, bright and dark, before applying morphological processing. This narrows the spectrum of images on which morphology could be applied. It is extremely difficult to threshold the NDE x-ray images we are working on and retain all the essential information. Gray-scale morphology started taking shape in the late seventies and early eighties with major contributions from Sternberg (1980 and 1982) and Nakagawa and Rosenfeld (1978). The binary morphological operations of dilation, erosion, opening, and closing are all naturally extended to gray-scale imagery by the use of *min* and *max* operators. Nakagawa and Rosenfeld (1978) first discussed the use of neighborhood min and max operators. The general extension by Sternberg (1980 and 1982) strictly adhered to all the algebraic properties of binary morphology. Peleg and Rosenfeld (1981) used gray-scale morphology to generalize the medial axis transform to gray scale imaging. Werman and Peleg (1985) used gray scale morphology for texture feature extraction. Coleman and Sampson (1986) used gray scale morphology on range data imagery to help mate a robot to an object.

The principles of mathematical morphology are applicable to sets in Euclidean or digital spaces without regard to its dimension. The extension from binary images

to gray-scale images requires the introduction of the concepts of three-dimensional binary image, umbra and top surface.

Three Dimensional Binary Image

Consider a gray-scale image with x,y as the integral spatial coordinates and the intensity values in the z domain. Let there be 256 gray scale levels. This entire three-dimensional space is then divided into cubes. That is at each x,y, there will be a column of cubes above it, called a cube stack. So a 100×100 image will have $100 \times 100 \times 256$ cubes. For each x, y, the numeral one is place in the cube corresponding to the intensity value at that location. After placing a one in one cube for each x,y, all the other cubes in this cube stack are filled with zeros to give the three-dimensional image. For instance, if at $x = 50$, $y = 50$, the intensity is 75, then a one is place in the cube in the stack corresponding to this intensity. All other cubes in this stack are filled with zeros. Chackalackal and Basart (1990) introduced the concept of a three-dimensional binary image to simplify the extension of binary to gray-scale morphology. Figure 3.1 illustrates the concept of a three dimensional binary image showing one cube stack.

Top Surface and Umbra

Definition 1: Let $\mathbf{A} \subseteq \mathbf{E}^3$ and $\mathbf{F} = \{x, y \in \mathbf{E}^2 \mid \textit{for some } z \in \mathbf{E}, (x, y, z) \in \mathbf{A}\}$. Here $\mathbf{E}$ stands for Euclidean space. and $\mathbf{F}$ stands for the spatial domain of $\mathbf{A}$. The top surface of $\mathbf{A}$, denoted by $\mathbf{T}[\mathbf{A}] : \mathbf{F} \rightarrow \mathbf{E}$, is defined by:

$$\mathbf{T}[\mathbf{A}](x, y) = max \{z \mid (x, y, z) \in \mathbf{A}\}. \tag{3.1}$$

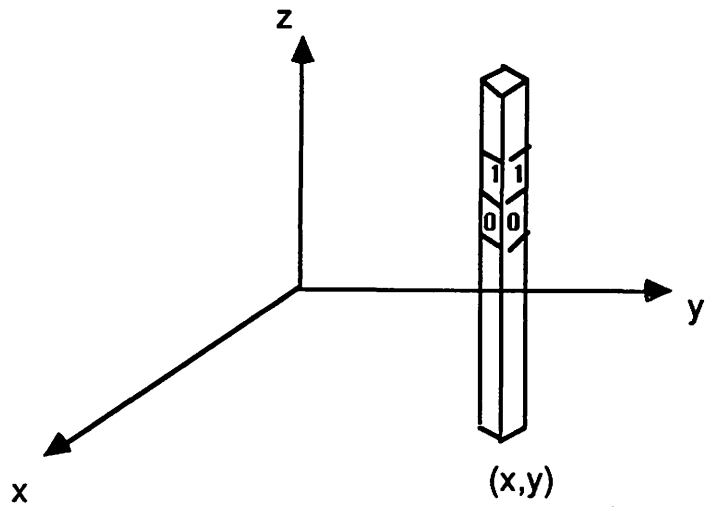

Figure 3.1: One cube stack in 3-D binary image

In other words, the top surface is the surface passing through all the ones in the three-dimensional image.

Defintion 2: Let $\mathbf{F} \subseteq \mathbf{E}^2$ and $a : \mathbf{F} \rightarrow \mathbf{E}$ where $\mathbf{F} = \{x, y \in \mathbf{E}^2 \mid \textit{for some } z \in \mathbf{E}, (x, y, z) \in \mathbf{A}\}$. The umbra of a, denoted by $\mathbf{U}[a]$, $\mathbf{U}[a] \subseteq \mathbf{F} \times \mathbf{E}$, is defined by:

$$\mathbf{U}[a] = \{(x, y, z) \in \mathbf{F} \times \mathbf{E} \mid z \leq a(x, y)\}. \tag{3.2}$$

Here $a(x,y)$ is the gray scale intensity at (x,y) and is a mapping from the spatial domain ($\mathbf{F}$) to the intensity (z) domain. $\mathbf{F} \times \mathbf{E}$ is the mapping from the spatial domain to the intensity domain. Hence, $a(x,y)$ is the function defining the top surface of $\mathbf{A}$. This is the definition given by Haralick et al. (1987). If the zero in every cube under the top surface in a three dimensional binary image is replaced by a one, then the set consisting of all the ones is called the umbra. In other words, the umbra is the set consisting of the top surface and everything below it. A vertical slice of a three dimensional binary image showing intensity versus position is shown in Figure 3.2. It

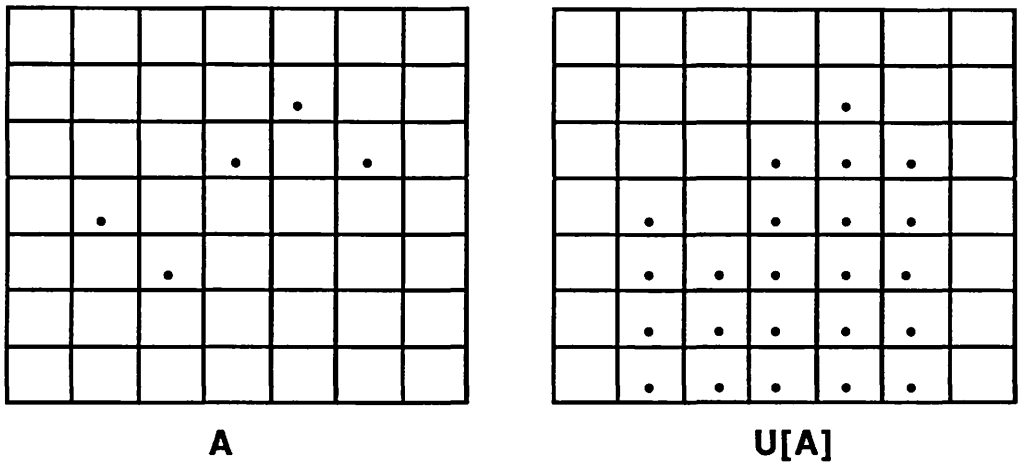

Figure 3.2: Umbra of a function

is a one-dimensional plot of the function a(x,y). The cells with the dots in them are those cells in which the ones are placed to form the three-dimensional binary image. Figure 3.2 also gives the umbra of the function.

Gray Scale Dilation

Definition3: Let $\mathbf{F}, \mathbf{K} \subseteq \mathbf{E}^2$ and $a : \mathbf{F} \rightarrow \mathbf{E}$, $b : \mathbf{K} \rightarrow \mathbf{E}$. $\mathbf{K}$ denotes the spatial domain of the structuring element **B**. The dilation of a by b, is denoted by $a \oplus b, is a \oplus b : \mathbf{F} \oplus \mathbf{K} \rightarrow \mathbf{E}$, and is defined by:

$$a \oplus b = \mathbf{T}[\mathbf{U}[a] \oplus \mathbf{U}[b]]. \tag{3.3}$$

Here **F** and **K** are subsets of the spatial domain and a and b are mappings from the spatial domain to the intensity domain. Basically, a and b are functions defining the top surface or the intensities of **A** and **B**. According to this definition, a(x,y) dilated

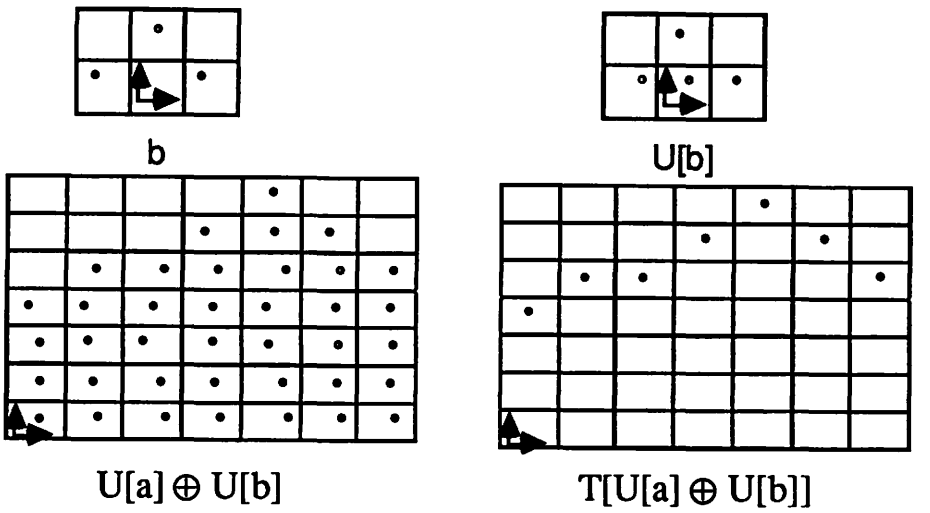

Figure 3.3: Illustration of dilation using an umbra

by $b(x,y)$ is the top surface of the dilation of the umbras of a and b. Figure 3.3 illustrates this definition. The figure shows the one-dimensional function b and its umbra. The dilation of the umbras and the top surface of the dilation of the umbras are also shown.

This method of gray scale dilation by taking the top surfaces of dilation of umbras is time consuming as it involves translating every element in **U**[a] by every element in **U**[b]. For instance, if **A** is a 50 $\times$ 50 image and **B** is a 3 $\times$ 3 image, then $\mathbf{A} \oplus \mathbf{B}$ could require as many as $50 \times 50 \times 256 \times 9$ translations. It will be shown in Theorem 1 that only the surface elements of **A** and **B** contribute to the final result. Thus, the gray scale dilation of **A** by **B** is given by:

$$\mathbf{A} \oplus \mathbf{B} = \mathbf{T}[\mathbf{T}[\mathbf{A}] \oplus \mathbf{T}[\mathbf{B}]]. \tag{3.4}$$

This property is illustrated in Figure 3.4. The image and the structuring element are the same as used in Figure 3.3. Instead of dilating the umbras, we just dilate the top

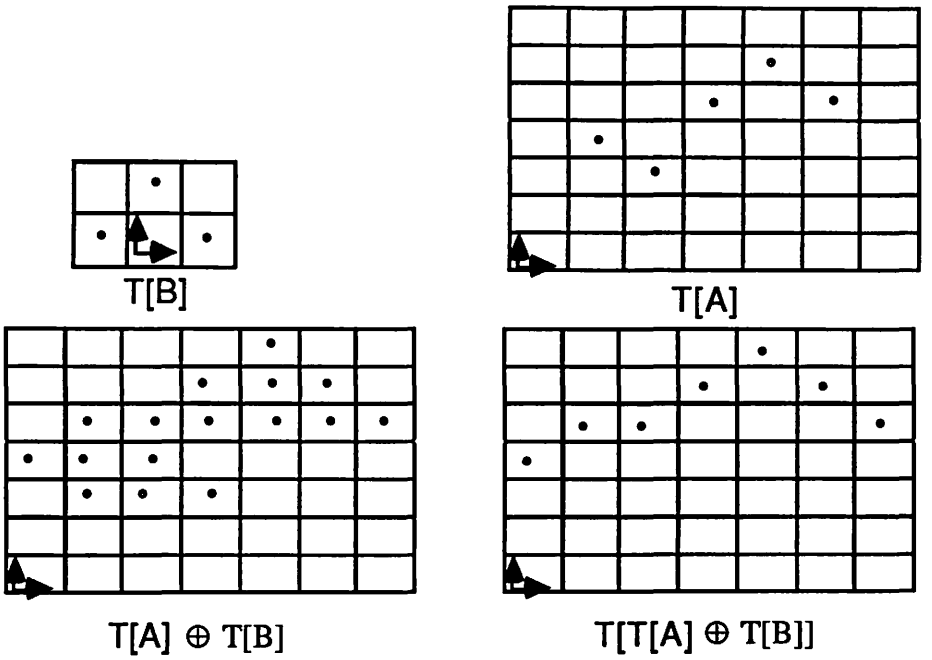

Figure 3.4: Illustration of gray scale dilation using the top surface elements

surfaces. The final dilated result is obtained by taking the top surface of the dilation of the top surfaces. The final dilated image is the same as the result in Figure 3.3.

Theorem 1: Let $a : \mathbf{F} - \mathbf{E}$ and $b : \mathbf{K} - \mathbf{E}$, where $\mathbf{F} = \{x, y \in \mathbf{E}^2 \mid$ *for some* $z \in \mathbf{E}, (x, y, z) \in \mathbf{A}\}$ and $\mathbf{K} = \{x, y \in \mathbf{E}^2 \mid$ *for some* $z \in \mathbf{E}, (x, y, z) \in \mathbf{B}\}$. Then $a \oplus b : \mathbf{F} \oplus \mathbf{K}$ can be computed by:

$$c(x,y) = \max_{\substack{i,j \in \mathbf{K} \\ x-i, y-j \in \mathbf{F}}} \{a(x-i, y-j) + b(i,j)\}. \tag{3.5}$$

where c(x, y) is the gray scale intensity of the dilated image at (x, y).

Proof: We have $c = (a \oplus b)(x, y)$. Then $c = \mathbf{T}[\mathbf{U}[a] \oplus \mathbf{U}[b]](x, y)$. By definition of

top surface,

$$c = max\ \{z \mid (x, y, z) \in [\mathbf{U}[a] \oplus \mathbf{U}[b]]\}. \tag{3.6}$$

By definition of dilation,

$$\begin{aligned} c &= max\ \{u + v \mid for\ some\ i,j \in \mathbf{K}\ satisfying \\ &\quad x - i, y - j \in \mathbf{F}, (x - i, y - j, u) \in \mathbf{U}[a]\ and\ (i, j, v) \in \mathbf{U}[b]\}. \end{aligned}$$

By definition of umbra, the largest u such that $(x - i, y - j, u) \in \mathbf{U}[a]$ is $u = a(x - i, y - j)$. Likewise, the largest v such that $(i, j, v) \in \mathbf{U}[b]$ is $v = b(i, j)$. Hence

$$\begin{aligned} c &= max\ \{a(x - i, y - j) + b(i, j) \mid (i, j) \in \mathbf{K}, (x - i, y - j) \in \mathbf{F}\} \\ &= \max_{\substack{i,j \in \mathbf{K} \\ x-i, y-j \in \mathbf{AF}}} \{a(x - i, y - j) + b(i, j)\}. \end{aligned}$$

Algorithm 1: An algorithm that implements gray scale dilation is shown pictorially in Figure 3.5. **A** represents a 5×5 image and **B** represents a 3×3 structuring element. The x, y plane is shown and the numbers represent the intensity at that particular x, y. The origin of **B**, represented by the circled number, is at the center in the square box. The origin of **A** is at the upper left corner. The origin of **B** is made to coincide with the center element of **A**. Ignoring all the other elements in **A** for the moment, we translate the center element by all the elements in **B** as shown in Figure 3.5c. Translating is done by adding each of the elements in **B** to the center element in **A** and storing the result in the respective position as shown in Figure 3.5d. The origin of **B** is then made to coincide with the element to the right of the center element of **A** as shown in Figure 3.5e. The result of translating this element by **B** is shown in Figure 3.6f. The process is repeated for all other inner elements in **A**, resulting in nine sets of translates. Since **B** is a 3×3 mask, we ignore the boundary

elements as we do not want the mask to fall outside **A**. The maximum intensity at each corresponding pixel location in the nine set of translates is retained to give the final dilated image. The process can be initiated by placing the mask at any location in the image.

Dilating a gray scale image causes the brighter regions in an image to grow. Brighter is a relative term and it represents regions brighter than the background. At the same time it causes regions darker than the background to shrink. For the process of dilation, we need an image and a three-dimensional structuring element. Figure 3.6 illustrates a real life application of gray scale dilation. The picture on the left is a digitized radiograph of a Westinghouse composite material. The bright dot-like features are flaws. This image was dilated by a 9×9 hemispherical structuring element to obtain the image on the right. Notice how the flaws have grown with respect to the background. The flaws have been magnified while maintaining the image at the same size. The growth of the flaws depends on the size of the structuring element. The larger the size of the structuring element, the larger will be the growth of the bright regions.

Gray Scale Erosion

Definition4: Let $\mathbf{F}, \mathbf{K} \subseteq \mathbf{E}^2$ and $a : \mathbf{F} \rightarrow \mathbf{E}$, $b : \mathbf{K} \rightarrow \mathbf{E}$. The erosion of a by b is denoted by $a \ominus b$, $a \ominus b : \mathbf{F} \ominus \mathbf{K} \rightarrow \mathbf{E}$, and is defined by:

$$a \ominus b = \mathbf{T}[\mathbf{U}[a] \ominus \mathbf{U}[b]]. \tag{3.7}$$

Here $\mathbf{F}$ and $\mathbf{K}$ are subsets of the spatial domain and a, b are mappings from the spatial domain to the intensity domain. Basically, a and b are functions defining the

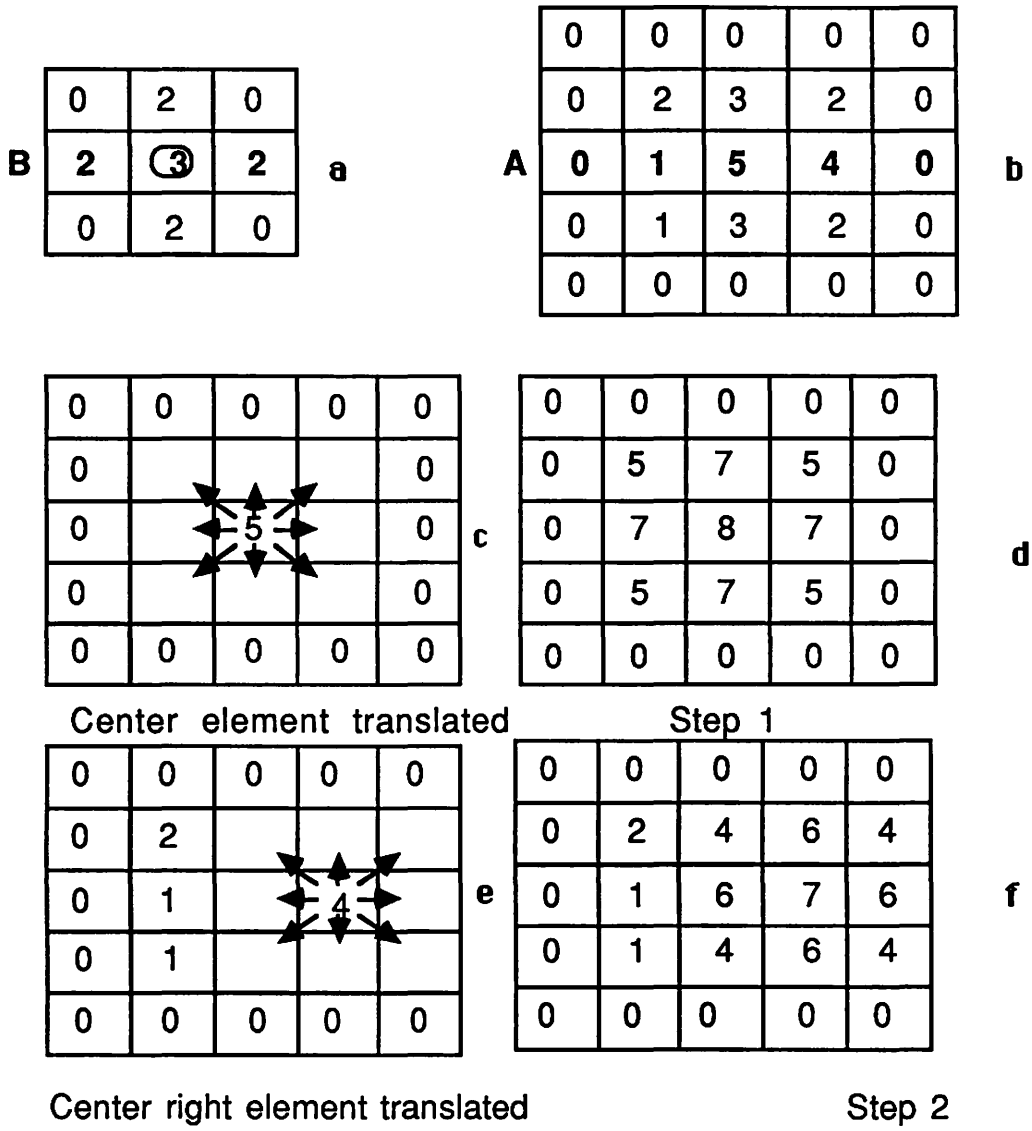

Continue for seven more translations. and take the maximum intensity at each pixel location from the nine sets of translates.

Figure 3.5: Illustration of gray-scale dilation

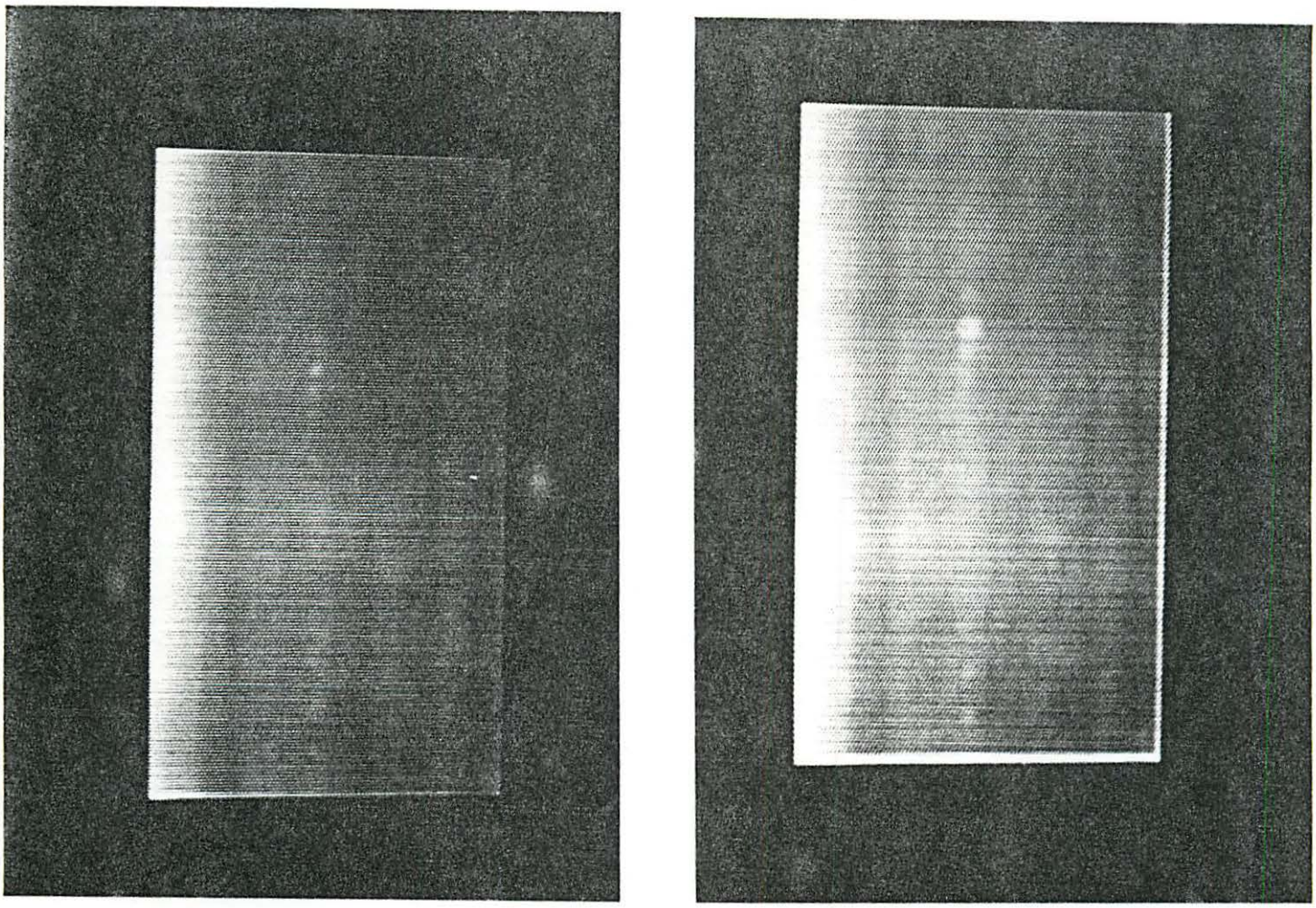

Figure 3.6: The picture on the left is the digitized image of a Westinghouse radiograph (Courtesy of Westinghouse). The one on the right is the dilated image

top surface or the intensities of **A** and **B**. According to this definition, *a(x,y)* eroded by *b(x,y)* is the top surface of the erosion of umbra of *a* by umbra of *b*. Figure 3.7 illustrates this definition. The functions *a* and *b* are the same as used in Figure 3.3. The figure gives the result of eroding the umbra of *a* by the umbra of **b**. The final eroded image is obtained by taking the top surface of $\mathbf{U}[a] \ominus \mathbf{U}[b]$. As in the case of gray scale dilation, gray scale erosion by taking the top surface of the erosion of the umbras is time consuming as it involves the vector subtraction of every element in **U**[a] by every element in **U**[b]. It will be shown in Theorem 2 that only the surface elements of **A** and **B** contribute to the final result. Thus, the gray scale erosion of **A** by **B** is given by:

$$\mathbf{A} \ominus \mathbf{B} = \mathbf{T}[\mathbf{T}[\mathbf{A}] \oplus \mathbf{T}[\mathbf{B}]]. \tag{3.8}$$

Instead of eroding the umbras, we just erode the top surfaces. The eroded image is obtained by taking the top surface of the erosion of the top surfaces.

Theorem 2: Let $a : \mathbf{F} - \mathbf{E}$ and $b : \mathbf{K} - \mathbf{E}$, where $\mathbf{F} = \{x, y \in \mathbf{E}^2 \mid \textit{for some } z \in \mathbf{E}, (x, y, z) \in \mathbf{A}\}$ and $\mathbf{K} = \{x, y \in \mathbf{E}^2 \mid \textit{for some } z \in \mathbf{E}, (x, y, z) \in \mathbf{B}\}$. Then $a \ominus b : \mathbf{F} \ominus \mathbf{K}$ can be computed by:

$$c(x, y) = \min_{\substack{i,j \in \mathbf{K} \\ x+i, y+j \in \mathbf{F}}} \{a(x + i, y + j) + b(i, j)\}. \tag{3.9}$$

where c(x, y) is the gray scale intensity of the eroded image at (x, y).

Proof: We have $c = (a \ominus b)(x, y)$. Then $c = \mathbf{T}[\mathbf{U}[a] \ominus \mathbf{U}[b]](x, y)$. By definition of top surface,

$$c = max \{z \mid (x, y, z) \in [\mathbf{U}[a] \ominus \mathbf{U}[b]]\}. \tag{3.10}$$

By definition of erosion,

$$c = max \{z \mid \textit{for every } (i, j, k) \in \mathbf{U}[b],$$

$$(x, y, z) + (i, j, k) \in \mathbf{U}[a]\}.$$

By definition of umbra,

$$\begin{aligned} c &= max\ \{z \mid for\ every\ i, j \in \mathbf{K}, k \leq b(i,j), \\ &\quad z + k \leq a(x+i, y+j)\} \\ &= max\ \{z \mid for\ every\ i, j \in \mathbf{K}, k \leq b(i,j), \\ &\quad z \leq a(x+i, y+j) - k\}. \end{aligned}$$

But $z \leq a(x+i, y+j) - k$ *for every* $k \leq b(i,j)$ implies $y \leq a(x+i, y+j) - b(i,j)$. Hence,

$$c = max\ \{z \mid\ for\ every\ i, j \in \mathbf{K}, z \leq a(x+i, y+j) - b(i,j)\}. \tag{3.11}$$

But $z \leq a(x+i, y+j) - b(i,j)$ for every $i, j \in \mathbf{K}$ implies

$z \leq min_{i,j \in \mathbf{K}}[a(x+i, y+j) - b(i,j)]$.

Now,

$$\begin{aligned} c &= max\ \{z \mid z \leq min_{i,j \in \mathbf{K}}[a(x+i, y+j)] - b(i,j)]\} \\ &= min_{\substack{i,j \in \mathbf{K} \\ x+i, y+j \in \mathbf{F}}} [a(x+i, y+j) - b(i,j)] \end{aligned}$$

Algorithm 2: An algorithm that performs gray-scale erosion is shown pictorially in Figure 3.7. **A** represents a 5×5 image and **B** represents a 3×3 structuring element. The *x*,*y* plane is shown and the numbers represent the intensity at that particular *x*,*y*. The origin of **B**, represented by the circled number, is at the center in the square box. The origin of **B** is made to coincide with the center element of **A** as shown in Figure 3.8c. Ignoring all the other elements in **A**, we take the negative translates

of the center element by the elements in **B**. Negative translating is done by vector subtracting each of the elements in **B** from the center element in **A** and storing the result at the corresponding location as shown in Figure 3.8d. The process is repeated for all other inner elements in **A**, to give nine sets of negative translates. For each corresponding pixel location in the nine sets, the intensity values in the nine sets of negative translates are compared and the minimum intensity at each pixel is retained. The process can be initiated by placing the mask at any location in the image.

Eroding a gray scale image causes the regions darker than the background to grow. At the same time it causes regions brighter than the background to shrink. Figure 3.8 illustrates a real life application of gray scale erosion. The picture on the left is a digitized radiograph of a pipe. There are two transverse cracks on the image. The image was eroded by a 7×7 hemisphere. Notice how the flaws have grown with respect to the background.

Boundary Effect: If the size of the structuring element is $n \times n$ (n being odd), then a region with thickness (n-1)/2 is left intact along the boundary. The structuring element is not centered at any pixel in this region. This prevents the structuring element from falling outside the image domain. Thus, the morphological operations do not affect the pixels in the boundary region. Consequently, it is not possible to extract information from the boundary region.

Structuring Elements

In morphological image processing, the image to be processed and the structuring element are an inseparable pair. The description of a morphological operation is not complete without specifying the structuring element. Consider the case of a

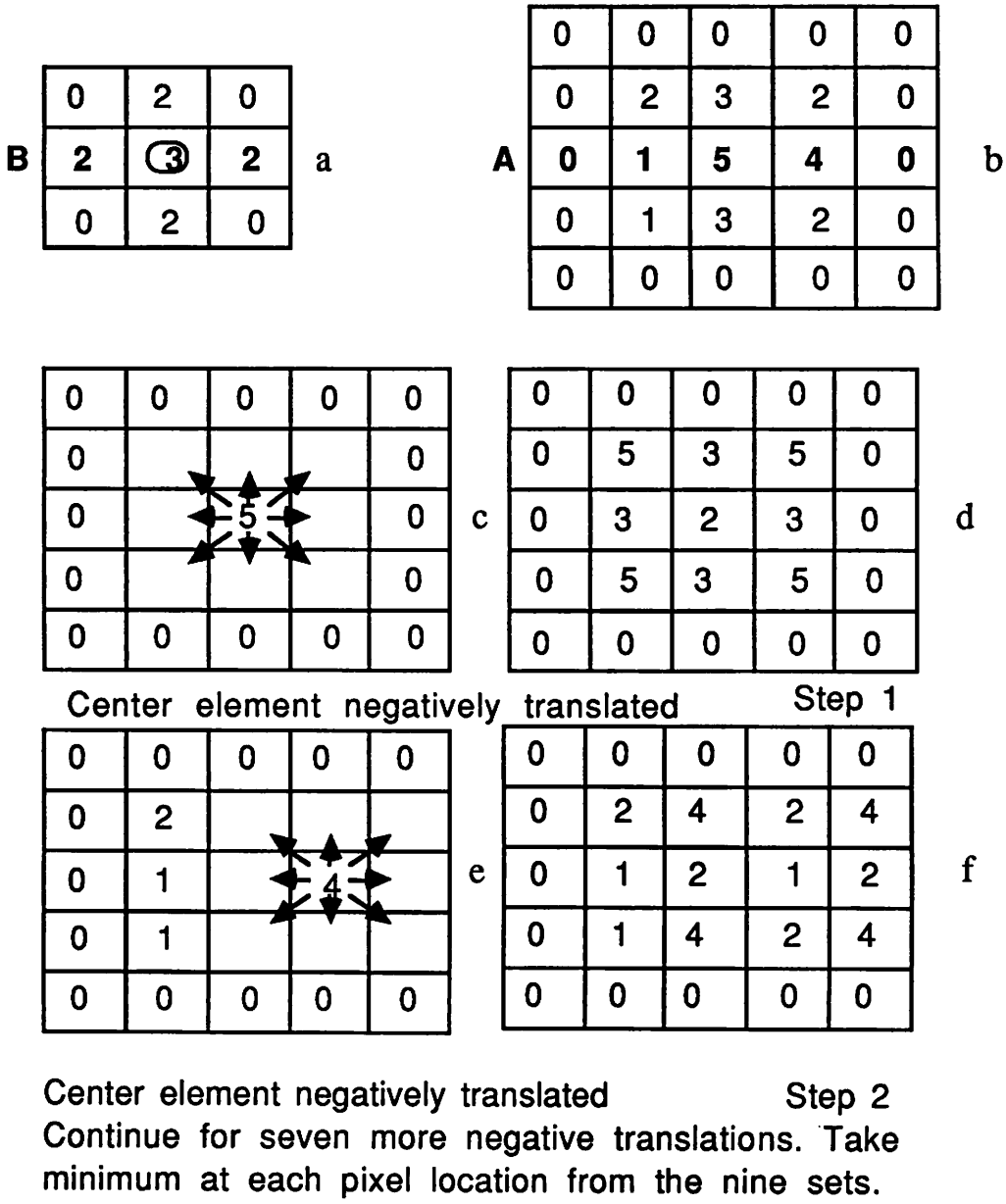

Figure 3.7: Illustration of gray scale erosion

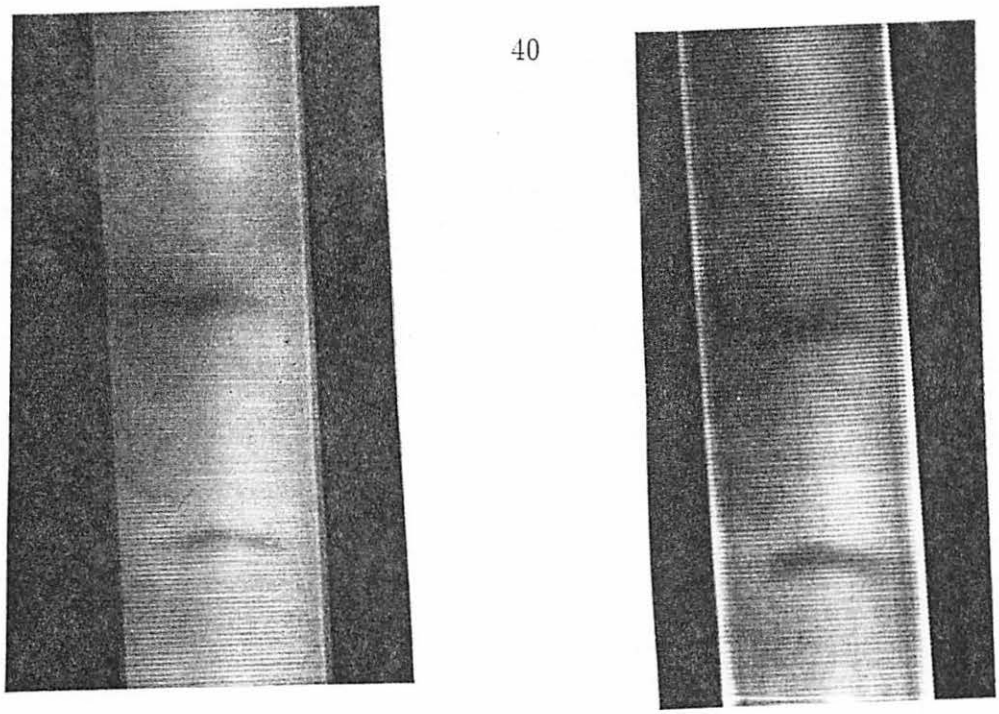

Figure 3.8: The picture on the left is a digitized image of a pipe (Courtesy of Atlantic Richfield Corporation). The one on the right is the eroded image

mechanic trying to unscrew a bolt given a ratchet and various sockets. To a person doing image analysis, mathematical morphology is his ratchet, and the structuring elements in a variety of shapes and sizes are the sockets. Like unscrewing a bolt, the person has to determine the right structuring element that will extract the required information. Thus, in applications of pattern recognition, feature extraction, the choice of structuring elements play a crucial role.

In gray scale morphology, the structuring element could be any three dimensional structure. Cones, cylinders, hemispheres and paraboloids were investigated for various images. The designations of $n \times n$ (e.g. 9×9) for a hemispherical structuring element means that the spatial dimensions are $n \times n$ and the intensity over this region varies as a hemisphere. In Figure 1.6, it was mentioned that the image was dilated by a 9×9 hemispherical structuring element. The center of the $n \times n$ mask

corresponds to the maximum intensity of the hemisphere. The 9×9 mask is shown in two dimensions in Figure 3.9, and in three dimensions in Figure 3.10.

For the image in Figure 3.6, the growth in the bright spots increases as the size of the mask increases. The expression for finding the elements in the $n \times n$ hemispherical mask is given by:

$$w(x,y) = g^2 - (gx/k)^2 - (gy/k)^2 \tag{3.12}$$

where $w(x,y)$ is the intensity at location (x,y),

g is the peak intensity at the center of the mask (0,0),

x lies in the range $[-k,k]$ and y lies in the range $[-k,k]$,

$k = (n\text{-}1/2)$.

The algorithm for finding the elements in a $n \times n$ cylindrical mask is given by:

$$If \;\; x^2 + y^2 \leq k^2 then \;\; w(x,y) = g else \;\; w(x,y) = 0. \tag{3.13}$$

where g is the height of the cylinder. Also note that the mask size is always an odd number. The criteria for selection of structuring elements are discussed later.

Decomposition of Structuring Elements

Man has never been content with the speed at which he could accomplish any task. Fast cars, planes and computers are living legacies to his relentless pursuit to break the time barrier. So it is not the least surprising when he wants to process images in real time. Morphological routines can be time consuming depending on the size of the image processed and to a greater extent on the size of the structuring element. For instance, if we want to dilate an image by a 3×3 structuring element,

0	0	0	0	0	0	0	0	0
0	0	4	6	6	6	4	0	0
0	4	6	7	8	7	6	4	0
0	6	7	8	9	8	7	6	0
0	6	8	9	9	9	8	6	0
0	6	7	8	9	8	7	6	0
0	4	6	7	8	7	6	4	0
0	0	4	6	6	6	4	0	0
0	0	0	0	0	0	0	0	0

Figure 3.9: 9×9 mask representing a hemisphere. The height of the hemisphere is nine and the origin is at the center of the mask

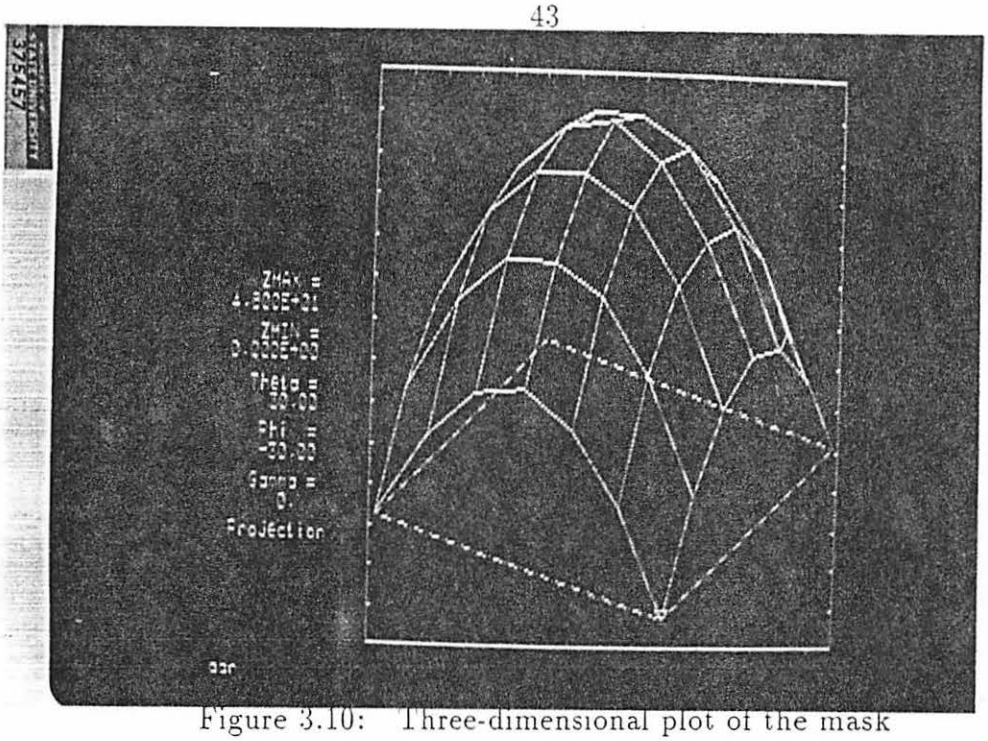

Figure 3.10: Three-dimensional plot of the mask

each pixel in the image generates 9 translates. But if the same image is dilated by a 15×15 structuring element, each pixel generates 225 translates. Thus, there is almost an exponential increase in computational time with increase in size of structuring element.

Decomposition of structuring elements can be used to reduce computational time drastically. Decomposition of symmetrical structuring elements is just a mathematical exercise. The theory underlying decomposition of structuring elements is given by Theorem-3.

Theorem-3: If the structuring element $\mathbf{B}$ has the decomposition $\mathbf{B} = \mathbf{B}_1 \oplus \mathbf{B}_2 \cdots \oplus \mathbf{B}_N$. Then, the dilation and erosion of $\mathbf{A}$ by $\mathbf{B}$ can be performed respectively as

$$\mathbf{A} \oplus \mathbf{B} = \mathbf{A} \oplus (\mathbf{B}_1 \oplus \mathbf{B}_2 \cdots \oplus \mathbf{B}_N) = (((\mathbf{A} \oplus \mathbf{B}_1) \oplus \mathbf{B}_2) \cdots) \oplus \mathbf{B}_N. \quad (3.14)$$

$$\mathbf{A} \ominus \mathbf{B} = \mathbf{A} \ominus (\mathbf{B}_1 \oplus \mathbf{B}_2 \cdots \oplus \mathbf{B}_N) = (((\mathbf{A} \ominus \mathbf{B}_1) \ominus \mathbf{B}_2) \cdots) \ominus \mathbf{B}_N. \quad (3.15)$$

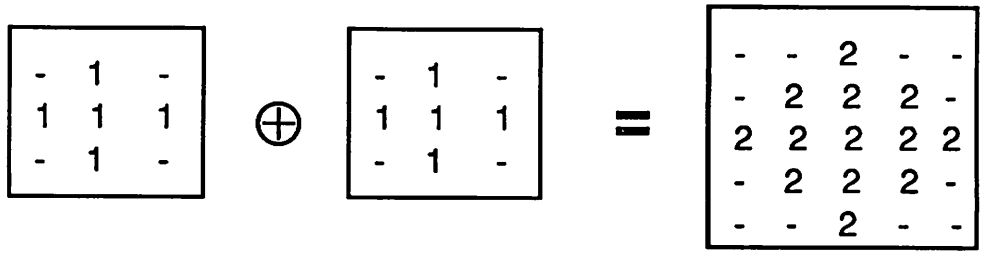

Figure 3.11: Decomposition of a 5×5 cylinder

The major problem in decomposing a structuring element is determining the N smaller structuring elements. Zhuang and Haralick (1986) discuss in detail the mathematics behind decomposing of structuring elements. Cylinder is the structuring element we use most in our work with NDE images and the justification is given later. A 5×5 cylinder can be expressed as the dilation of two 3×3 cylinders. Thsi implies that a 5×5 cylinder can be decomposed into two 3×3 cylinders as illustrated in Figure 12. This principle can be extended to a cylinder of any size. A 17×17 cylinder can be generated by eight repeated dilations with a 3×3 cylinder. Dilating by a 17×17 cylinder generates 289 translates for each pixel in the image, whereas repeated dilations by 3×3 cylinder generates 72 translates for each pixel.

CHAPTER 4. MORPHOLOGICAL FILTERS

Morphological filters are nonlinear signal transformations that locally modify geometric features of signals. Each signal is viewed as a set in a Euclidean space, and the morphological filters are set operations that transform the graph of the signal and can provide a quantitative description of its geometrical structure. The applications of morphological filters in image processing and analysis are numerous and are discussed by Serra (1982) and Maragos and Schafer (1986). Areas of application include biomedical image processing, automated industrial inspection, shape recognition, nonlinear filtering, edge detection, noise suppression, thinning, enhancement, representation and coding, texture anlysis and shape smoothing. A lot of research is currently going on in morphological filters. Maragos and Schafer (1987) introduce the representation of classical linear filters in terms of morphological operators. Chen and Yan (1987) prove why mathematical morphology is more powerful in studying some vision problems than using derivatives of Gaussian-shaped filters of different sizes. Song and Delp (1989) propose a new class of morphological filters, known as the generalized morphological filter, for image enhancememt. This chapter introduces the concept of morphological filtering, hybrid filtering and sieving.

Opening and Closing

Opening and closing are the two morphological filters, referred to as M-filters by Lantuejoul and Serra (1982). As mentioned earlier, dilation and erosion are not inverse operations. Dilation of an image followed by erosion with the same structuring element will not yield the original image. Similarly, erosion followed by dilation will not yield the original image. This property is exploited in the designing of opening and closing.

Opening: The gray-scale opening of $\mathbf{A}$ by $\mathbf{B}$ is denoted by $\mathbf{A} \circ \mathbf{B}$ and is defined by:

$$\mathbf{A} \circ \mathbf{B} = (\mathbf{A} \ominus \mathbf{B}) \oplus \mathbf{B}. \tag{4.1}$$

Opening can also be defined as:

$$\mathbf{A} \circ \mathbf{B} = \cup(\mathbf{B})_y; \quad where(\mathbf{B})_y \subset \mathbf{A}. \tag{4.2}$$

where $(\mathbf{B})_y$ is the translation of $\mathbf{B}$ to a point y element of Euclidean space. The result of mathematical opening can be explained as the domain swept out by all the translations of $\mathbf{B}$ which are included in $\mathbf{A}$. Opening is somewhat like a nonlinear low-pass filter that removes features brighter than the background and smaller than the structuring element. However, it is not a low-pass filter. A low-pass filter would reject high spatial frequencies for both large and small structures. The process of opening is pictorially represented in Figure 4.1. Opening can be visualized as a process in which the structuring element is pushed pushed apex up under the top surface of the image and scanned along the image. The opened image consists of the highest points reached by structuring element at each pixel as it is slid under the top surface of the image. Figure 4.1 also shows slices through the image $\mathbf{A}$ and the cylindrical

structuring element **B**. The figure gives the plot of intensity versus position. Note how all the peaks that had a base width smaller than the radius of the structuring element were removed from the image. The larger peaks were slightly clipped at the top. Opening an image breaks narrow isthmuses, and eliminates small islands and sharp peaks or capes. Figure 4.2 shows The digitized radiograph of a Westinghouse composite with bright flaws. This image is opened by a 9×9 cylindrical structuring element. Notice how all the flaws disappeared from the opened image given in Figure 4.3.

Closing: The closing of **A** by **B** is denoted by $\mathbf{A} \bullet \mathbf{B}$ and is defined by:

$$\mathbf{A} \bullet \mathbf{B} = (\mathbf{A} \oplus \mathbf{B}) \ominus \mathbf{B}. \tag{4.3}$$

Closing can also be defined as:

$$\mathbf{A} \bullet \mathbf{B} = \cup(\mathbf{B})_y; \ \textit{where} \ (\mathbf{B})_y \subset \mathbf{A}^c. \tag{4.4}$$

Here $(\mathbf{B})_y$ is the translation of **B** to a point y in Euclidean space. Thus, closing can also be explained as the domain swept out by all the translations of **B** which are included in $\mathbf{A}^c$.

Closing an image fuses narrow breaks and long thin gulfs, eliminates small holes, and fills gaps. Closing behaves like a low-pass filter that removes features darker and smaller than the background. Closing can be visualized as a process in which we slide the structuring element, apex down, over the top surface of the structuring element. The closed image consists of the lowest points reached by the structuring element. Closing is pictorially represented in Figure 4.4. Closing removes all the pits smaller than the size of the structuring element. Larger pits are retained to a great extent

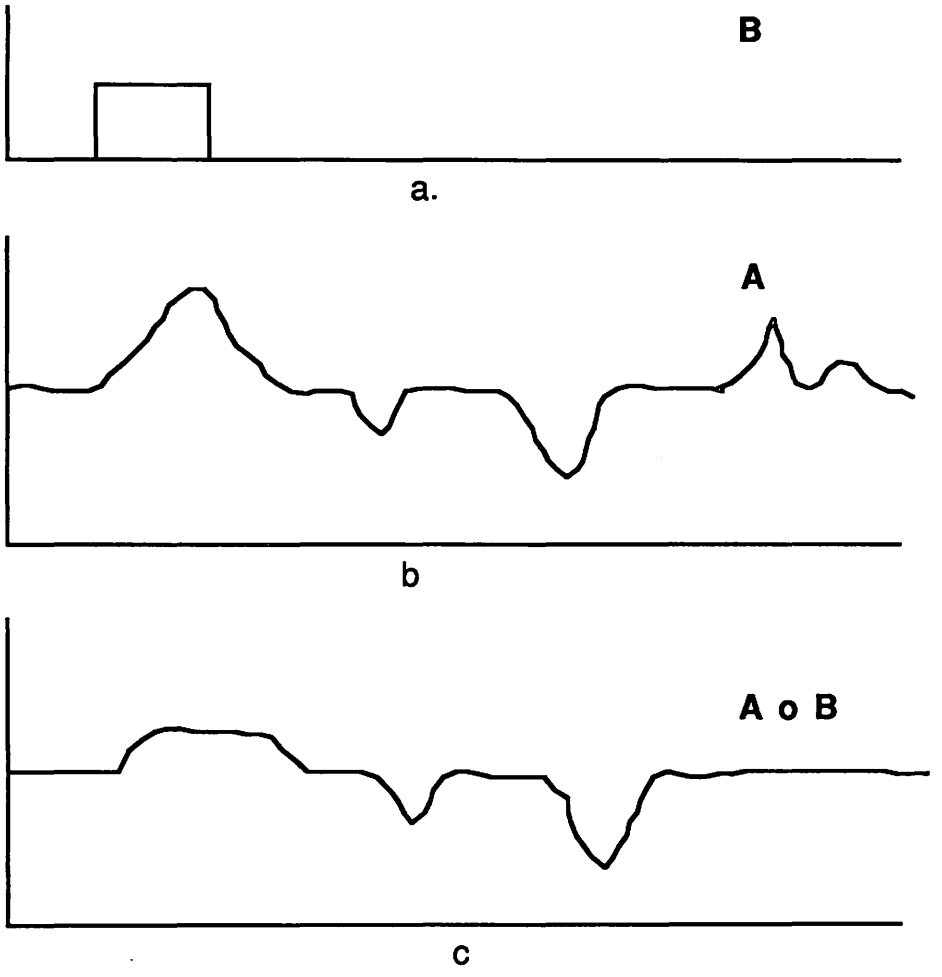

Figure 4.1: Pictorial Illustration of opening

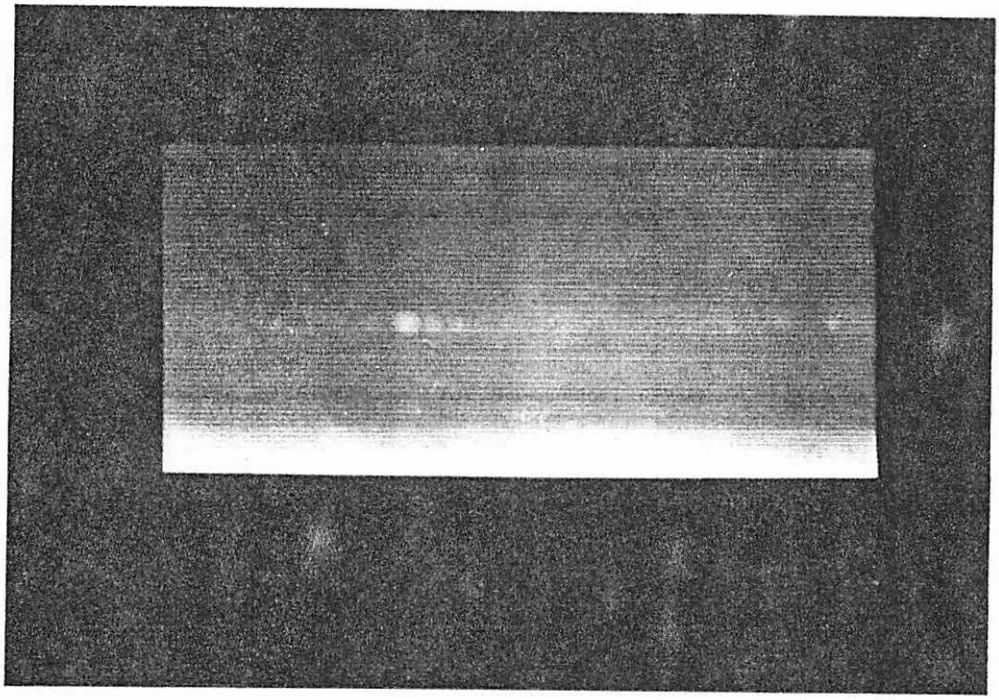

Figure 4.2: Digitized radiograph of a composite (Courtesy of Westinghouse)

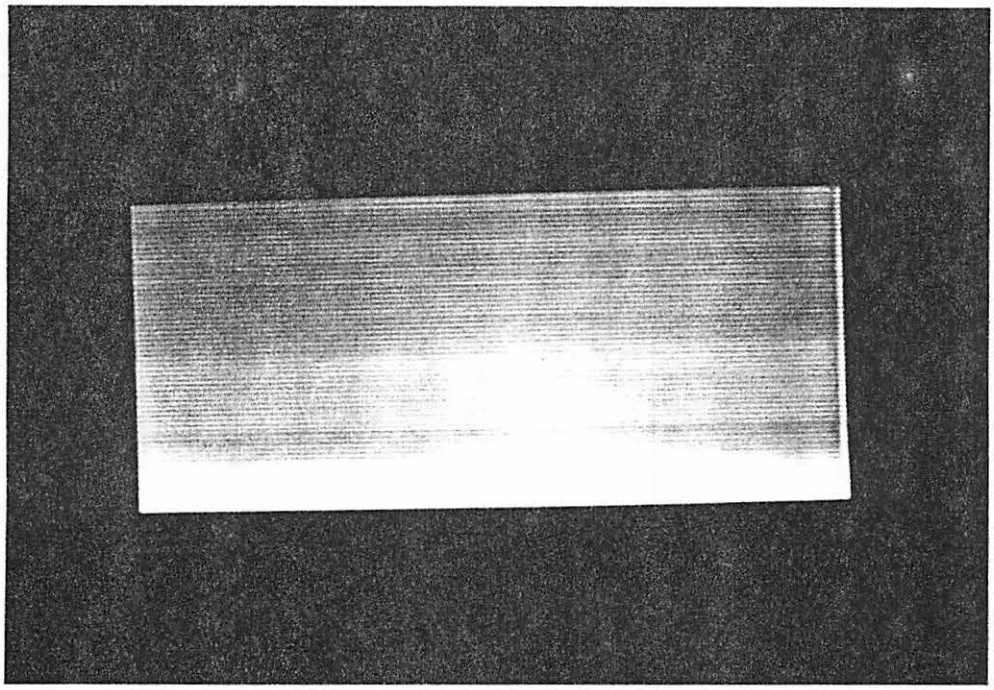

Figure 4.3: The image of composite opened by a 9×9 cylinder

except for clipping due to the nature of the structuring element. Figure 4.5 shows the digitized x-ray of a railroad frog with shrinkage cracks. This image is closed by a 25×25 cylinder to give the image in Figure 4.6. Notice how all the shrinkage cracks have been removed from the image.

Hybrid Filtering

The opening of an image by a structuring element cuts down the peaks in the image, whereas closing the image fills up the valleys. Thus, the positive noise spikes in an image can be removed by opening the image wiht a small structuring element (say 3×3). Similarly, the negative noise spikes can be suppressed by closing with a small structuring element. The cleaning effects of the opening-closing pair is utilized in the hybrid filter. The schematic of a hybrid filter is given in Figure 4.7. Figure 4.8 gives the digitized image of space shuttle fuel tank and a slice through the center of the image showing intensity versus position. The image is noisy as can be observed from the slice. Figure 4.9 shows the result of hybrid filtering the image in Figure 4.8 with a 5×5 hemisphere. The figure also includes a slice of the filtered image.

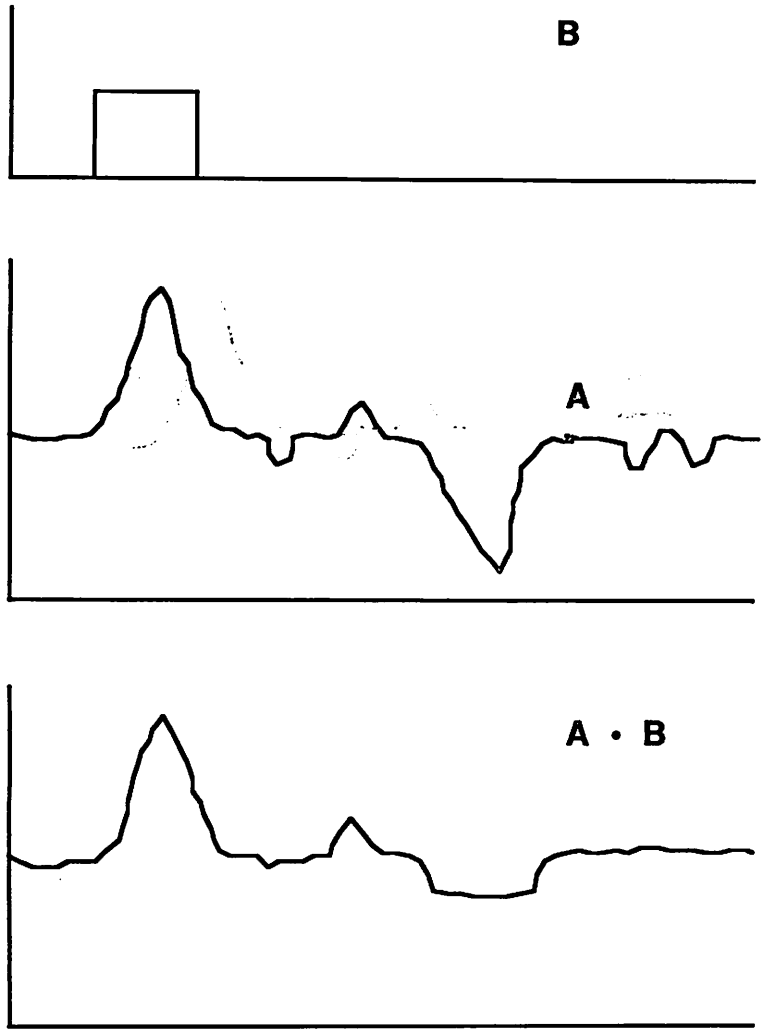

Figure 4.4: Illustration of closing

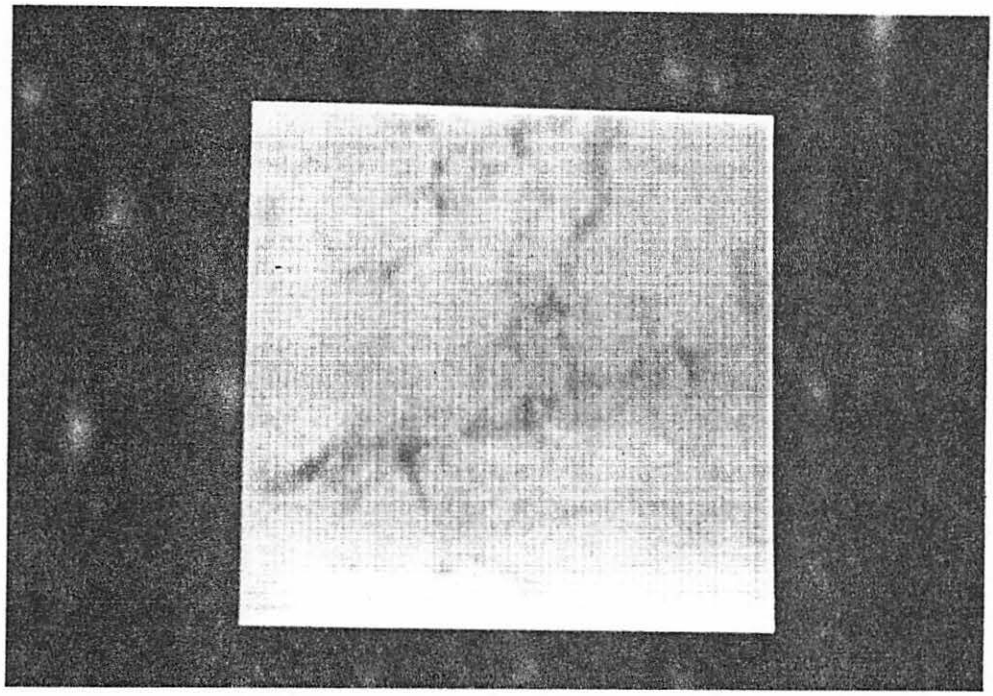

Figure 4.5: Digitized image of a frog (Courtesy of the American Association of Railroads)

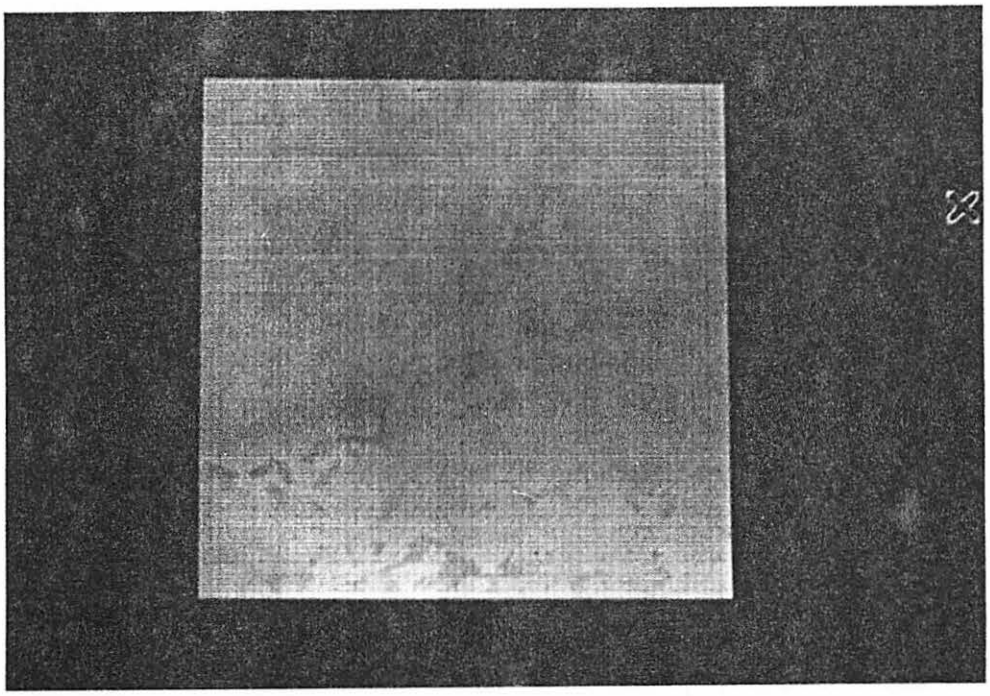

Figure 4.6: Image of frog closed by a 25×25 cylinder

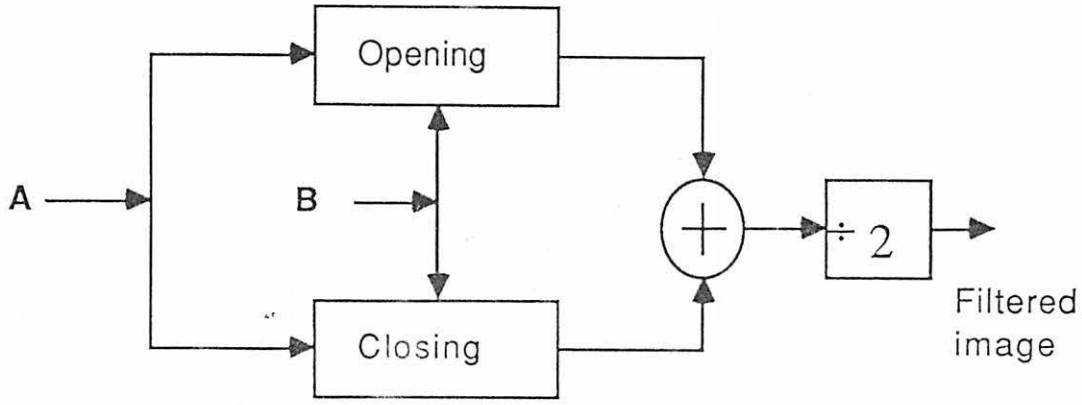

Figure 4.7: Schematic of a hybrid filter

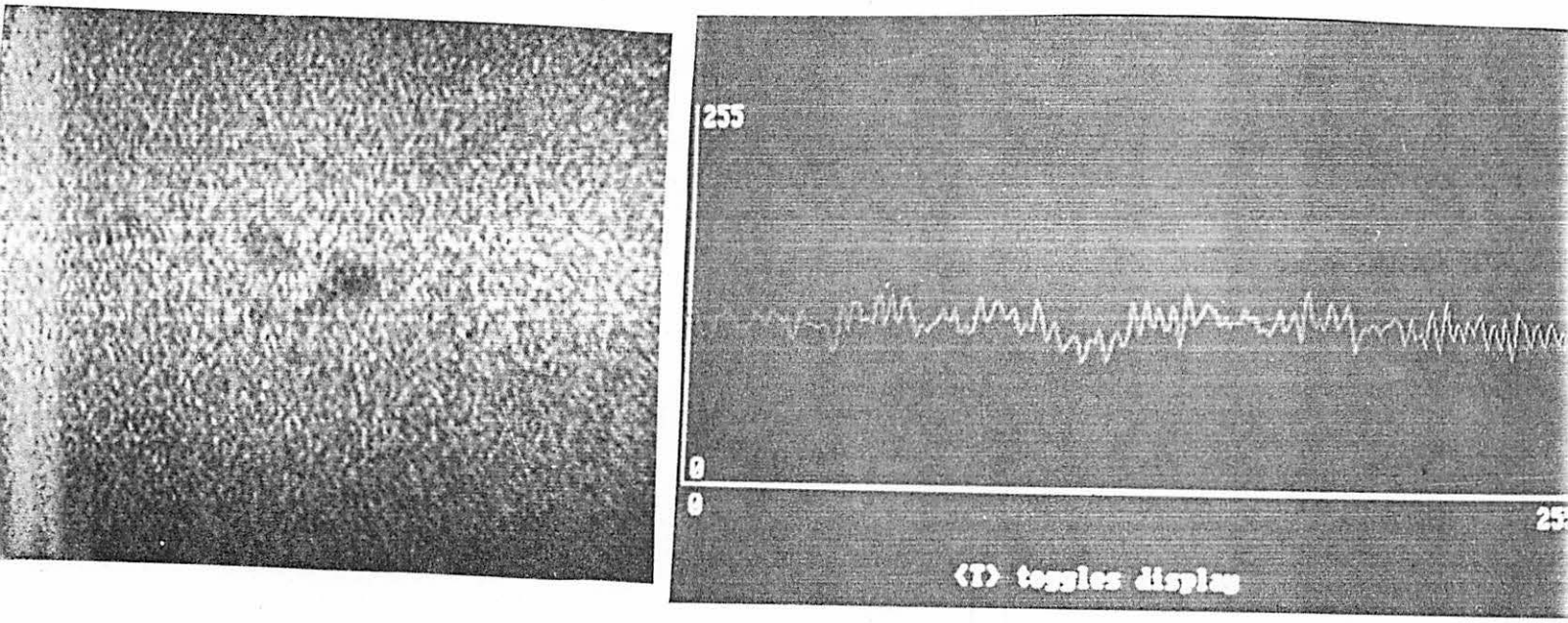

Figure 4.8: Digitized radiograph of a space shuttle fuel tank (Courtesy of Martin Marietta) and a slice through the image

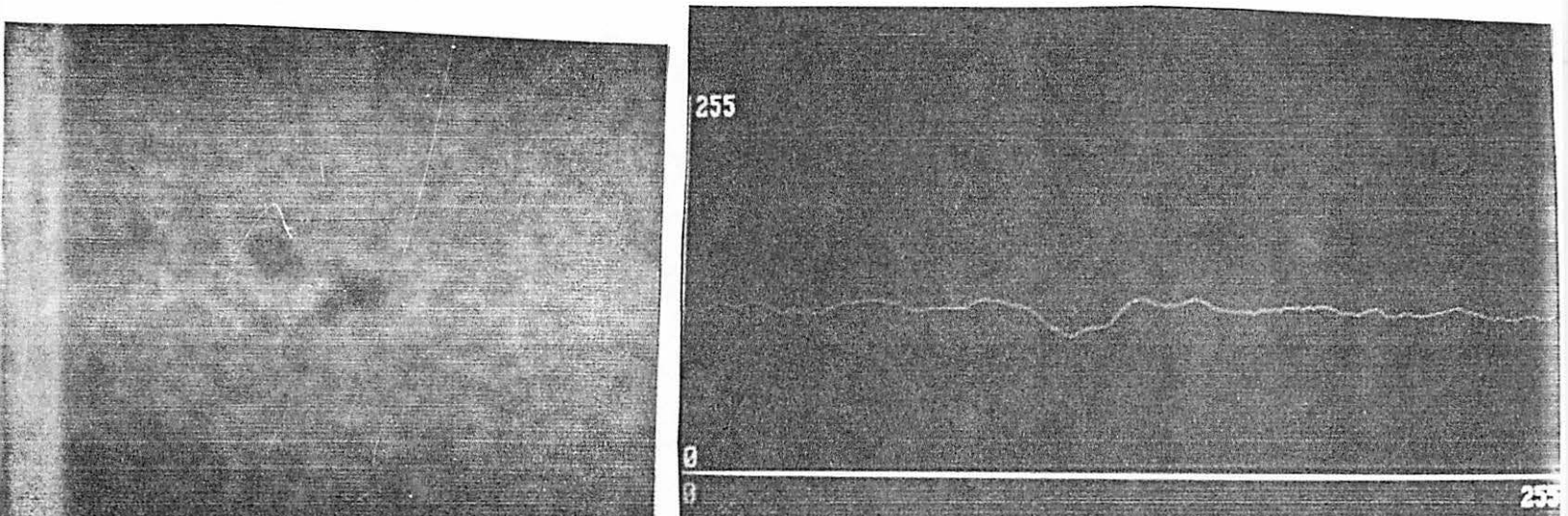

Figure 4.9: Hybrid filtered image and its slice

CHAPTER 5. APPLICATION OF MORPHOLOGICAL FILTERING TO NDE

Ever since the industrial revolution, the dependence of man on machine has grown rapidly. With the advent and growth of computers, we have come to the stage where people have more faith in computers than human judgement. To err is human, and so it does not come as a surprise when there is a strong move to replace humans with machines in jobs that are subject to lot of fatigue. X-ray technicians are one such class of people who face extinction. An x-ray technician goes through miles of radiographs looking for flaws. Even, if the flaws are easily visible, factors such as human fatigue and the monotony of the job, could adversely affect his judgement. So the drive to make the detection of flaws automated makes sense especially in the aircraft industry where there is no room for error. Automated detection of flaws is relatively simple in cases where the flaws can be separated from the background. This can be done when the histogram of the image is bi-modal. The background and the nonbackground intensities can be thresholded into distinct regions. The histograms of NDE x-ray images often tend to be uni-modal which prohibits thresholding. So the first hurdle to be crossed towards automated detection is suppressing the background.

Another approach to background elimination is to estimate the background intensity levels using some form of low pass filter (e.g., based upon a fast Fourier

transformation of the digitized image). Linear filter techniques (based upon transforms into the frequency domain) alter image information in ways that can conflict with the need for precise measurement of the size and location of flaws that are of utmost importance in our work. Non-linear filters such as opening and closing can suppress the background but still retain size and location information with a fair amount of accuracy. Morphological features alter the intensity values of images, but the geometric nature of morphological filters describes the manner in which the intensities are changed. Further, the extent to which the intensities are altered can be controlled based on the nature of the structuring element and will be a subject of discussion in this chapter. This chapter discusses, with illustrations, the practical applications of morphological filters. It also includes the report on a project we did for Westinghouse.

Background Elimination

Opening removes features brighter than the background but smaller than the structuring element from the image. Thus, if the features of interest are brighter than the background, opening the image by a structuring element bigger than the largest feature will remove the features from the image leaving behind an estimate of the background. Subtracting the estimate of the background from the original image extracts the flaws. The structuring elements most commonly used are the hemisphere and the cylinder. If the flaws are bright, then

$$\textit{Background estimate} = \mathbf{A} \circ \mathbf{B}. \tag{5.1}$$

$$\textit{Background reduction} = \mathbf{A} - (\mathbf{A} \circ \mathbf{B}) \tag{5.2}$$

where **B** is larger than any of the bright features of interest. The location of the extracted flaws will be exactly the same as in the original image. The size also agrees with the original size if the structuring element exceeds the flaw size. The background image may still contain some of the intensity information. Since opening removes all the bright features smaller than the structuring element, the extracted flaws may contain noise-like features smaller than the structuring element. In most cases, there will be an intensity disparity between the flaws and the noise-like regions permitting noise removal by thresholding. If this is not the case, the best approach will be to remove the noise-like features first by opening the image by a small structuring element (say 5×5) and then using this image to estimate the background. The trade-off is that some of the smaller flaws will be lost. One could always use some preprocessing to remove noise before opening. Once the flaws are extracted and thresholded, there are many routines for locating and sizing the flaws. Figure 5.1 is the digitized radiograph of a composite with bright dot-like flaws. The largest flaw is roughly 7×7 pixels in size. Figure 5.2 is obtained by opening this image with an 11×11 hemisphere and gives the background estimate of the picture in Figure 5.2. Subtracting the image in Figure 5.2 from the one in Figure 5.1 gives Figure 5.3 with the flaws extracted. There are noise-like features which can be easily removed by thresholding.

Closing removes features darker than the background but smaller than the structuring element from the image. Thus, if the features of interest are darker than the background, closing the image by a structuring element bigger than the largest feature will remove the features from the image leaving behind an estimate of the background. Subtracting the original image from the estimate of the background

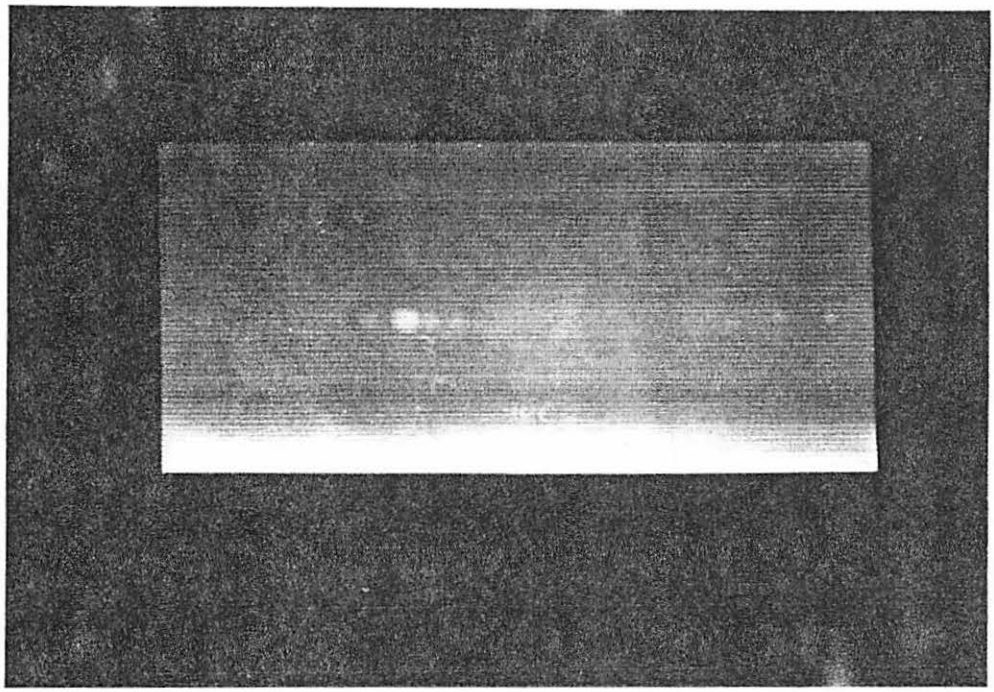

Figure 5.1: Digitized radiograph of a composite (Courtesy of Westinghouse)

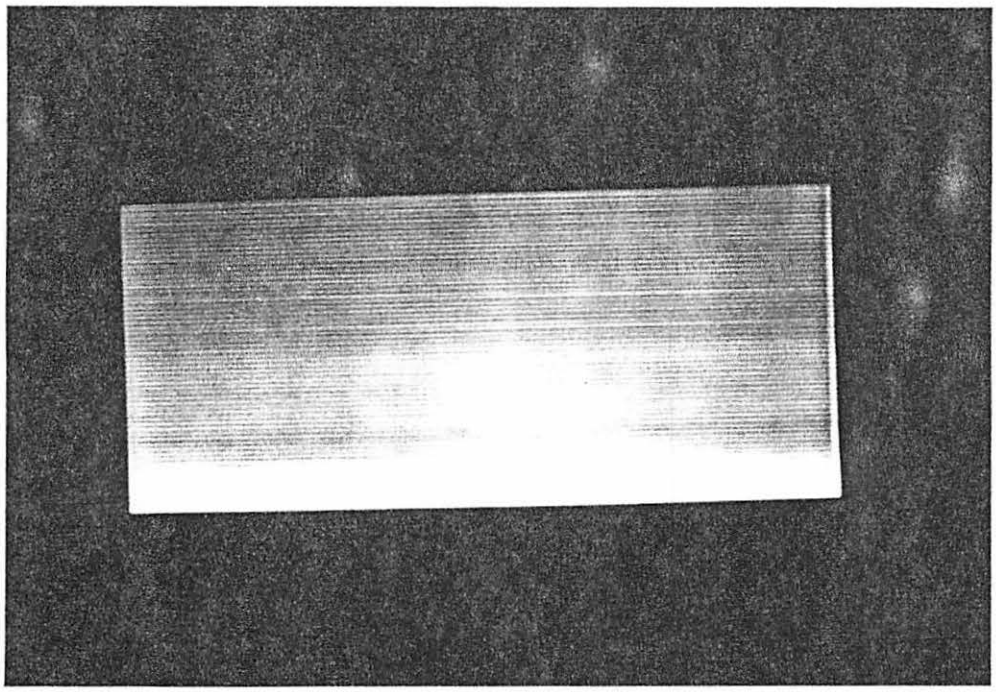

Figure 5.2: Background estimate obtained by opening

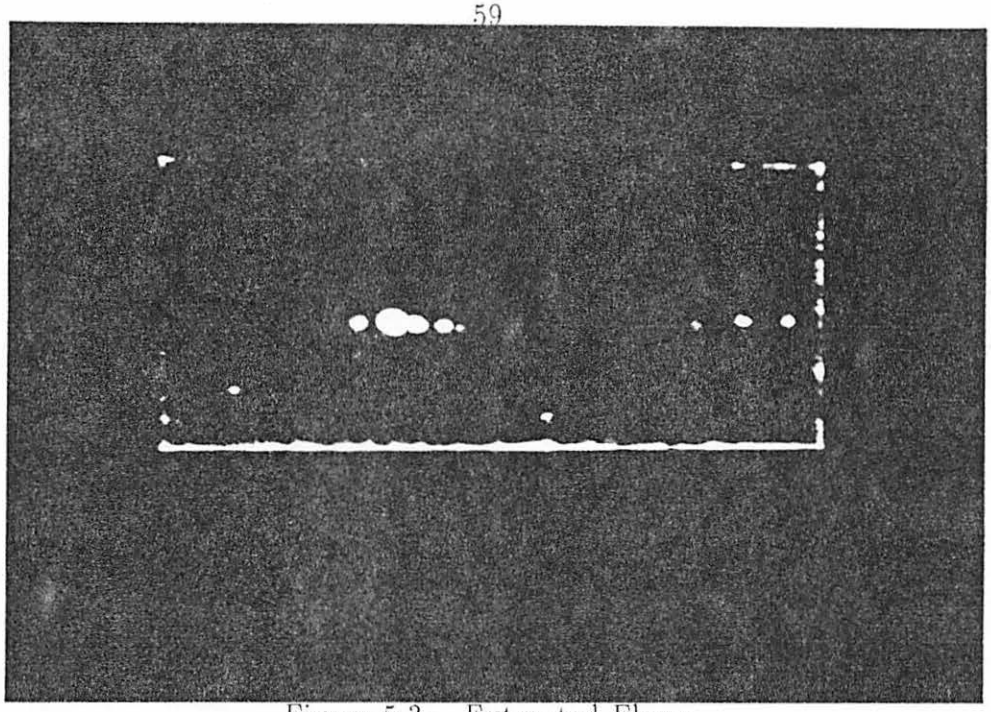

Figure 5.3: Extracted Flaws

extracts the flaws. If the flaws are dark, then

$$\textit{Background estimate} = \mathrm{A} \bullet \mathrm{B}. \tag{5.3}$$

$$\textit{Background reduction} = (\mathrm{A} \bullet \mathrm{B}) - \mathrm{A} \tag{5.4}$$

where B is larger than any of the dark features of interest. Figure 5.4 is an illustration of the power of morphology to extract flaws that are hidden in background trends. The picture on the left is the digitized radiograph of a control valve. There is a flaw hidden in the transition region from dark to bright. The flaw is hardly visible and the image conditions make it difficult for most image processing routines to detect it. This image was closed by a 13×13 cylinder to obtain the background estimate. The image was then subtracted from the background estimate to pull out the flaw as shown by the image at the center. The size and location of the flaw remains the same but the intensity information is inverted. The image on the right is a result of

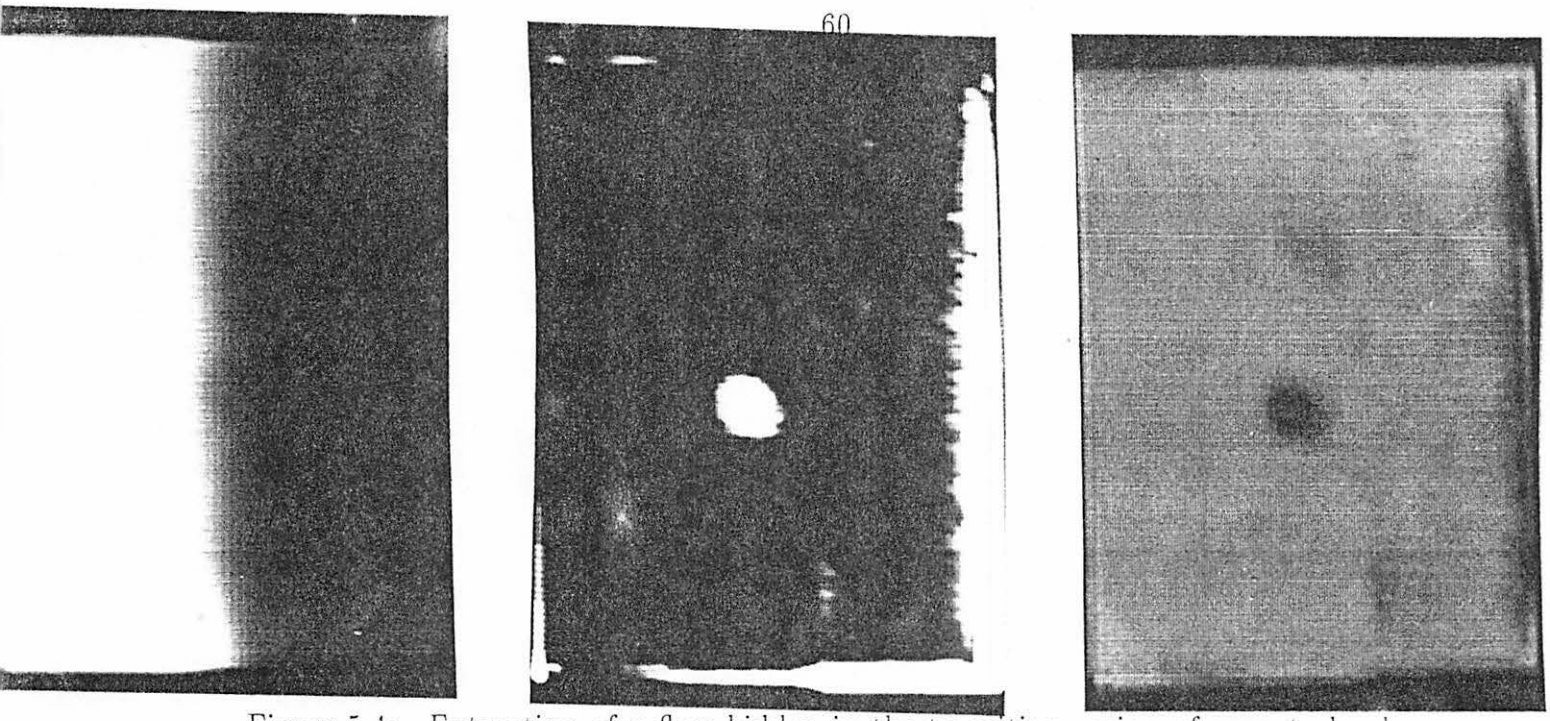

Figure 5.4: Extraction of a flaw hidden in the transition region of a control valve by closing

image enhancement which is discussed later in the chapter.

Selection of Structuring Element

A variety of structuring elements have been tried on NDE images. Hemispheres and cylinders were found to be the most useful. For the purpose of background estimation, a cylinder seems to be the ideal structuring element. Figure 5.5 compares the opening of a one- dimensional slice of A by a cylinder and a hemisphere of the same radius. The image opened by the cylinder is clearly a better estimate, as illustrated in Figure 5.5, because it minimizes the residue of the flaw in the result. The top of the hemisphere may fit up into a flaw, resulting in a background surface that will not truly measure the background level. When the background surface is subtracted from the original spot intensities the result will be a lowering of flaw

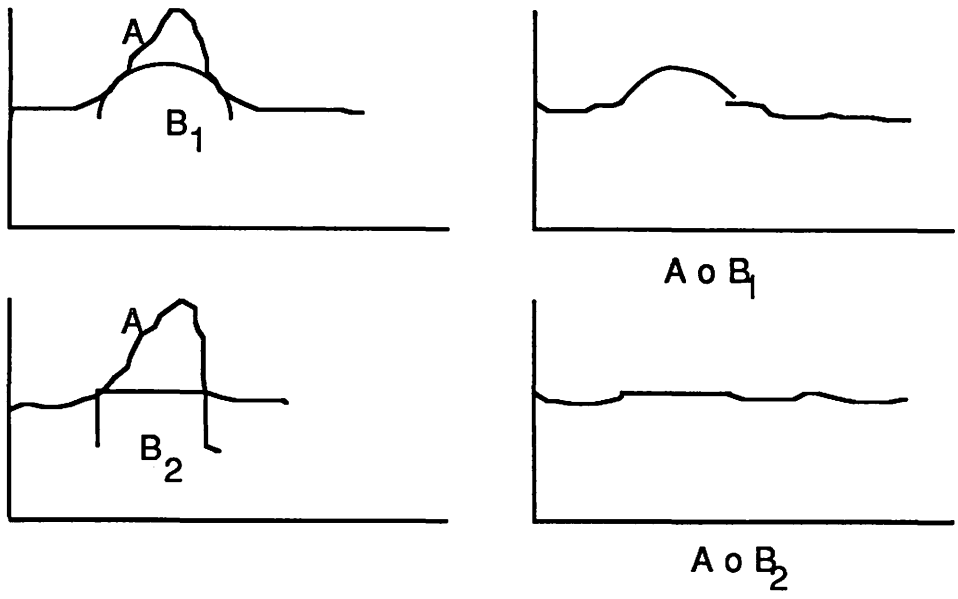

Figure 5.5: Comparing hemisphere with a cylinder in an opening operation

intensities near the flaw peak (decreasing in effect as the flaw borders are approached). As seen in the figure, this problem is alleviated to a great extent by using a cylinder. A hemisphere of a larger radius can be comparable to a cylinder, but it will increase the computational time considerably.

For filtering purposes, a hemisphere was found to be better than a cylinder. Owing to the abrupt edges, a cylinder clips off a lot of useful information, whereas a hemisphere with its rounded edges slides over or under the surface.

Elimination of Artifacts

Structuring elements have made morphological filtering so flexible that one can improvise fancy routines. Elimination of artifacts is a good example. Many radiographs have artifacts that are often misleading or distort information. Artifacts could also be a major obstacle in automating the detection of flaws. When these artifacts are in the form of lines, opening or closing by planes can eliminate them. Horizontal and vertical structuring elements, denoted by $\mathbf{H}$ and $\mathbf{V}$, respectively, are shown in Figure 5.6. If the artifacts are horizontal and bright, they can be eliminated by opening with a horizontal plane given by:

$$\textit{Reduction of horizontal artifact} = \mathbf{A} \circ \mathbf{H}. \tag{5.5}$$

If the artifacts are vertical, they can be eliminated by opening with a vertical plane and is given by:

$$\textit{Reduction of vertical artifact} = \mathbf{A} \circ \mathbf{V}. \tag{5.6}$$

The lengths of $\mathbf{H}$ and $\mathbf{V}$ should be less than the length of the artifacts. Diagonal structuring elements could be used for removing diagonal artifacts.

Figure 5.7 shows an x-ray image of a composite material with artifacts and the result of artifact elimination. The two bright horizontal streaks in the picture on the left are artifacts. It was possible to remove the artifacts totally from the image. This can be largely attributed to the fact that the artifacts were perfectly horizontal. The image was opened by a plane of length fifteen pixels to eliminate the artifacts. Eliminating the artifacts make the image a lot easier to work with.

$$H = [1\ 1\ 1 \cdots 1\ 1\ 1]_{1x(n+1)} \qquad V = \begin{vmatrix} 1 \\ 1 \\ 1 \\ \cdot \\ \cdot \\ \cdot \\ 1 \\ 1 \\ 1 \end{vmatrix}_{(n+1)X1}$$

Figure 5.6: A horizontal structuring element, H, is on the left and a vertical structuring element, V, is on the right

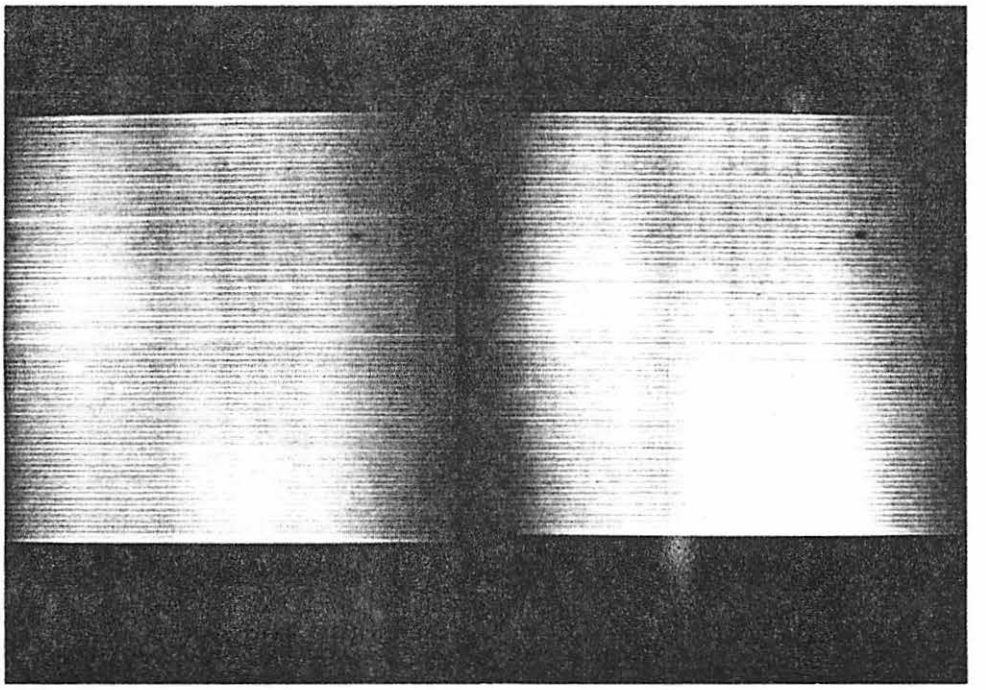

Figure 5.7: The picture on the left is the image of a composite with artifacts (Courtesy of Westinghouse). The image on the right is the result of artifact reduction

Detection of Cracks

The principle of elimination of artifacts can be extended to the detection of cracks. Closing the image with vertical or horizontal planes gives the background estimate. Subtracting the background from the original leaves the cracks behind. Figure 5.8 gives the digitized x-ray radiograph of a pipe and the result of crack detection. The image on the left has a faint horizontal flaw. The flaw is pulled out by closing with a plane of length 17 pixels and then superimposing the result on the original image. The detected flaw is composed of linear segments. This technique is useful for flaw detection and not for flaw characterization. It is very effective in pulling out faint crack-like flaws. It does not work well in noisy conditions. Morphological crack detection is very simple and computationally a lot faster than the Hough transform. But, it lacks the versatility of Hough transform.

Report to Westinghouse Electric Corporation on the Evaluation of Sample Radiographs

The objectives of the project were to try our existing image processing routines on the sample radiographs from Westinghouse and to check the acquisition capabilities of our image capture system. A variety of image processing routines were tried on these images. Owing to the faintness of the flaws and the low contrast of the images, morphological routines outperformed most of our other image processing software. All the figures are given at the end of the report.

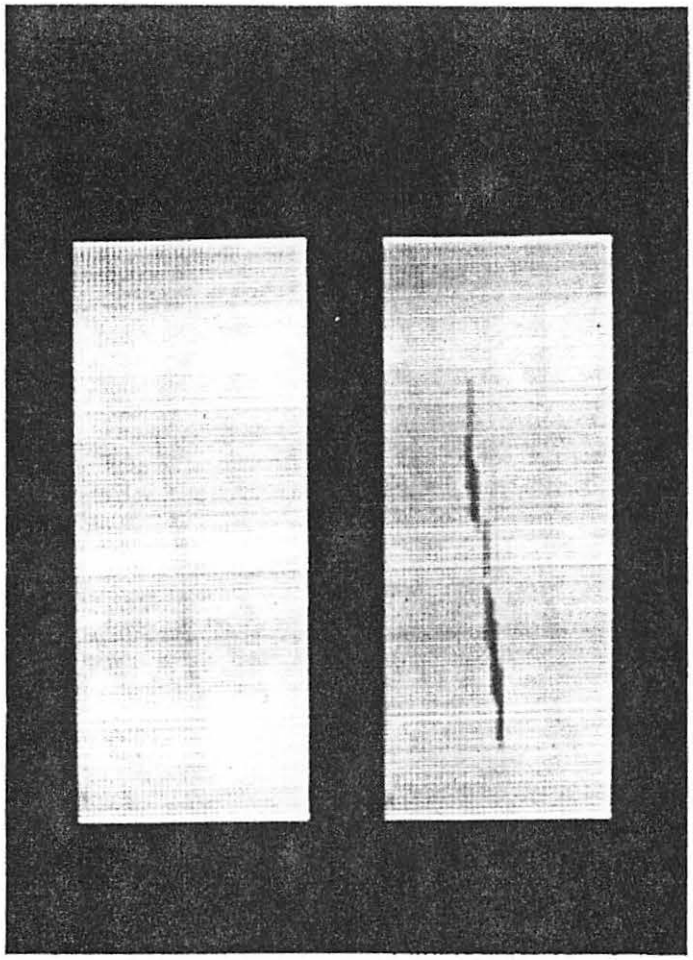

Figure 5.8: The picture on the left shows the digitized radiograph of a pipe (Courtesy of Westinghouse). The picture on the right gives the result of crack detection

Introduction

This document reports the results of our evaluation of two sample radiographs sent to us in December 1987 for processing and evaluating. Sample#1 shows a radiograph of the weldment, a contact print of the radiograph, and an enlargement of the weld zone from the contact print. The objective of our analysis was to compare the enhancement capabilities associated with the original radiograph, a contact print of the original radiograph, or an enlargement of the contact print. For Sample#2, the objective was to compare the single-wall radiograph with multiple-shot double-wall work. Westinghouse was also interested in finding out whether our acquisition system is capable of displaying the image together with the flaws.

The region of interest marked on the radiographs was divided into three sections and each of these sections was separately digitized. With the lens available to us, we could not focus on the entire region of interest. This report does not include the processing results of every section, but only a few of the relavent ones. All the pictures are gray scale images.

Processing Techniques and Results

Figure 5.9 shows the digitized region of interest on the single wall shot radiograph of the laser-welded sleeve (Sample#1). The digitized image was lowpass filtered to reduce the noise. The filtered image was processed morphologically to remove the background and extract the flaws. The morphological steps were as following. The image was closed by a 13×13 hemispherical structuring element. Morphological closing removed the flaws from the original image leaving behind an estimate of the background of the image. Subtracting the estimate of the background from the

original image extracted the flaws. Figure 5.10 shows the result of morphological enhancement. Note that, in Figure 5.10, most of the background trend has been removed bringing out the porosity.

To compare the enhancement capabilities associated with the radiograph, the contact print, and the enlargement of the contact print, we used one of our standard image processing macros. It involves first order trend removal along the columns, followed by histogram equalization. The trend removal is accomplished by fitting a first order polynomial to the columns of the image and subtracting the function from the actual data.

Figure 5.11 shows the digitized region of interest on the radiograph. Figure 5.12 is the trend removed image and Figure 5.13 is the histogram equalized image. Figure 5.14 shows shows the digitized region of interest on the contact print. Figure 5.15 is the trend removed image and Figure 5.16, the histogram equalized. Figure 5.17 shows the digitized region of interest on the enlargement of the weld zone from the contact print. Figure 5.18 and Figure 5.19 are the trend removed and histogram equalized, respectively. Comparing Figure 5.13, Figure 5.16 and Figure 5.19, it is obvious that the enlargement of the contact print has the best enhancement capabilities followed by the original radiograph. Very little information can be obtained from the contact print of the radiograph.

Figure 5.20 is a small section of the single-wall radiograph of Sample#2. Figure 5.21 is the result of a morphological routine that detects cracks. Figure 5.22 is a subsection of Figure 5.20. Figure 5.23 is the result of the morphological crack detection routine. Figure 5.20 and Figure 5.22 show that it is possible to capture the faint flaws on the radiograph. Figure 5.24 is a section of the double-wall shot

(Sample #2). Notice how noisy the image is. Figure 5.25 is the result of processing Figure 5.24 using the crack detection routine.

Conclusions

For Sample#1, based on the experimenting we have done, we have no doubt that the enlarged contact print has the best enhancement capabilities. It tends to be slightly noisier than its competitors, but filtering can take care of this problem. The single-wall shot radiograph also brings out most of the porosity. The contact print is not much help.

Sample#2 has been a real challenge to our group. We had to get new lenses to digitize the radiographs. The flaws are very faint and narrow, and with all the inherent limitations of our camera we were able to do a good job of digitizing the radiographs. As the flaws were very thin and faint, we had to magnify the image, resulting in a rather noisy image. Most our routines were very sensitive to noise. Due to the faintness of the flaws, filtering invariably removed the desired information. We finally decided to try some morphological processing. Morphological filtering can pull out the flaws, but in addition pulls out a lot of noisy features. So, we had to improvise the morphological routines to detect cracks. This appeared to work pretty effectively on the Sample #2 radiographs.

From the enhancement point of view, we have every little doubt that single-wall shots are better than double-wall shots. The single wall-shots are less noisier than the double-wall shots and further the cracks seem to appear sharper on the single-wall shot radiograph. We felt that the single-wall shot contained more information than the double-wall shot. Further, the double-wall shot radiographs seem to give more

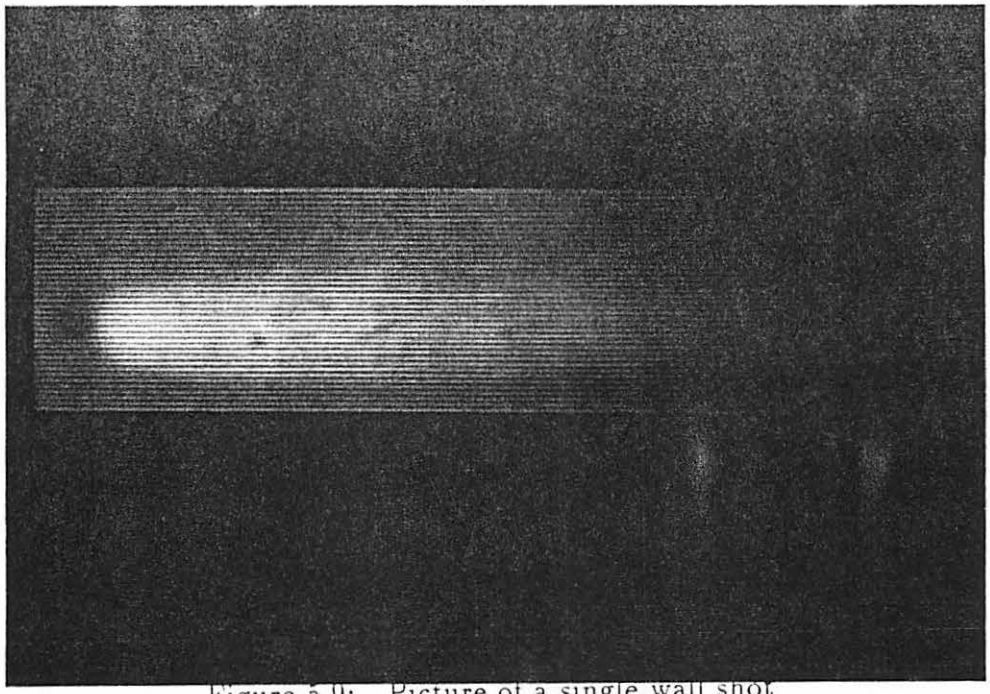

Figure 5.9: Picture of a single wall shot

false alarms than single-wall shot radiographs.

We were successful in digitizing the radiographs together with the flaws. With a reasonably good camera and the right lenses, the radiographs can be displayed on a monitor with good resolution. This could save lot of trouble for the technicians who have to go over miles of radiographs with hand lenses.

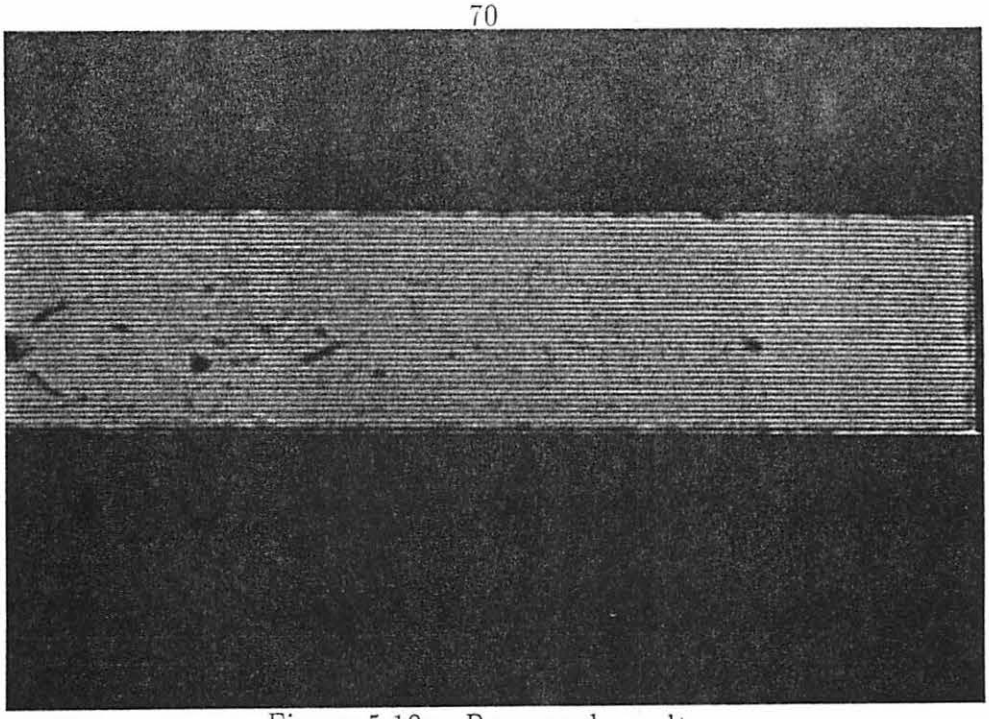

Figure 5.10: Processed result.

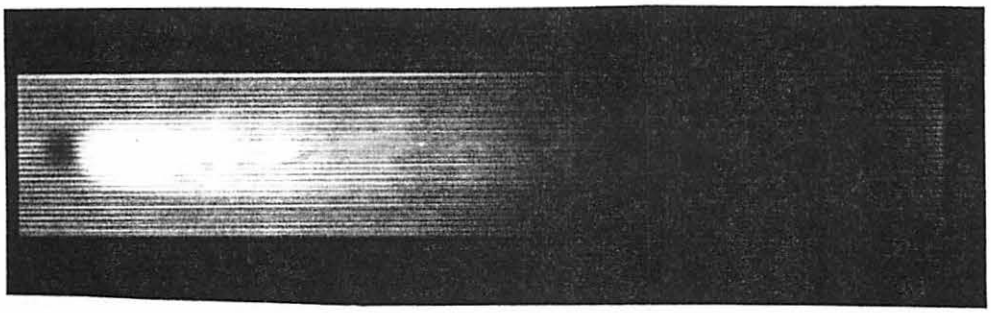

Figure 5.11: Picture of a single wall shot

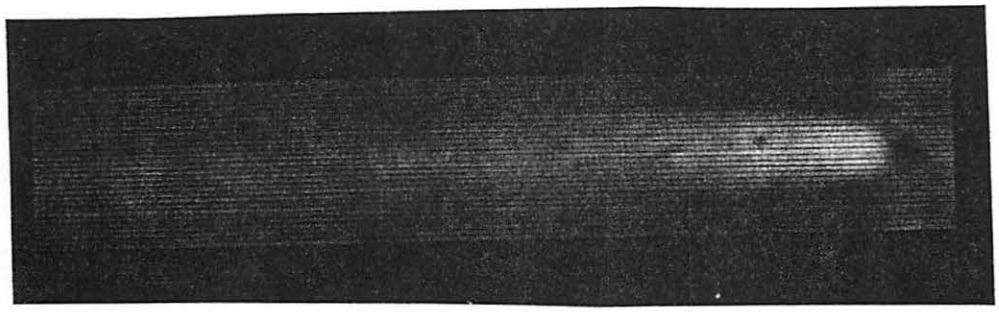

Figure 5.12: Result of trend removal

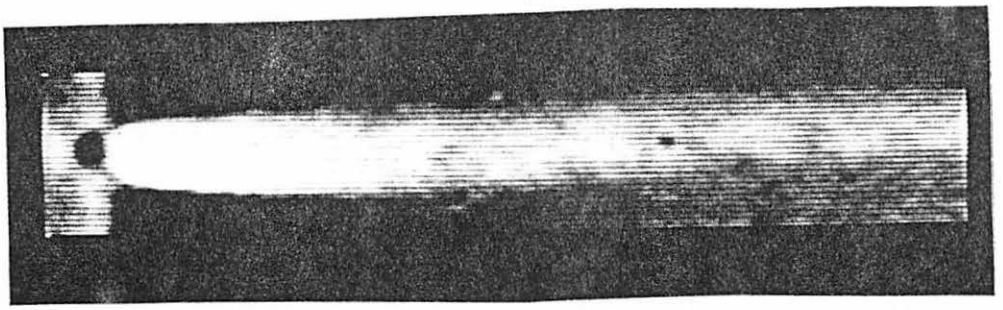

Figure 5.13: Result of histogram equalization

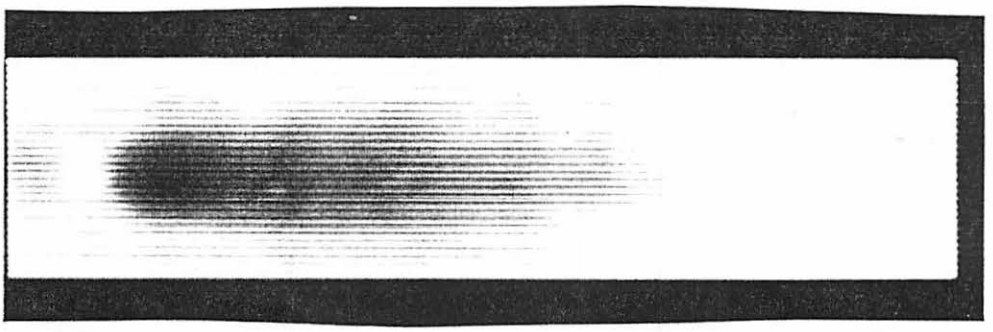

Figure 5.14: Picture of contact print

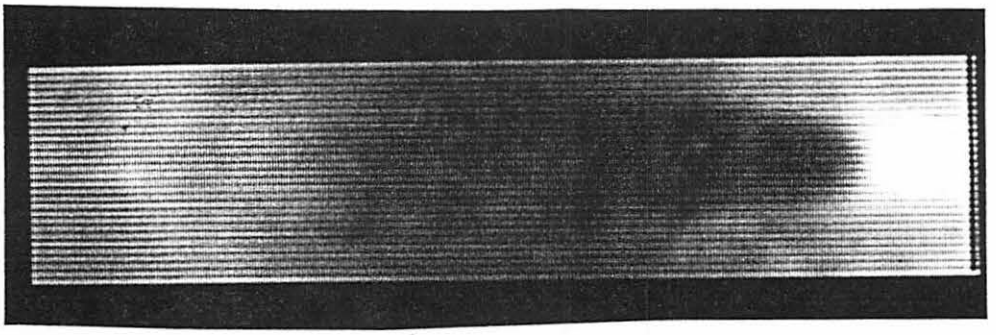

Figure 5.15: Result of trend removal

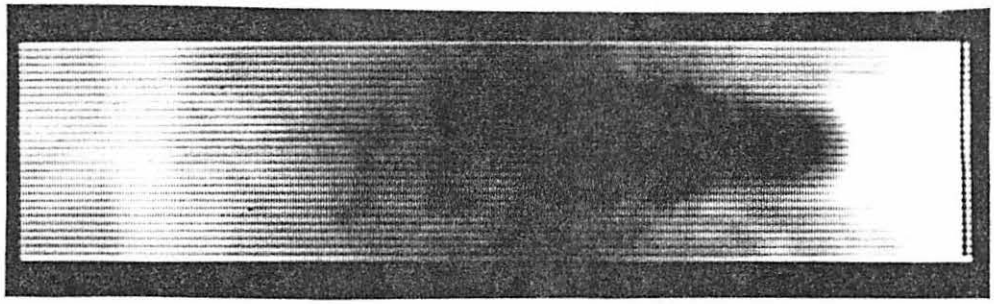

Figure 5.16: Histogram equalized image

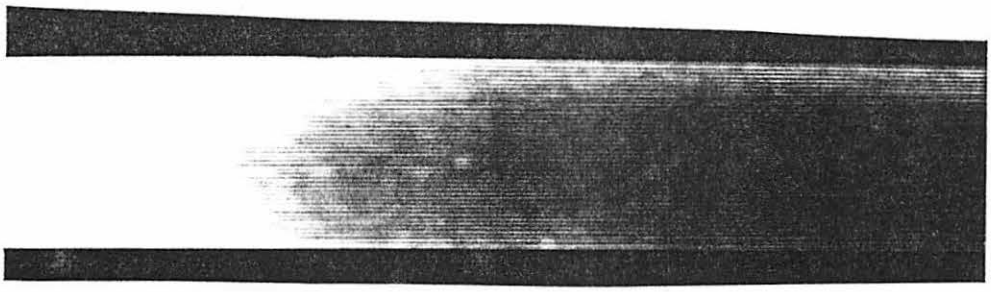

Figure 5.17: Picture of enlargement of contact print

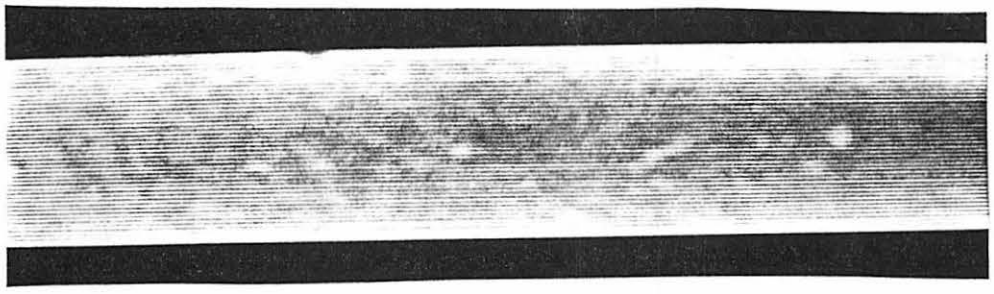

Figure 5.18: Result of trend removal

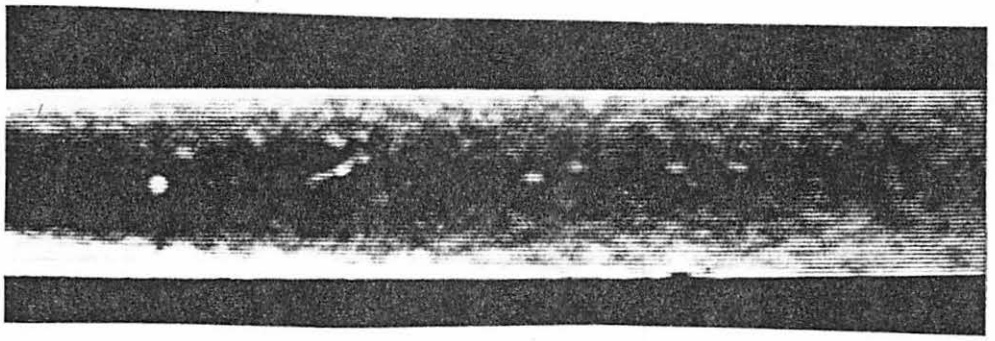

Figure 5.19: Result of histogram equalization

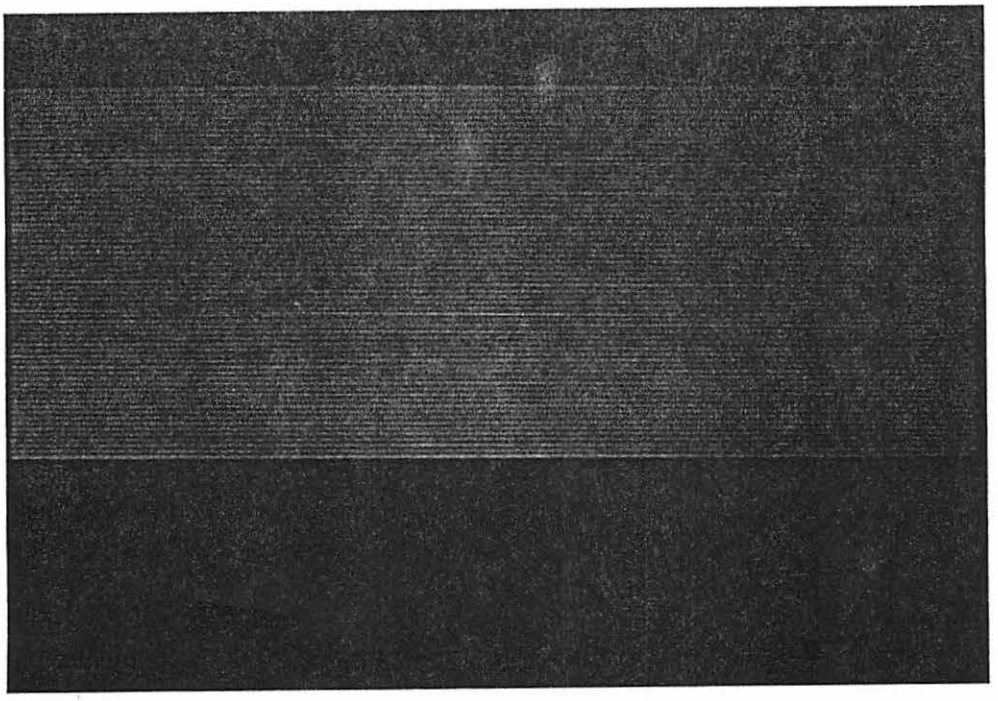

Figure 5.20: Picture of a small section of single wall x-ray of sample#2

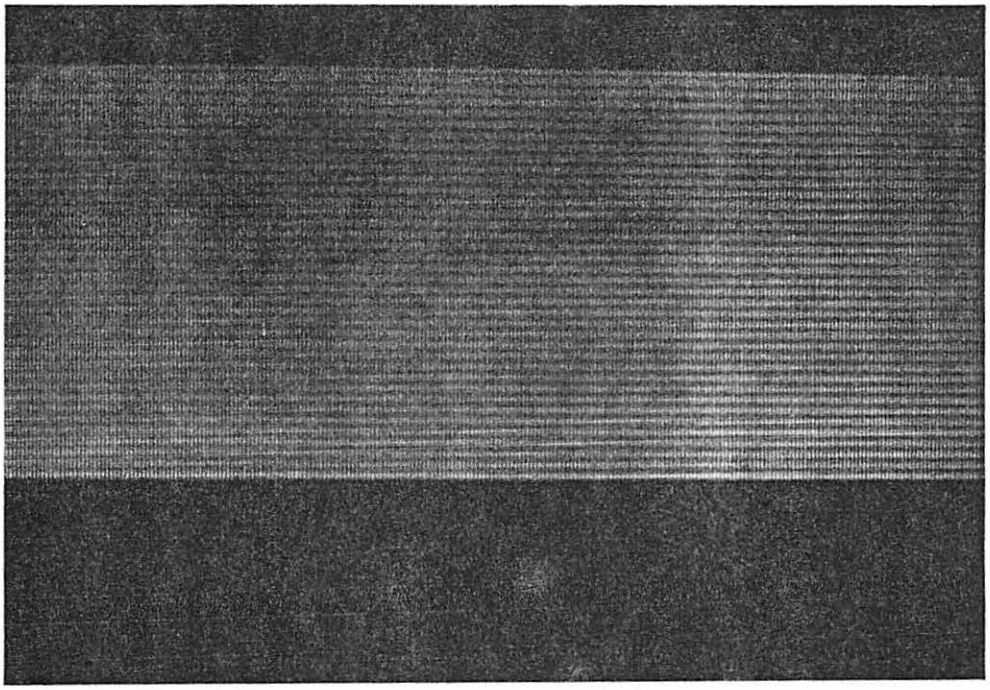

Figure 5.21: Picture of subsection of Figure 5.20

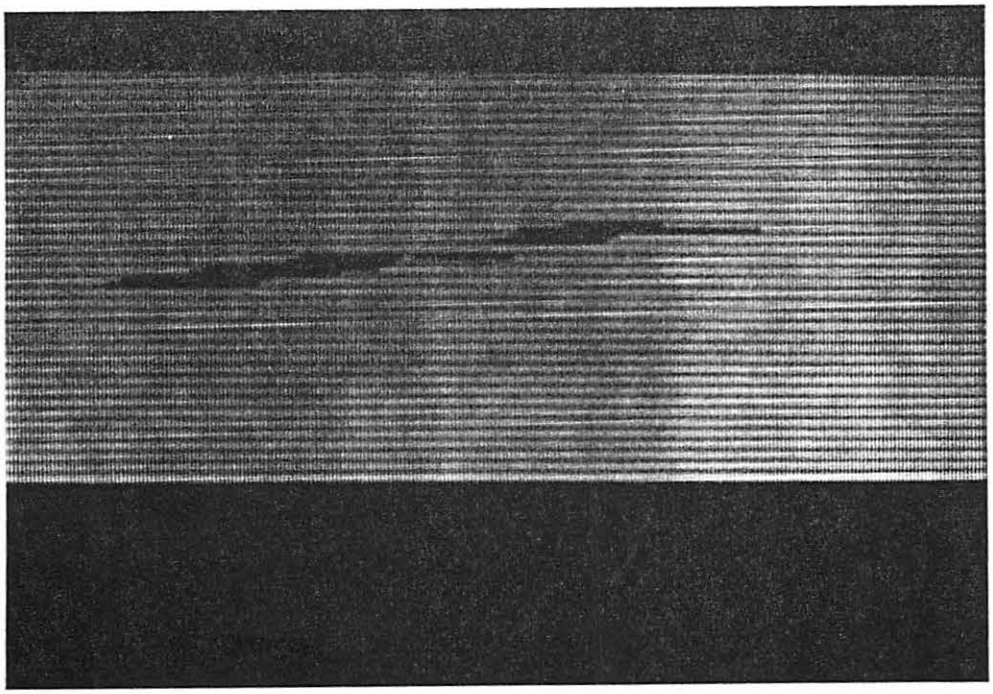

Figure 5.22: Result of morphological processing

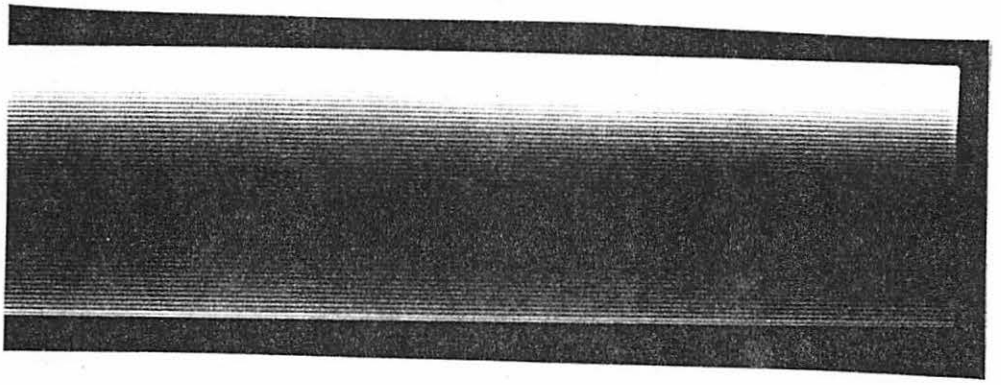

Figure 5.23: Picture of a section of double wall shot

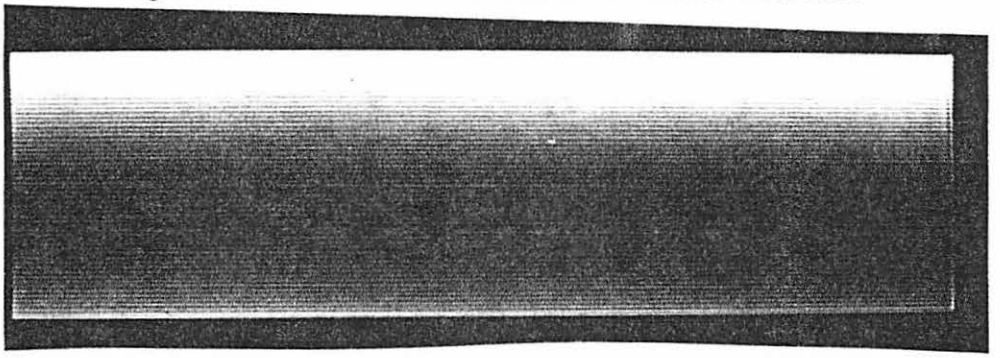

Figure 5.24: Result of morphological processing

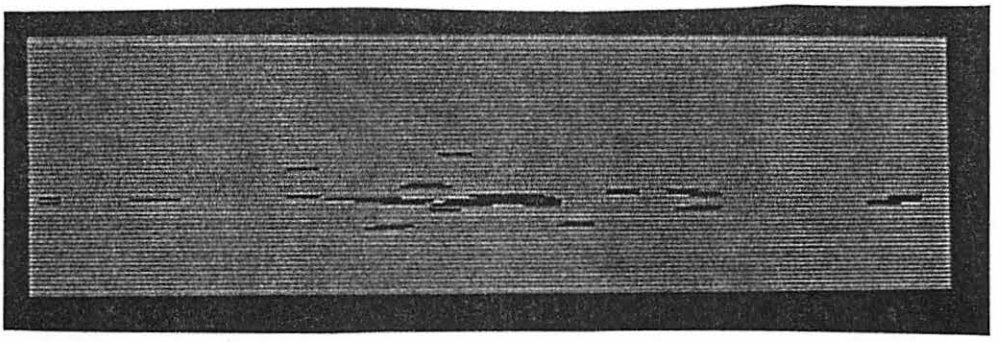

Figure 5.25: Binary image of Figure 5.24

CHAPTER 6. MORPHOLOGICAL EDGE DETECTION

Edges are probably the most reliable descriptors of the shape of an object. For this reason edge detectors are commonly used in object recognition. Basically, the idea underlying most edge detection techniques is the computation of a local derivative operator. Such detectors are called gradient operators. Gradient operators are sensitive to noise and often tend to magnify it. The NDE images we work with often tend to be noisy. This imposes severe constraints on using gradient operators. Though morphological edge detectors are simple, their performance is comparable to that of sophisticated edge focussing techniques in noisy conditions. The morphological routines are relatively insensitive to noise. Further, morphological edge detection routines are comparable in speed to a 3×3 convolution operation. Morphological edge detectors are very rarely mentioned in the literature. They have been of great help in our work and it deserve more than a kind word. Four different morphological edge detectors are discussed in this chapter.

Morphological Gradient

Serra (1982) and Meyer (1986) define the gradient in terms of morphological operators as:

$$Gradient1 = (\mathbf{A} \oplus \mathbf{B}) - (\mathbf{A} \ominus \mathbf{B}) \tag{6.1}$$

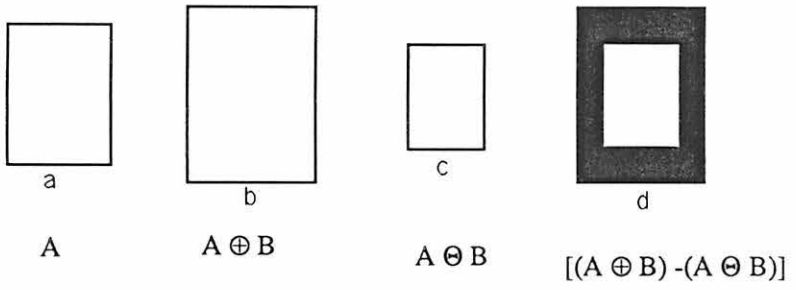

Figure 6.1: Illustration of Gradient1

where **B** is a 3×3 cylinder. Figure 6.1 illustrates this principle. As shown by the figure, the boundary is two pixels thick and might appear out of focus.

From our experience, we found that a sharper boundary can be obtained by defining the gradient as:

$$Gradient2 = (\mathbf{A} \oplus \mathbf{B}) - \mathbf{A} = \mathbf{A} - (\mathbf{A} \ominus \mathbf{B}) \tag{6.2}$$

Figure 6.2 illustrates this definition. The concept is very easy to understand. Dilating an image by a 3×3 cylinder causes the brighter regions to get thicker along their boundaries by a pixel. Thus subtracting the original image from the dilated image pulls out the external growth of the boundaries, which is one pixel wide. An NDE application of this edge detector is shown in Figure 6.3. The picture on the left is the digitized radiograph of a honeycomb structure. The picture on the right is obtained by using Gradient2 on the original. The objective of applying edge detection to the

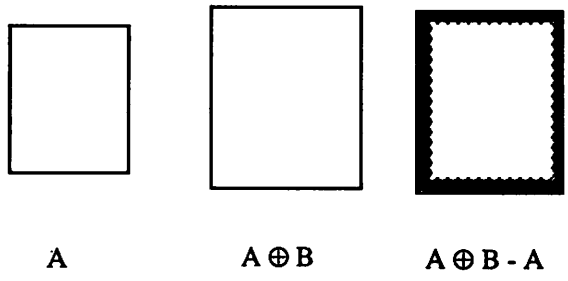

Figure 6.2: Illustration of Gradient2

honeycomb was to detect the signature of crushed core, which appears as a halo around the hexagonal structure of the honeycomb. The arrow in the picture on the left points to a region of interest. The image, as one can observe, is fairly noiseless. In the resulting image, the signature of crushed core appears as lines parallel to, but very close to, the hexagonal edges. Gradient2 is comparable in performance, as well as computational time, to the Laplacian and other gradient operators. Gradient1 and Gradient2 are sensitive to noise but unlike conventional edge detectors do not magnify noise.

A third morphological edge detector, introduced by Lee et al. (1986), that is to a great extent noise insensitive is defined by:

$$Gradient3 \;=\; min\,\{[(\mathbf{A}\oplus\mathbf{B})-\mathbf{A}],[\mathbf{A}-(\mathbf{A}\ominus\mathbf{B})]\}. \tag{6.3}$$

where the min operator indicates the minimum of the two operators at each pixel. The results of this operator on ideal ramp edges are great. It is insensitive to isolated noise points. Unfortunately, it is not able to detect ideal step edges. This is the motivation for the blur minimum morphological edge detector improvised by Lee et al. (1986). In this edge detector, the image is first blurred that converts the ideal

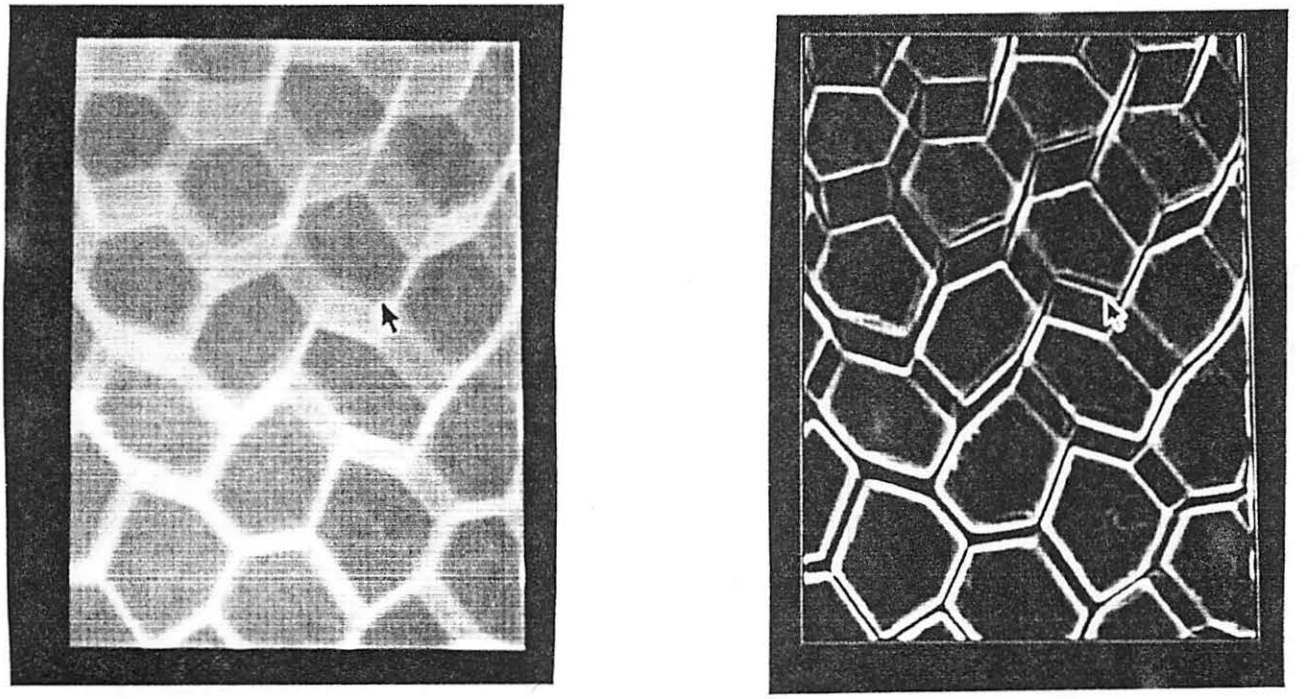

Figure 6.3: The picture on the left is the digitized radiograph of a honeycomb (Courtesy of Joe Gray). The one on the right is the edge detected image

step edges into ideal ramp edges, and then Gradient3 is applied to the blurred image.

Blur Minimum Morphologic Edge Operator

As stated above, the image has to be blurred before applying the Gradient3 operator. One thing to be noted is that the domain of the blurring mask should be the same as the domain of **B** used for dilation and erosion. The domain of a 3×3 cylinder is $\{(0,1),(-1,1),(0,0),(1,1),(0,-1)\}$ and will be the domain of the blurring mask. Given an image **A**, its blurred version, **I** is given by :

$$\mathbf{I}(i,j) = \{\mathbf{I}(i-1,j) + \mathbf{I}(i,j) + \mathbf{I}(i+1,j) + \mathbf{I}(i,j+1) + \mathbf{I}(i,j-1)\}/5. \qquad (6.4)$$

where I(i,j) is the gray scale value at (i,j). Given the blurred image **I**, the modified gradient edge detector is defined by:

$$Gradient4 \;=\; min\;\{[(\mathbf{I} \oplus \mathbf{B}) - \mathbf{I}], [\mathbf{I} - (\mathbf{I} \ominus \mathbf{B})]\}. \qquad (6.5)$$

Due to the blurring operation, we lose some of the edge strength. Thus, if the image is not noisy to start with, it is better to use Gradient3. It is a trade-off between higher signal-to-noise ratio and sharper edges when we choose between Gradient4 and Gradient3.

Gradient4 has been fairly successful in detecting edges in noisy images. It does a better job than any of the edge detection routines available to the NDE group at Iowa State University. Figure 6.4 is a real-time x-ray image of a honeycomb structure with a magnification of 6 times. Real-time x-ray images are much noisier than images digitized from radiographs. Figure 6.5 is the result of applying Sobel operator to Figure 6.4. Figure 6.6 shows the result of applying Gradient4. As in the case of

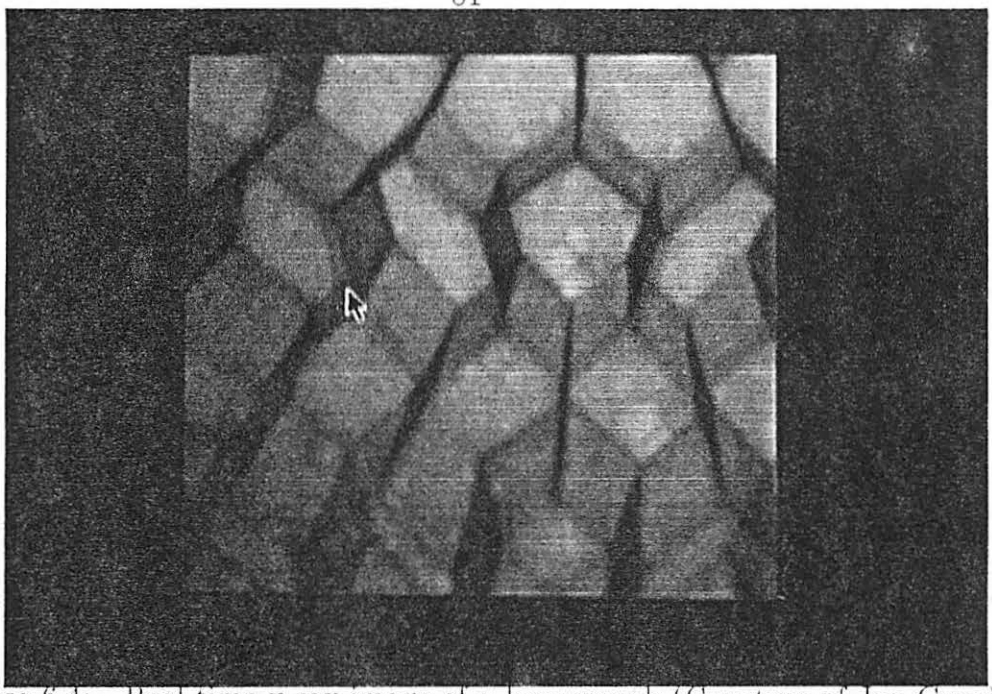

Figure 6.4: Real time x-ray image of a honeycomb (Courtesy of Joe Gray)

Figure 6.3, the objective is to detect the crushed core which appears as lines par allel to the edges of the hexagonal pattern. The Sobel operator is successful in detecting the signature of the crushed core, but as can be seen in Figure 6.5 the image is too noisy. The Gradient4 detects the edges but maintains the noise level much lower then that in Figure 6.5.

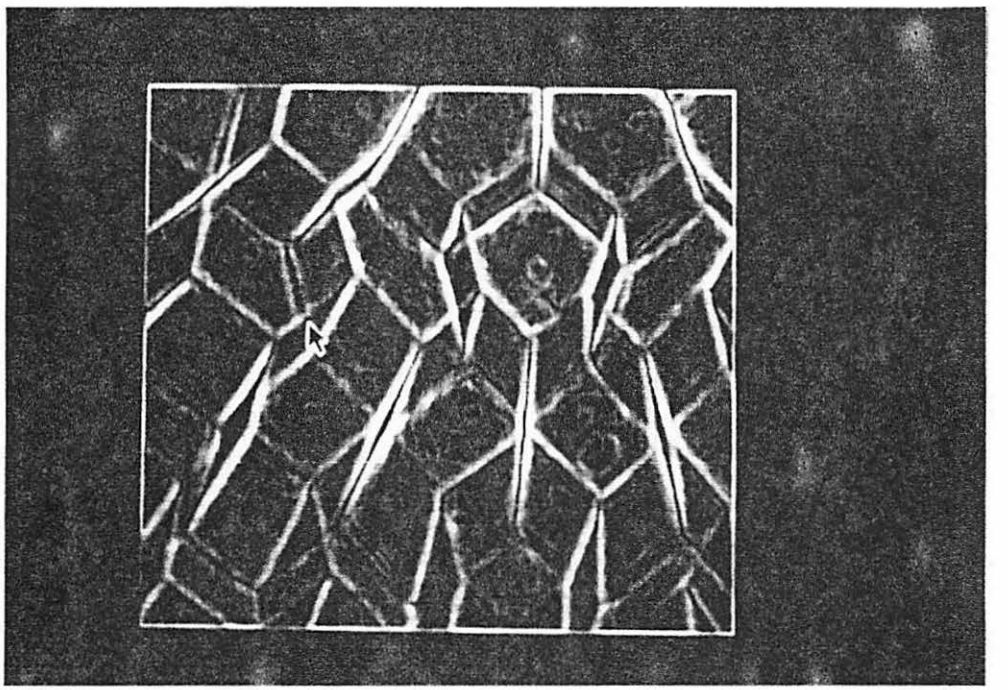

Figure 6.5: Edge detected using Sobel operator

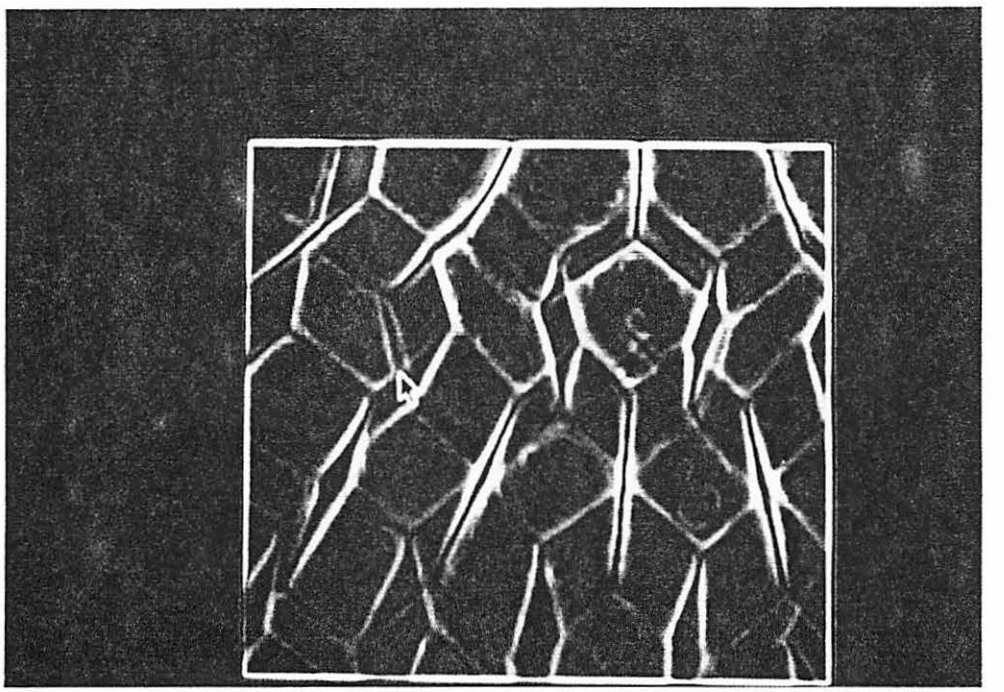

Figure 6.6: Edge detected using Gradient4

CHAPTER 7. CONNECTIVITY

There is no limit to man's curiosity or his eagerness to learn. With the discovery of x-rays by Roentgen in 1895, it became possible to unveil many of the mysteries of the human physiology. Further, x-rays became one of the major tools in nondestructive evaluation of materials. X-rays are projections of three-dimensional objects onto a two-dimensional film. Hence, information such as depth and volume still remained very much elusive. Such information is critical in the medical field when it comes to sizing and locating tumors and clots. Though not so critical, sizing and locating the flaws helps to determine whether a manufactured part is beyond repair. A lot of research is currently going on in the three-dimensional reconstruction of flaws in materials using tomography, reconstruction from limited angle projections, and so on. There are cases where the depth of the flaws are not as important as the size. Flaws at different depths in the material might appear as one connected cluster in the film plane. This happens often in the case of railway frogs. The principles of connectivity could be used to a certain extent in separating these flaws. Often the frogs are rejected based on the sizing of the individual flaws. If the size of a certain flaw exceeds a critical size, the frog may have to be rejected. Thus, it becomes necessary to separate the connected flaws. Another application of connectivity to NDE is discussed in the following chapter. This chapter discusses an algorithm that

distinguishes particles that overlap in the image plane. It also discusses some morphological tools such as conditional dilation, hit or miss transform, ultimate erosion, thinning and thicken ing. Serra's book (1982) discusses all these operations is detail. All the images that are being dealt in this chapter are binary.

Definitions

Conditional Dilation: The conditional dilation of $\mathbf{A}$ by $\mathbf{B}$ with respect to $\mathbf{X}$ is denoted by $\mathbf{A} \oplus \mathbf{B}; \mathbf{X}$ and is defined by:

$$\mathbf{A} \oplus \mathbf{B}; \mathbf{X} = (\mathbf{A} \oplus \mathbf{B}) \cap \mathbf{X}. \tag{7.1}$$

Here $\mathbf{A}$ is dilated by $\mathbf{B}$ and all those regions common to the limiting set $\mathbf{X}$ are retained.

Repeated Conditional Dilation: The repeated conditional dilation of $\mathbf{A}$ by $\mathbf{B}$ is denoted by $\mathbf{A} \oplus \{\mathbf{B}\}; \mathbf{X}$ and is defined by:

$$\mathbf{A} \oplus \{\mathbf{B}\}; \mathbf{X} = \cdots[[[(\mathbf{A} \oplus \mathbf{B}) \cap \mathbf{X}] \oplus \mathbf{B}] \cap \mathbf{X}] \oplus \mathbf{B} \cdots. \tag{7.2}$$

Here $\mathbf{A}$ is repeatedly dilated by $\mathbf{B}$ until no further growth is observed in the set consisting of elements common to the limiting set $\mathbf{X}$ and the set obtained by repeated dilations. This sequential algorithm is of great importance as it relates to the connectivity of $\mathbf{X}$.

Hit or Miss Transform: For an input image $\mathbf{X}$, the hit-or-miss transform is denoted by $\mathbf{X} \otimes \mathbf{T}$ and is defined by:

$$\mathbf{X} \otimes \mathbf{T} = [(\mathbf{X} \ominus \mathbf{T}_1) \cap (\mathbf{X}^c \ominus \mathbf{T}_2)]. \tag{7.3}$$

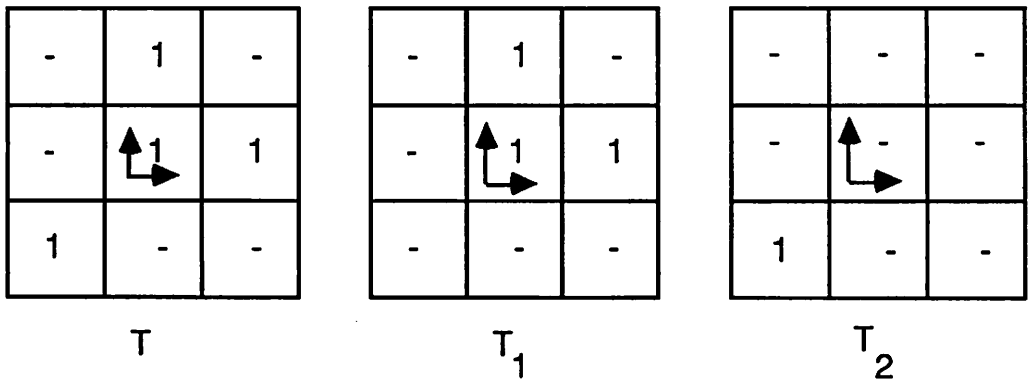

Figure 7.1: Structuring element used in hit-or-miss transform

where the structuring element $\mathbf{T}$ is a union of $\mathbf{T}_1$ and $\mathbf{T}_2$. $\mathbf{T}_1$ and $\mathbf{T}_2$ are disjoint sets. The origin should belong to either one of $\mathbf{T}_1$ and $\mathbf{T}_2$ and not to both. The hit-or-miss transform studies the relation between the image and its complement with respect to the structuring element by probing the image and its complement with structuring elements. $\mathbf{X} \ominus \mathbf{T}_1$ hits $\mathbf{X}$ and $\mathbf{X}^c \ominus \mathbf{T}_2$ misses $\mathbf{X}$ and hence the name hit-or-miss transform. Two sets are disjoint if they have no elements in common. Normally $\mathbf{T}$ is a 3×3 mask as shown in Figure 7.1.

Ultimate Erosion: The ultimate erosions of $\mathbf{X}$ consists of the set of all seeds of the connected components of $\mathbf{X}$. Each connected component of $\mathbf{X}$ generates an ultimate erosion or a seed. Connected components are particles that appear overlapped on the image. A seed is the stage in the successive erosions of a particle before the particle disappears. Let $\mathbf{X}_i = \mathbf{X} \ominus i\mathbf{B}$, where $\mathbf{B}$ is a unit circle and $i\mathbf{B}$ is a circle of radius i units. Then the ultimate erosion $\mathbf{Y}_i$ is defined to be the components of $\mathbf{X}_i$ which

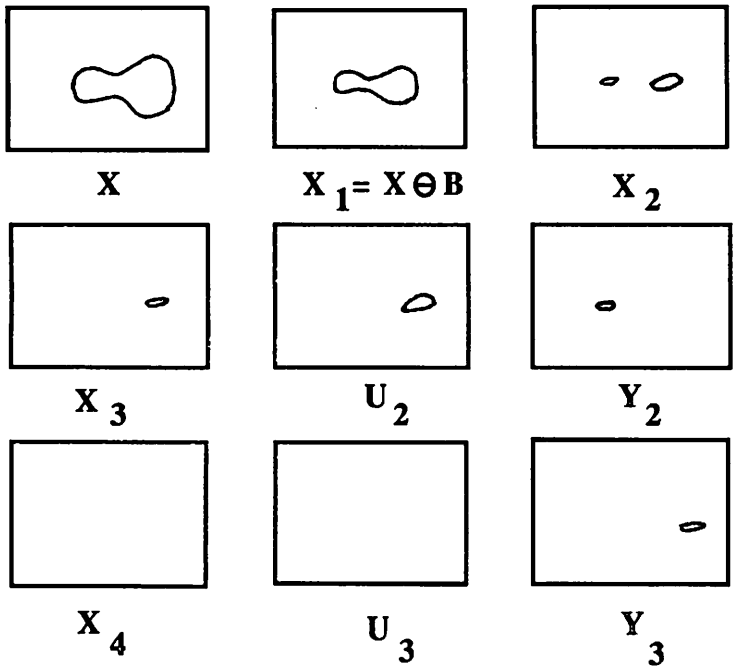

Figure 7.2: Illustration of ultimate erosion

vanish from any larger erosion $\mathbf{X}_j$ (j greater than i), and is given by:

$$\mathbf{U}_i = (\mathbf{X}_{i+1} \oplus \{B\}); \mathbf{X}_i \tag{7.4}$$

$$\mathbf{Y}_i = \mathbf{X}_i - \mathbf{U}_i \tag{7.5}$$

The ultimate eroded sets of $\mathbf{X}$ are obtained by taking the union of all $\mathbf{Y}_i$s. Figure 7.2 shows a set $\mathbf{X}$ consisting of two connected particles. $\mathbf{X}_i$s are obtained by successive erosion with $\mathbf{B}$. $\mathbf{Y}_1$ and $\mathbf{Y}_2$ are the ultimate eroded sets.

Thinning and Thickening

Thinning: Thinning as the name suggests is a skeletonizing operation. By definition, we thin $\mathbf{X}$ by $\mathbf{T}$ when we subtract the hit-or-miss transform of $\mathbf{X}$ from $\mathbf{X}$. Thinning is denoted by $\mathbf{X} \bigcirc \mathbf{T}$ and is given by:

$$\mathbf{X} \bigcirc \mathbf{T} = \mathbf{X} - \mathbf{X} \otimes \mathbf{T}. \tag{7.6}$$

Here $\mathbf{T} = \mathbf{T}_1 \cup \mathbf{T}_2$ and $\mathbf{T}_1$ and $\mathbf{T}_2$ are disjoint sets. In particular the origin cannot belong to both $\mathbf{T}_1$ and $\mathbf{T}_2$.

Sequential Thinning: Consider a sequence $\{\mathbf{T}^i\}$ of structuring elements. The thinning of $\mathbf{X}$ by the sequence $\{\mathbf{T}^i\}$ is defined by:

$$\mathbf{X} \bigcirc \{\mathbf{T}^i\} = (\cdots((\mathbf{X} \bigcirc \mathbf{T}^1) \bigcirc \mathbf{T}^2) \cdots \bigcirc \mathbf{T}^i \cdots). \tag{7.7}$$

Note that each $\mathbf{T}_i$ is an union of 2 disjoint sets. Each $\mathbf{T}^i$ consists of an union of two disjoint sets. The skeleton $\mathbf{S}$ of $\mathbf{X}$ is defined in terms of thinning by:

$$\mathbf{S} = \mathbf{X} \bigcirc \{\mathbf{T}^i\} \textit{ such that } \mathbf{S} \neq \emptyset. \tag{7.8}$$

Here $\mathbf{X}$ is repeatedly thinned by the same structuring element. The stage before $\mathbf{X}$ ceases to exist is the skeleton of $\mathbf{X}$.

Thickening: Thickening is the dual operation of thinning. The thickening of $\mathbf{X}$ by $\mathbf{T}$ is denoted by $\mathbf{X} \odot \mathbf{T}$ and is defined by:

$$\mathbf{X} \odot \mathbf{T} = \mathbf{X} \cup (\mathbf{X} \otimes \mathbf{T}). \tag{7.9}$$

Conditional Thickening: Exactly as with the conditional dilation, we can thicken $\mathbf{Y}$ within a limiting set $\mathbf{X}$. This operation is called conditional thickening of $\mathbf{Y}$ with

respect to $\mathbf{X}$ and is denoted by:

$$\mathbf{Y} \odot \mathbf{T}; \mathbf{X} = (\mathbf{Y} \odot \mathbf{T}) \cap \mathbf{X}. \tag{7.10}$$

Equipped with all these tools we are ready to implement the cluster fast segmentation developed by Meyer (1979).

Cluster Fast Segmentation (CFS)

This algorithm particles that overlap. The particels are assumed to be approximately convex. It is made up of two distinct phases, namely: to find markers for the zones to be separated, and to draw the boundaries. Here the markers are the ultimate eroded sets $\mathbf{Y}_i$. The steps involved in CFS are as given. $\mathbf{X}$ is the set to be split up.

Step 1:

$$\mathbf{X}_i = \mathbf{X} \ominus iB, for\ i = 1, \cdots, m\ where\ \{m : \mathbf{X}_m \neq \emptyset\}. \tag{7.11}$$

Here B is a unit circle, $\mathbf{X}_1 = \mathbf{X} \ominus B$, $\mathbf{X}_2 = \mathbf{X} \ominus 2B$, and so until $\mathbf{X}_m = \mathbf{X} \ominus mB$, and $\mathbf{X}_{m+1} = \emptyset$. $\mathbf{X}$ is given on the left in Figure 7.3. The boundary after each erosion is given by dotted lines in the figure on the right. Notice that after the second erosion $\mathbf{X}$ splits into two and after the fifth erosion $\mathbf{X}$ becomes a null set.

Step 2 (Ultimate Erosion):

$$\mathbf{Y}_i = \mathbf{X}_i / (\mathbf{X}_i + 1 \oplus \{H\}; \mathbf{X}_i). \tag{7.12}$$

Here the $\mathbf{Y}_i$s are the ultimate eroded sets or the seeds. Figure 7.4 illustrates Step 2. The ultimate erosions are $\mathbf{Y}_2$ and $\mathbf{Y}_4$. This is because $\mathbf{Y}_2$ and $\mathbf{Y}_4$ cease to exist after the third and fifth erosions respectively.

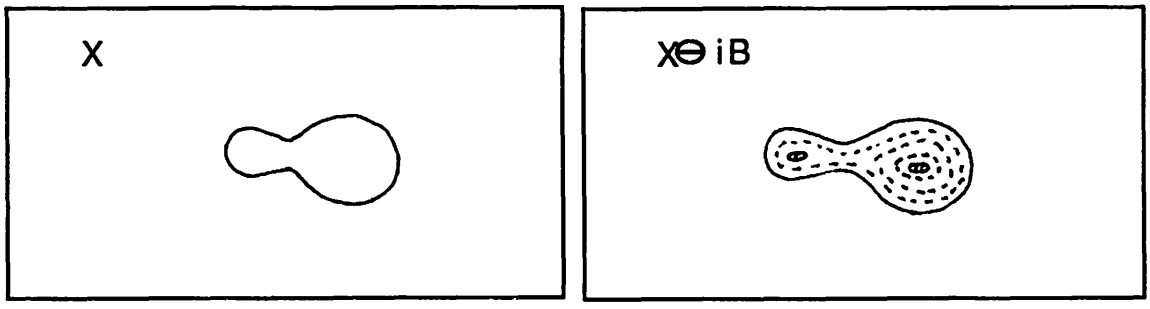

Figure 7.3: Illustration of Step 1 of CFS

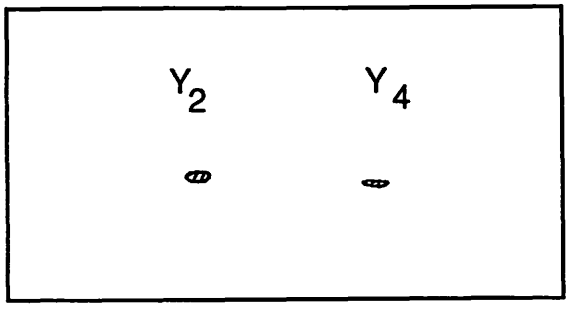

Figure 7.4: Illustration of Step 2

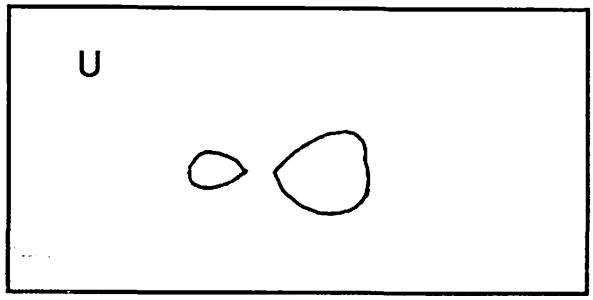

Figure 7.5: Illustration of Step 3

Step 3:

$$\mathbf{U} = \cup \mathbf{Y}_i \oplus (i-1)H; \ for\ i = 0\ to\ m. \tag{7.13}$$

Here we dilate each ultimate eroded set proportional to the size of the corresponding component. Step 3 is illustrated in Figure 7.5. It required 3 dilations and thickenings to obtain **U**, which is the final result.

Figure 7.6 is a simulated x-ray image of two ellipsoidal flaws at different depths in an aluminum block. The picture on the left in Figure 7.7 shows the ultimate eroded sets and the picture on the right gives the result of CFS. One thing to be noted is that for CFS to work the flaws have to be nearly convex. Further, there has to be a constriction at the region connecting the the flaws. If these conditions are satisfied CFS works for clusters with any number of connected flaws. In CFS, it is practically impossible to restore the flaws back to original size. In the result in Figure 7.7, the area of the restored flaws are seventy five percent of the original size.

Figure 7.6: Simulated x-ray image of two flaws at different depths in the material

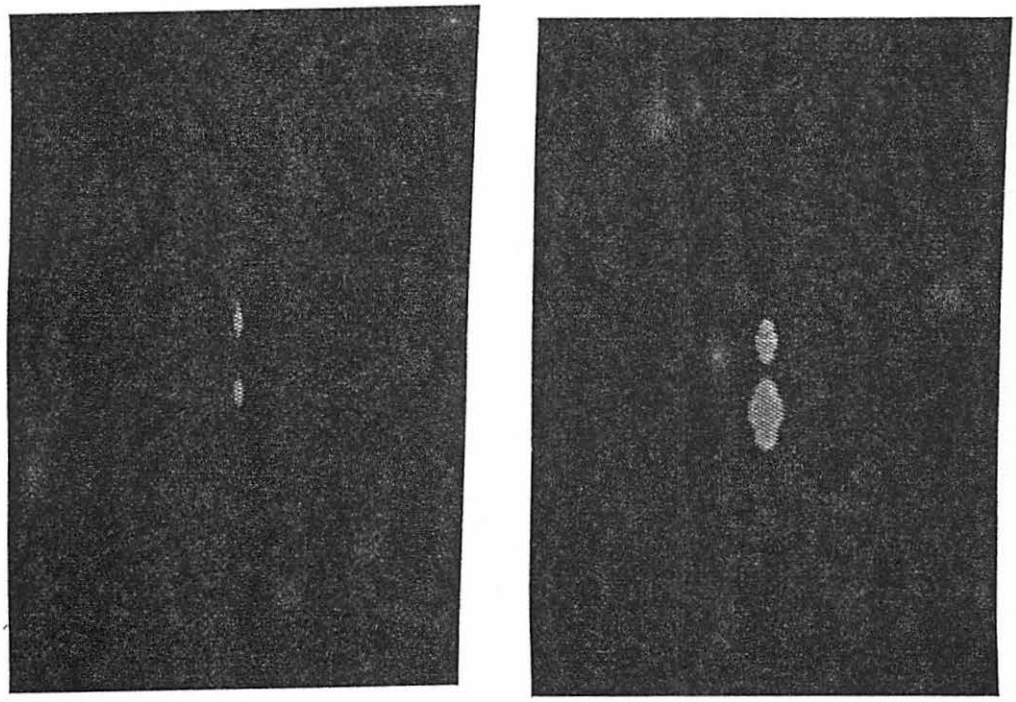

Figure 7.7: The picture on the left gives the two seeds and the one on the right gives the separated flaws

CHAPTER 8. APPLICATION OF MATHEMATICAL MORPHOLOGY TO THE STUDY OF MICROSTRUCTURAL CHARACTERISTICS OF METAL MATRIX COMPOSITES

In the process of manufacturing silicon carbide reinforced aluminum metal matrix composites, silicon carbide particles are mixed with aluminum powder and subjected to an extrusion process. The orientation of the silicon carbide particles in the resulting composite should be random for the stiffness of the material to be the same in the three orthogonal directions. Secondary electron images show that the orientation of the particles follow some pattern rather than being random. To determine stiffness, it becomes necessary to study nondestructively the microstructure characteristics such as the distribution of size, orientation, length and aspect ratio of the silicon carbide particles. In secondary electron images, it was found that many of the silicon carbide particles appear connected as shown in Figure 8.1. These particles have to be separated to obtain a good estimate of the stiffness. Cluster fast segmentation is not a reliable algorithm. A new algorithm has been developed that incorporates CFS and certain properties of the skeleton that make it possible to separate connected particles. At this stage this algorithm separates just one cluster of connected particles within an image. It can be easily extended to any number of clusters.

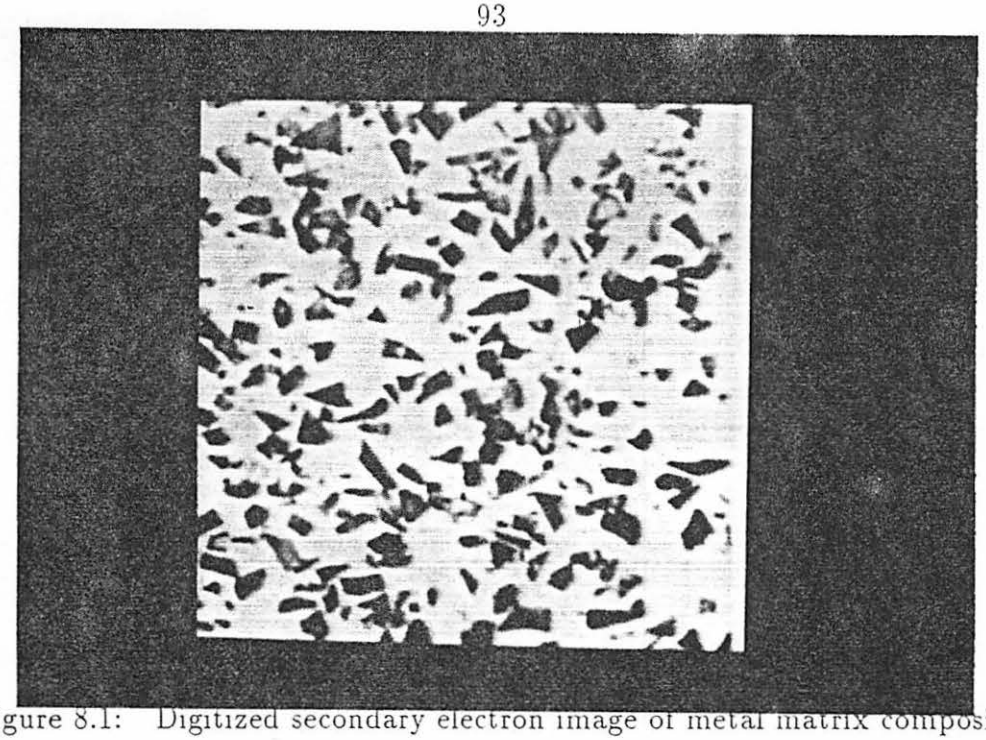

Figure 8.1: Digitized secondary electron image of metal matrix composite

Morphological Skeleton

The skeleton of a continuos object A is defined as the centers of the maximal disks inscribable inside A. A disk is maximal if it is not properly contained in any other disk totally included in A. Hence, a maximal disk must touch the boundary of A at least at two different points. A lot of work has been done on morphological skeletons. Lantuejoul (1980) defined the morphological skeleton for a continuos object. Serra (1982) provided an algorithm for the morphological skeleton of a discrete binary object. Maragos and Schafer (1986) use decomposed skeletons for coding of binary images.

The algorithm developed by Serra for obtaining the skeleton of a binary image is as given:

$$Let\ \mathrm{A}_0 = \mathrm{A}\ and\ i = 0.$$

$$do\ until\ \mathbf{B}_i = 0$$

$$\mathbf{A}_{i+1} = \mathbf{A}_i \ominus \mathbf{T}$$

$$\mathbf{B}_{i+1} = \mathbf{A}_{i+1} - (\mathbf{A}_{i+1} \circ \mathbf{T}) \tag{8.1}$$

$$i = i + 1$$

$$enddo.$$

$$\mathbf{B} = \sum_{k=1}^{i-1} \mathbf{B}_k. \tag{8.2}$$

Figure 8.2 illustrates the above algorithm. $\mathbf{T}$ is a unit circle of radius one, $\mathbf{A}$ the image to be skeletonized, and $\mathbf{B}$ the morphological skeleton. The first skeletal subset $\mathbf{B}_1$ is obtained by eroding $\mathbf{A}$ by $\mathbf{T}$, and then keeping from every eroded set $(\mathbf{A} \ominus \mathbf{T})$ only those parts which consist of angular points and lines without thickness. These parts are the only ones remaining after the set difference between $(\mathbf{A} \ominus \mathbf{T})$ and its opening $(\mathbf{A}_1 \circ \mathbf{T})$. $\mathbf{B}_2$ is obtained in a similar manner. $\mathbf{O}_1$ and $\mathbf{O}_2$ are obtained by opening $\mathbf{A}_1$ and $\mathbf{B}_1$ respectively by $\mathbf{T}$. In or example, $\mathbf{B}_3$ is a null set and so the skeleton, $\mathbf{B}$, is the union of $\mathbf{B}_1$ and $\mathbf{B}_2$.

Generalized Connectivity Algorithm

Step 1: The ultimate erosions (seeds) of the image are obtained using cluster fast segmentation. As mentioned earlier, based on the nature of connectivity, CFS may be able to break the connectivity. Figure 8.3 shows a simulated image of the metal matrix composite. Figure 8.4 gives the seeds generated by CFS. Every isolated component in Figure 8.3 has a corresponding seed. By comparing Figure 8.4 with Figure 8.3, we see that CFS was able to distinguish between some of the connected particles.

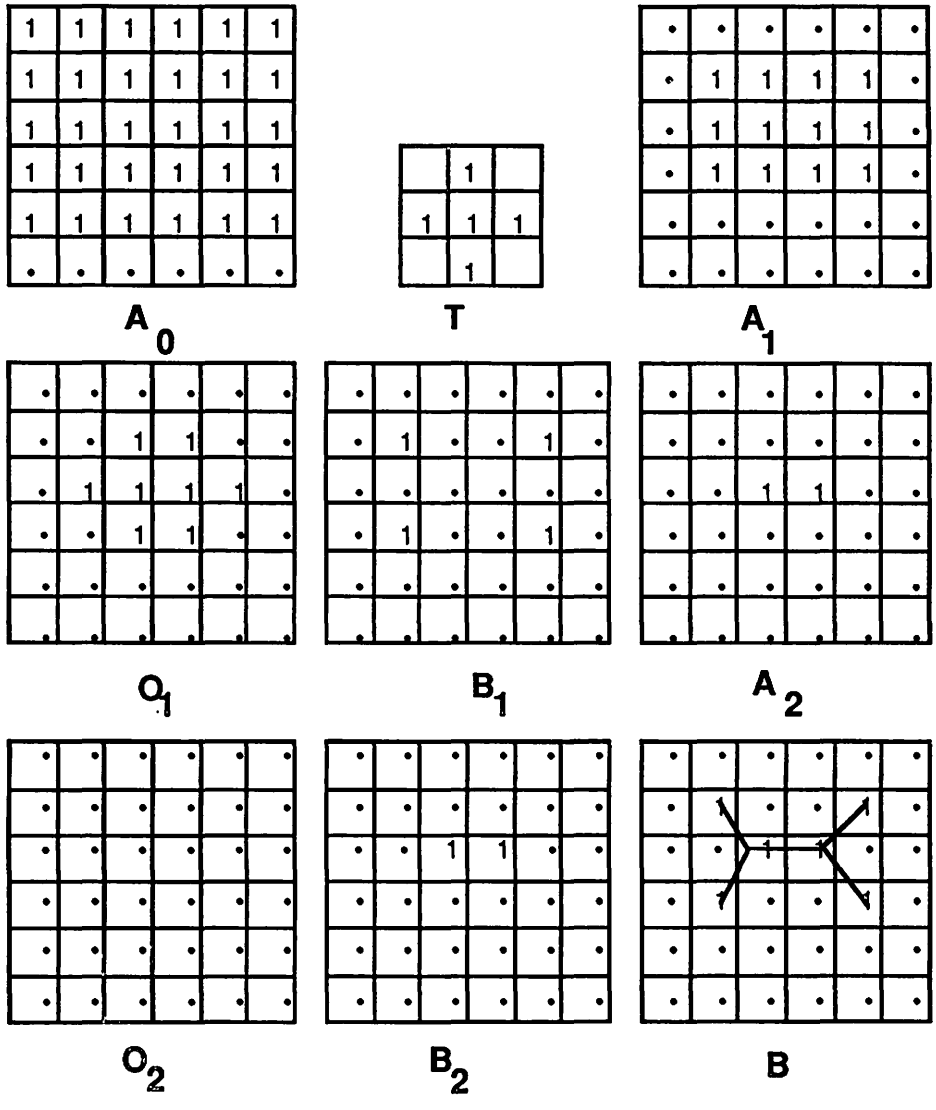

Figure 8.2: Illustration of morphological skeletonizing

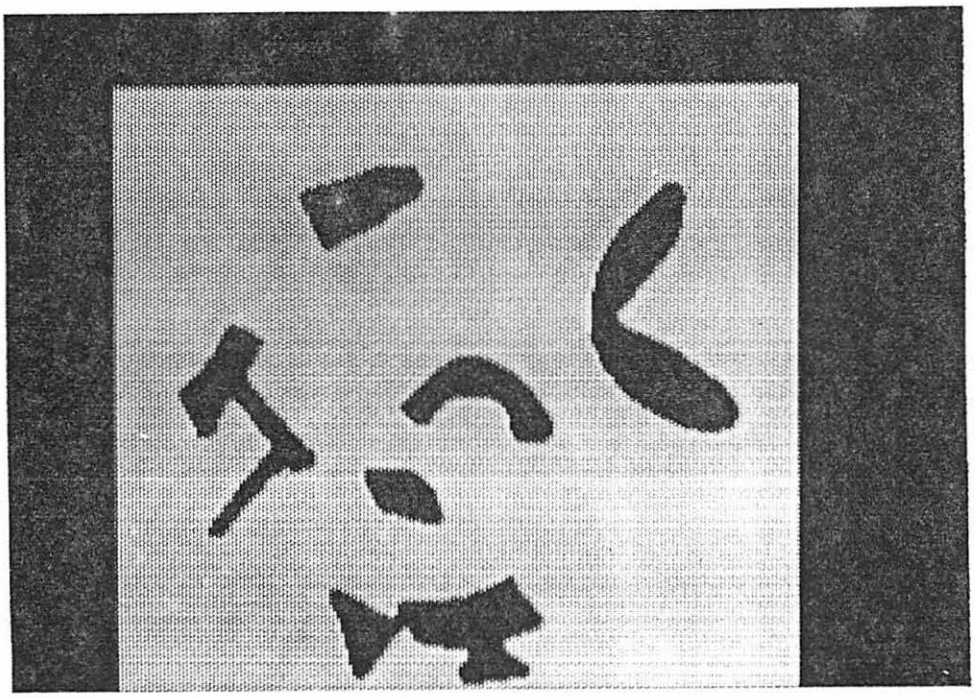

Figure 8.3: Simulated image of the metal matrix composite showing the silicon carbide particles

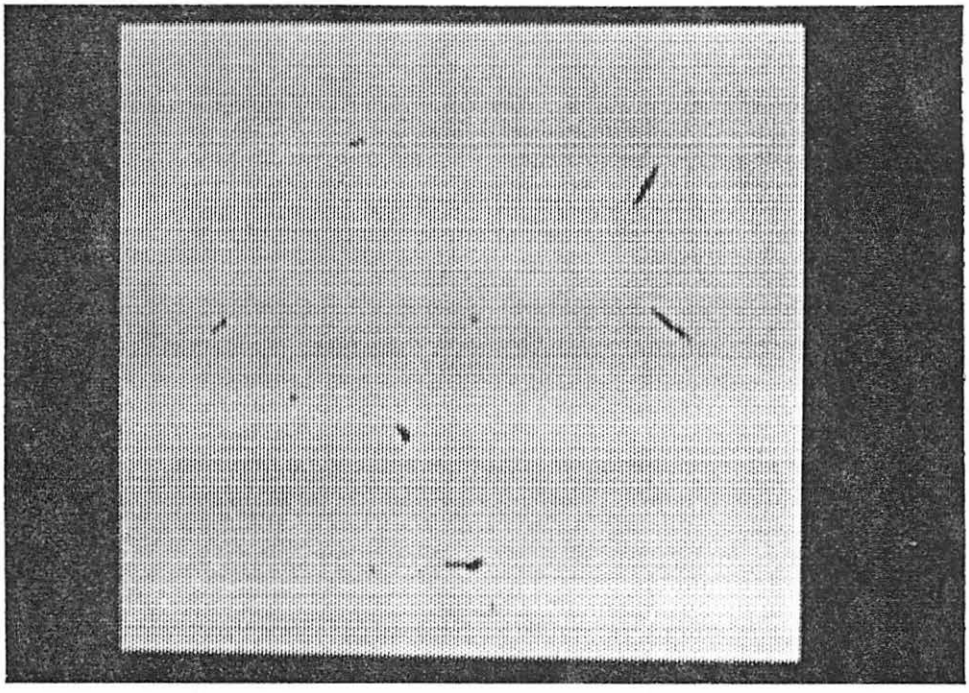

Figure 8.4: Seeds generated by CFS

Step 2: The morphological skeleton of the image is formed using the skeletonizing algorithm. Figure 8.5 gives the skeleton of Figure 8.3.

Step 3: For each connected component that is either isolated or clustered, its corresponding skeleton is checked to see whether it is branched or not. A histogram of the angles made by every point in the skeleton is made. There are as many branches in the skeleton as there are peaks in the histogram. If skeleton is not branched and the CFS generated just one seed for that component, it implies that the component is single. If, the skeleton if branched, there is a possibility that the component is a cluster of particles. To avoid the complexity in programming, a cluster with three connected particles will be analyzed. The picture on the top left in Figure 8.6 shows the cluster and the picture on the top right gives the skeleton.

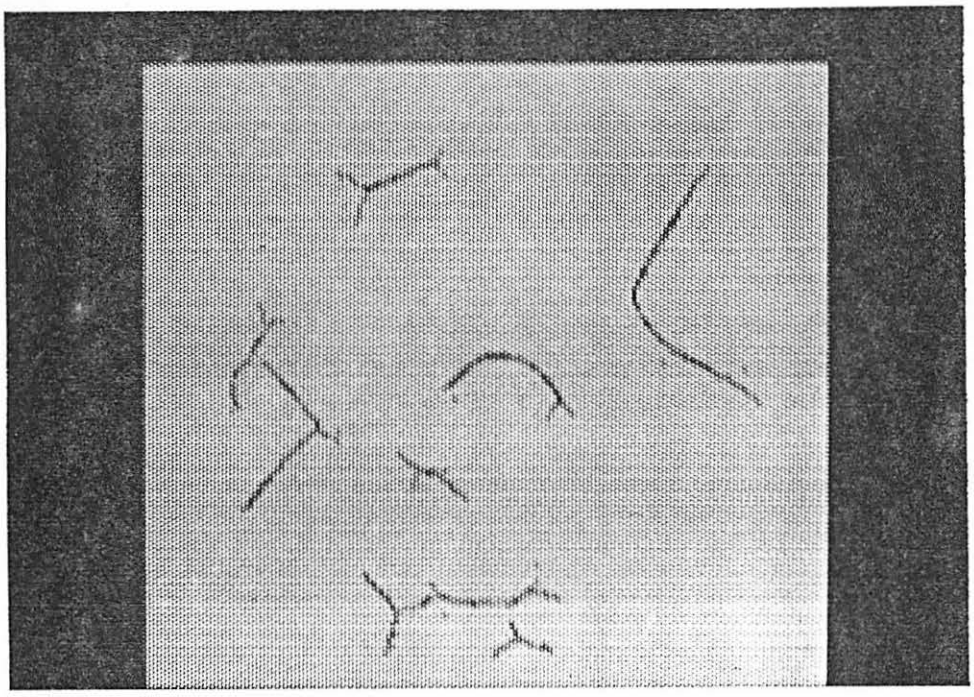

Figure 8.5: Skeleton of Figure 8.3

Step 4: If the number of the branches of the skeleton correspond to the number of seeds generated by CFS, the seeds can be grown back with the connectivity broken.

Step 5: If the numbers do not correspond, then the conditional skeleton is used to break the connectivity. The conditional skeleton is defined as the line joining the centers of the maximal disks of radii greater than a critical value known as the critical radius r. The algorithm for generating the conditional skeleton is as given:

$$\begin{aligned} &\textit{Let } \mathbf{A}_0 = \mathbf{A} \textit{ and } i = 0. \\ &\textit{do until } \mathbf{B}_i = 0 \\ &\mathbf{A}_{i+1} = \mathbf{A}_i \ominus \mathbf{T} \\ &\mathbf{B}_{i+1} = \mathbf{A}_{i+1} - (\mathbf{A}_{i+1} \circ \mathbf{T}) \\ &i = i + 1 \end{aligned} \tag{8.3}$$

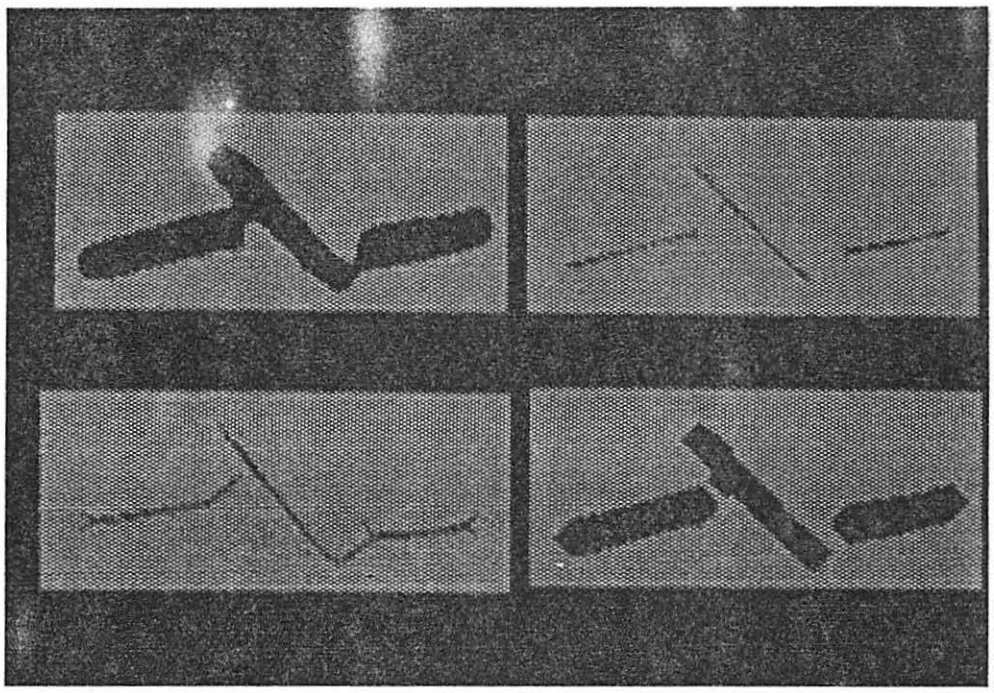

Figure 8.6: Cluster with the connectivity broken

$$\textit{enddo.}$$

$$\mathbf{B} = \sum_{k=r}^{i-1} \mathbf{B}_k. \tag{8.4}$$

The picture on the lower left gives the conditional skeleton with a critical radius of four. The conditional skeleton can be grown back using Step 3 in CFS to break the connectivity as shown in the lower right. It took four repeated conditional dilations to get the final result.

CHAPTER 9. CONCLUSION

When we started our research in Image Analysis Using Mathematical Morphology, every one was kind of pessimistic as to whether this rising star of the eighties could handle the highly demanding NDE images. Our group is involved in developing a software package to meet the image processing needs of the NDE community. This package contains at least a dozen morphological algorithms and demonstrates beyond doubt the confidence we have in the ability of morphology to handle the toughest images. No image processing software package will be complete without morphological routines. Morphological routines tend to fail when the image is too noisy and thus are not without drawbacks. But there are certain tasks like background elimination where morphology has no peers.

The first two chapters of this thesis explained the concepts of binary morphology and gray-scale morphology. The mathematics of morphology is intense and at times tend to be abstract. Only the principles that directly explain mathematical morphology have been included. Careful tailoring has been done, so that the material can be easily read by someone without a great mathematical background. Simple algorithms that perform gray-scale dilation and erosion have been included with pictorial illustrations.

My research so far has opened doors to further research in many different areas.

One area in which a lot of research is going on currently is to implement design procedures for design of morphological filters. The state of the art of morphological filters depends on a priori information of the size of the flaws. This could hinder the automated detection of flaws, if no a priori information is available. But compared to digital filters, it is easier to physically visualize the operation of morphological filters as pictorially represented in Chapter 4. Thus, it is easier for a technician or a non-signal- processing person to use morphological filtering. If it becomes necessary to classify the flaws based on size, the sieving filter comes in handy.

Another aspect of morphological filtering that has not been fully understood is the role played by structuring elements. The size of the structuring elements plays an important role in morphological filtering. But the role played by the intensity of the structuring element has not been fully understood. If it is possible to put the intensity information to good use, it might be possible to discriminate between noise and flaws on the basis of intensity information. We have experimented with various symmetric structuring elements. It will be interesting to study the effect of asymmetric structuring elements on gray-scale images. It was also found that a cylinder was the ideal structuring element for estimating background of NDE x-ray images. For filtering applications, a smoothly varying surface like a hemisphere or a paraboloid will be appropriate.

One thing I liked about my research was the opportunity that was available to work with real life problems. X-ray images are rarely a pretty sight. They often tend to be noisy, of low contrast and with lots of background trends and artifacts. Someone once stated at a image processing seminar that the best image processing routines are the simple minded routines such as histogram equalization, low-pass

filtering and high-pass filtering. He is probably right. These routines could do a better job on seventy five percent of the images than complicated routines such as the Kalman filtering. Most x-ray NDE images are among the unfortunate twenty five percent. All NDE is about is detection of flaws. Extracting flaws by estimating the background using opening or closing is perhaps the greatest contribution of mathematical morphology towards nondestructive evaluation of materials. Figures 5.3 and 5.4 are classic illustrations of the power of morphology.

When working on the Westinghouse samples, there arose the need for a structuring element that could pull out faint cracks but would leave small noise like regions untouched. A cylinder could be used to pull out the crack but it would have pulled out all the noise with it. It is then that I decided to try a plane. The plane could fit into the crack but not into the noise-like features. Thus, the noise-like features will be removed from the image. That is the beauty of morphology. It was later extended to the elimination of artifacts.

Some work has been done on the connectivity problem. So far, the flaws have been assumed to be convex and the images binary. A lot more work is yet to be done on connectivity. The connectivity algorithms have to be extended to include gray-scale images and non-convex flaws. Studies have to be done to see whether connectivity properties could be extracted from stereoscopic pairs of images.

Any work is gratifying when the outcome lives up to your expectations. This is especially true in research where the chances of success break even with failure. This has been a great experience for me and the good results kept my confidence and interest in mathematical morphology soaring.

CHAPTER 10. BIBLIOGRAPHY

Chackalackal, M.S., and Basart, J.P. 1990. *NDE X-ray Image Analysis Using Mathematical Morphology.* Review of Progress in Quantitative Nondestructive Evaluation, 9:700-707.

Chen, M., and Yan, P. 1989. *A Multiscaling Approach Based on Morphological Filtering.* IEEE Transactions on PAMI, 7:694–700.

Coleman, E.N., and Sampson, R.E. 1982. *Acquisition of randomly oriented workpieces through structure mating.* Proc. Computer Vision Pattern Recognition Conf., 350–357.

Giardina, C.R., and Dougherty, E.R. 1988. *Morphological Methods in Signal and Image Processing.* Prentice Hall, Englewood Cliffs, New Jersey.

Golay, M.J.E. 1969. *Hexagonal parallel pattern transformations.* IEEE Trans. Comput., 18:733–740.

Hadwiger, H. 1957. *Vorlesungen uber Inhalt, Oberflache und Isoperimetrie.* Springer-Verlag, Berlin.

Haralick, R.M., Sternberg, S.R., and Xinhua, X. 1987. *Image Analysis Using Mathematical Morphology.* IEEE Transactions on PAMI, 9(4):532–550.

Kirsch, R.A., Cahn, L., and Ray, C. 1957. *Experiments in processing pictorial information with a digital computer.* Proc. Eastern Joint Comput. Conf., 221–229.

Lantuejoul, C. 1980. *Skeletonization in quantitative metallography.* Issues of Digital Image Processing, Groningen, Netherlands.

Lantuejoul, C., and Serra, J. 1982. *M-Filters.* Proc. IEEE Int. Conf. Acoust.,

Speech, Signal Processing, 2063–2066.

Lee, J.S.J, Haralick, R.M., and Shapiro, L.G. 1986. *Morphologic Edge Detection.* Digital Image Processing in Industrial Applications, 7–14.

Mandenville, J.R. 1985. *Novel method for analysis of printed circuit images.* IBM J. Res. Develop., 29:73–86.

Maragos, P. and Schafer, R.W. 1986. *Applications of morphological filtering to image processing and analysis.* Proc. IEEE Int. Conf. ASSP, 2067–2070.

Maragos, P. and Schafer, R.W. 1987. *Morphological Filters.* IEEE Trans. Acoust., Speech, Signal Processing, 35:1153–1185.

Matheron, G. 1965. *Elements Pour une Tiorre des Mulieux Poreux.* Masson, Paris.

Matheron, G. 1975. *Random Sets and Integral Geometry.* Wiley, New York.

Meyer,F. 1979. *Iterative image transformations on an automatic screening of cervical smears.* J. Histochem. Cytochem., 27:128–135.

Meyer, F. 1986. *Automatic Screening of Cytological Specimens.* Computer Vision, Graphics, and Image Processing, 35:356–369.

Minkowski, H. 1903. *Volumen und oberflache.* Math. Ann., 57:447–495.

Moore, G.A. 1968. *Automatic scanning and computer processes for the quantitative analysis of micrographs and equivalent subjects.* Pictorial Pattern Recognition, 275–326.

Nakagawa, Y., and Rosenfeld, A. 1978. *A note on the use of local min and max operators in digital image processing.* IEEE Trans. Syst., Man, Cybern., 8:632–635.

Peleg, S., and Rosenfeld, A. 1981. *A min max medial axis transformation.* IEEE Trans. Pattern Anal. Machine Intell., 3:206–210.

Preston, K. 1961. *Machine techniques for automatic identification of binucleate lymphocyte.* Proc. Fourth Int. Conf. Medical Electronics, 25–37.

Rodenacker, K., Gais, P., Jutting, U., and Burger, G. 1983. *Mathematical morphology in grey images.* Proc. 1983 Euro. Signal Processing Conf., 200–210.

Serra, J. 1972. *Stereology and structuring elements.* J. Microscopy, 99–103.

Serra, J. 1982. *Image Analysis and Mathematical Morphology.* Academic Press, London.

Serra, J. 1986. *Introduction to Mathematical Morphology.* Computer Vision, Graphics, and Image Processing, 35:283–305.

Skolnick, M.M. 1986. *Application of Morphological Transformations to the Analysis of Two-Dimensional Electrophoretic Gels of Biological Materials.* Computer Vision, Graphics, and Image Processing, 35:306-332.

Song, J., and Delp, E.J. 1989. *A generalization of morphological filters using multiple structuring elements.* Proc. of the 1989 IEEE International Symposium on Circuits and Systems, 991–994.

Sternberg, S.R. 1979. *Parrallel architectures for image processing.* Proc. IEEE COMPSAC, Chicago.

Sternberg, S.R. 1980. *Cellular computers and biomedical image processing.* Biomedical Images and Processing, 294–319.

Sternberg, S.R. 1982. *Esoteric iterative algorithms.* Proc. Second Int. Conf. Image Analysis and Processing, Brindisi, Italy.

Sternberg, S.R. 1983. *Biomedical image processing.* Computer, 16:22–34.

Sternberg, S.R., and Sternberg, E.S. 1983. *Industrial inspection by morphological virtual gauging.* Proc. IEEE CAPAIDM, Pasadena, California.

Sternberg, S.R. 1986. *Grayscale Morphology.* Computer Vision, Graphics, and Image Processing, 35:333–355.

Unger, S. H. 1958. *A computer oriented to spatial problems.* Proc. IRE, 46:1744–1750.

Werman, M. and Peleg, S. 1985. *Min-max operators in texture analysis.* IEEE Trans. Pattern Anal. Machine Intell., 7:730–733.

Zhuang, X. and Haralick, R.M. 1986. *Morphological Structuring Element Decomposition.* Computer Vision, Graphics, and Image Processing, 35:370-382.